Advanced System Design and Signal Processing Techniques for Converged High-Speed Optical and Wireless Applications

A Dissertation
Presented to
The Academic Faculty

by

Cheng Liu

In Partial Fulfillment

of the Requirements for the Degree

Doctor of Philosophy in the

School of Electrical and Computer Engineering

Georgia Institute of Technology

August, 2013

Advanced System Design and Signal Processing Techniques for Converged High-Speed Optical and Wireless Applications

Approved by

Dr. Gee-Kung Chang, Advisor
School of Electrical and Computer Engineering
Georgia Institute of Technology

Dr. John R. Barry
School of Electrical and Computer Engineering
Georgia Institute of Technology

Dr. Aaron D. Lanterman
School of Electrical and Computer Engineering
Georgia Institute of Technology

Dr. Stephen E. Ralph
School of Electrical and Computer Engineering
Georgia Institute of Technology

Dr. Youjiang Wang
School of Materials Science and Engineering
Georgia Institute of Technology

Date Approved: June 03, 2013

To my parents and my beloved fiancée Jing,

for their unconditional support and encouragement

ACKNOWLEDGEMENTS

I would like to take this great opportunity to express my sincere gratitude to the many people who made this dissertation possible.

Foremost, I am very grateful to my advisor, Professor Gee-Kung Chang, for his guidance, patience, and continuous support. It is my great honor and great pleasure to work with him as his student. I learned a lot from him both in the class and off the class. He will always be my mentor for the rest of my life.

Another person I am also deeply thankful for is Prof. Stephen E. Ralph. I really appreciate his guidance on the Terabit Consortium project. That project expanded my research scope and enriched my research experience. I would also like to thank Professor John R. Barry, Professor Aaron D. Lanterman, and Professor Youjiang Wang for serving as my committee members and their valuable suggestions on my dissertation.

I am certainly appreciative and thankful for all my colleagues in both Optical Networking Research Group and Terabit Consortium. Their advice and collaboration as well as friendship have supported my professional and personal life during the five-year Ph.D. study. Thanks to Hung-Chang Chien, Yu-Ting Hsueh, Shu-Hao Fan, Jesse Hsin, Zhensheng Jia, Wei Jian, Claudio Estevez, Arshad Chowdhury, Ming Zhu, Jie Pan, Andy Stark, Jing Wang, Lin Cheng, Tom Detwiler, and many other grad students whom I have worked with in both groups.

I am also very fortunate to make many good friends at Atlanta during my Ph.D. study. Special thanks go to Zhixuan Xia, Dong Yang, Wei Mu, Tianyu Jiang, Min Na, Jiumeng Liu, Zhen Gao, Jing Chen, and Ke Yu. I am so grateful for all the great memories we had together at Atlanta, and wish our friendship last forever no matter where we are in the future.

Lastly, I would like to thank my family for all their love and encouragement. For my parents, Youlin Liu and Liya Wang, who did their best to give me the best education and always provide me the unconditional support. They raised me up and taught me how to become a considerate and responsible man for the family and the society. Saving the best for last, I would like to thank my lovely fiancée, Jing Xu. Your constant support and love were the most important driving force throughout my Ph.D. life. Thank you and thank you all.

TABLE OF CONTENTS

LIST OF TABLES

LIST OF FIGURES

LIST OF ABBREVIATIONS

ADC	Analog-to-digital convertor
AP	Access point
ASE	Amplified spontaneous emission
AWG	Arrayed-waveguide grating
AWG	Arbitrary waveform generator
BBU	Baseband processing unit
BER	Bit-error rate
BPF	Band-pass filter
BS	Base station
BTB/B2B	Back-to-back
BW	Bandwidth
BWA	Broadband wireless access
CAPEX	Capital expenditure
CATV	Community antenna television
CD	Chromatic dispersion
CL	Circulator
CO	Central office
CoMP	Coordinated multi-point transmission
CP	Cyclic prefix
C-RAN	Cloud radio access network
CSR	Carrier-suppression ratio
CW	Continuous wave
DAS	Distributed antenna system
DB	Duobinary
DC	Direct current
DEMUX	Demultiplexer
DI	Delay interferometer
DL	Downlink
DMD	Digital micromirror device
DP	Dual polarization
DQPSK	Differential quadrature phase-shift keying
DS	Downstream
DSB	Double sideband
DSB-OCS	Double-sideband optical-carrier suppression
DWDM	Dense wavelength-division multiplexing
EA	Electrical amplifier
EDFA	Erbium-doped fiber amplifier
EIRP	Equivalent isotropic radiated power
EVM	Error-vector magnitude
FBG	Fiber Bragg grating
FCC	Federal Communications Commission
FEC	Forward error correction
FMF	Few-mode fiber
FTTB	Fiber-to-the-building

FTTH	Fiber-to-the-home
FWM	Four-wave mixing
GPS	Global positioning system
HDTV	High-definition television
Het-Net	Heterogeneous network
HSR	Harmonics-suppression ratio
ICI	Inter-channel interference
IF	Intermediate frequency
IL	Interleaver
IM	Intensity modulation/ Intensity modulator
IP	Internet protocol
ISI	Inter-symbol interference
LAN	Local area network
LD	Laser diode
LDPC	Low-density parity-check code
LMS	Least mean square
LNA	Low-noise amplifier
LO	Local oscillator
LPF	Low-pass filter
LTE	Long term evolution
MAC	Medium access control
MCF	Multi-core fiber
MI	Modulation index
MIMO	Multiple input and multiple output
Mm-wave	Millimeter wave
MS	Mobile subscriber
MUX	Multiplexer
MW	Microwave
MZM	Mach-Zehnder modulator
NF	Noise figure
NRZ	Non-return-to-zero
OCS	Optical carrier suppression
OF	Optical filter
OFC	Optical Fiber Communication Conference
OFDM	Orthogonal frequency-division multiplexing
OOK	On-off keying
OPEX	Operating expense
OSNR	Optical signal-to-noise ratio
OTN	Optical transport network
O/E	Optical to electrical
PA	Power amplifier
PBS	Polarization beam splitter
PC	Polarization controller
PD	Photodetector
PDM	Polarization-division multiplexing
PHY	Physical layer

PMD	Polarization-mode dispersion
PM	Phase modulation/ Phase modulator
Pol	Polarization
Pol-Mux	Polarization-multiplexing
PRBS	Pseudorandom-bit sequence
Pre-comp	Pre-compensation
PON	Passive optical network
RAN	Radio access network
RAU	Remote antenna/access unit
RB	Rayleigh backscattering
RBS	Random-bit sequence
RF	Radio frequency
RN	Remote node
ROADM	Reconfigurable optical add/drop multiplexer
RoF	Radio-over-fiber
RRH	Remote radio head
RZ	Return-to-zero
SDM	Spatial division multiplexing
SPM	Single-phase modulation
SSB	Single sideband
SSMF	Standard single-mode fiber
TDM	Time-division multiplexing
TFBG	Tunable fiber Bragg grating
Tx	Transmitter
UL	Uplink
VNI	Visual networking index
VOA	Variable optical attenuator
WDM	Wavelength-division multiplexing
WAN	Wide area network
WCNC	Wireless Communication and Networking Conference
WiGig	Wireless Gigabit Alliance
WLAN	Wireless local area network
WMAN	Wireless metropolitan area networks
WPAN	Wireless personal area network
WSS	Wavelength-selective switch
XPM	Cross-phase modulation
XPolM	Cross-polarization modulation

SUMMARY

The ever-increasing data traffic demand drives the evolution of telecommunication networks. The evolution of network architecture and underlying technologies happens not only in the last-mile access networks but also in the long-haul backbone networks. This Ph.D. dissertation focuses on system design and signal processing techniques for next-generation converged optical-wireless access systems and the high-speed long-haul coherent optical communication systems.

For access networks, due to the great mobility and flexibility provided by wireless access networks and the abundant bandwidth and capacity provided by fiber-optic access networks, the convergence of optical and wireless access systems is the trend for the next-generation broadband access. In particular, using high-speed fiber-optic backhaul networks for next-generation small-cell wireless access system has become an important topic and requires strong interdisciplinary research efforts. In this thesis work, a cloud-radio-over-fiber (cloud-RoF) access architecture is proposed as a promising solution to centralize processing power of cell sites to the “cloud”, thus simplifies the conventionally expensive and power-hungry cell sites. This enables a large-scale small-cell system to be deployed in a cost-effective and power-efficient way. By taking advantage of centralized processing power of the cloud-RoF architecture, a reconfigurable backhaul network is proposed and demonstrated to serve different traffic-load areas and different mobile user patterns. In addition, the combination of radio-over-fiber (RoF) technologies and wavelength division multiplexing (WDM) techniques enables multiple wireless services (e.g. GSM, 3G,

4G-LTE, etc.) coexist in the backhaul network by sharing the optical infrastructure, which further reduces the CAPEX and OPEX related to small-cell deployment.

Additionally, due to the congested RF spectrum at lower RF bands (700MHz to 5GHz), exploration and exploitation of higher radio frequencies become important research topic to further increase wireless transmission capacity. 60GHz millimeter-wave (mm-wave) band in particular has drawn significant attention due to its 7-GHz unlicensed bandwidth. Interestingly, due to the limited transmission range at higher RF bands, the combination of small-cell cloud-RoF architecture and mm-wave radio provides an ideal solution to drastically increase the system capacity through frequency exploitation and reuse. However, the challenges of mm-wave cloud-RoF system are mainly on optical mm-wave signal generation and transmission. In this dissertation, based on mm-wave-photonics techniques, several novel system designs are proposed and demonstrated that enable advanced modulation format transmission in mm-wave cloud-RoF systems in a simplified way.

For long-haul core networks, ultra-high-speed optical communication systems which can support ≥ 1Terabit/s per channel transmission will soon be required to meet the increasing capacity demand in the core networks. However, 1Tb/s over a single optical carrier requires either or both a high-level modulation format (i.e. 1024QAM) and a high baud rate. Alternatively, grouping a number of tightly spaced “sub-carriers” to form a terabit superchannel increases channel capacity while minimizing the need for high-level modulation formats and high baud rate, which may allow existing formats, baud rate and components to be exploited. In ideal Nyquist-WDM superchannel systems, optical subcarriers with rectangular spectra are

tightly packed at a channel spacing equal to the baud rate, thus achieving the Nyquist bandwidth limit. However, in practical Nyquist-WDM systems, precise control on channel spectra is required to avoid strong inter-channel interference (ICI). Conventional ways to mitigate the impact of ICI include optical or electrical filtering at transmitter side; however these approaches are not flexible to the transport networks. In this thesis work, we propose and demonstrate a new “super receiver” architecture for practical Nyquist-WDM systems, which jointly detects and demodulates multiple channels simultaneously and mitigates the penalties associated with the limitations of generating ideal Nyquist-WDM spectra. Several joint DSP algorithms are developed for linear ICI cancellation and joint carrier-phase recovery. Performance analysis under different system configurations is conducted to demonstrate the feasibility and robustness of the proposed joint DSP algorithms, and improved system performance is observed with both experimental and simulation data.

CHAPTER 1: INTRODUCTION

1.1 Motivation

In the era of rapid-paced "Information Age," people generate and distribute information all around the world much more frequently and in a much higher speed than in any previous era in the history. According to the collected data and forecast from Cisco [1][2], the global IP traffic will increase over seven-fold between 2009 and 2016, as shown in Figure 1.1. By the year of 2016, the number of devices connected to IP networks will be nearly three times as high as the global population in 2016.

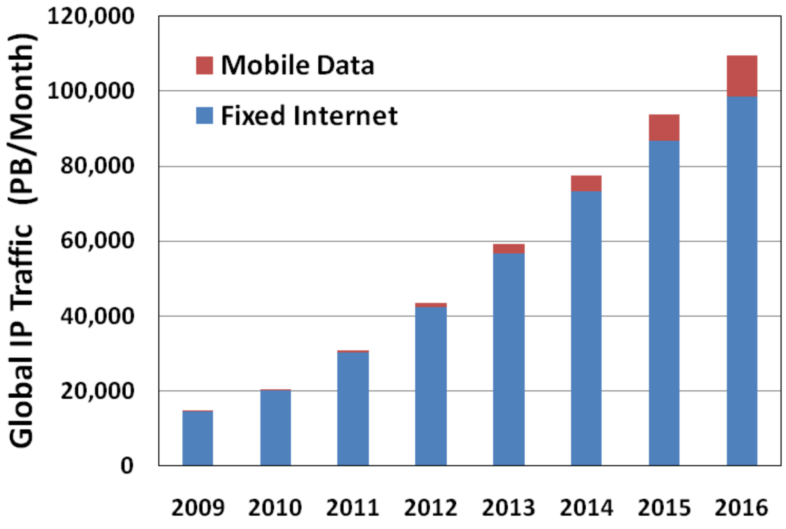

Figure 1.1. Global IP traffic growth from 2009 to 2016.

At the same time, mobile data traffic is increasing in an even faster growth rate. From 2009 to 2011, the increase of mobile data traffic is over six-fold [3], and the estimated growth rate of mobile data traffic between 2011 and 2016 is 18-fold [4]. By looking at the mobile traffic of different content types, as shown in Figure 1.2, it is observed that the mobile video, which demands higher bandwidth and less latency, will be the "killer" application generating over 70 percent of the total mobile data traffic in 2016.

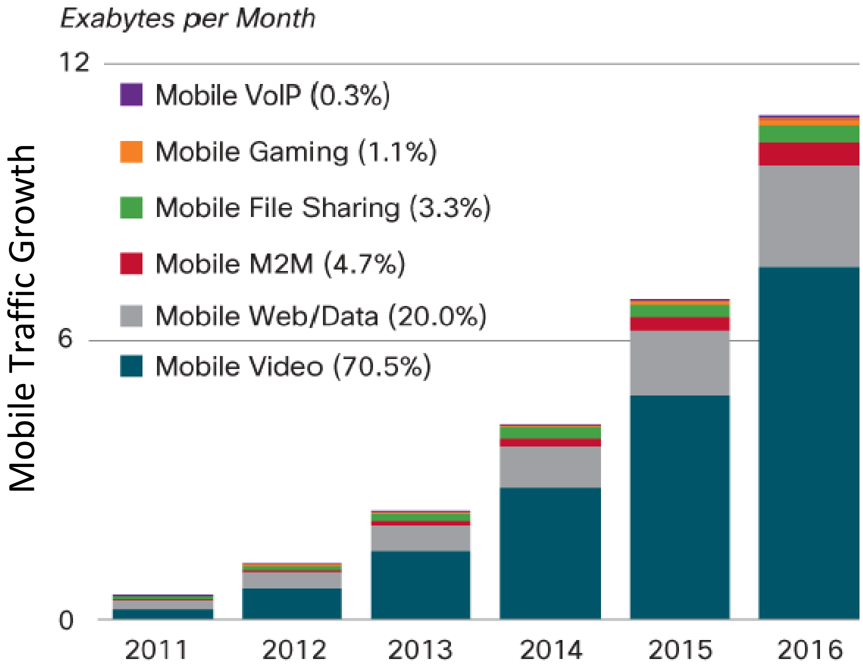

Figure 1.2. Global mobile data traffic growth by content types from 2011 to 2016 [4].

The enabling technologies behind the overwhelming explosions of both fixed and mobile data traffic rely on two telecommunication societies: (1) Optical fiber communication for backbone and backhaul networks; (2) Wireless communication for mobile access networks.

Since optical fiber was introduced as a promising communication medium by Charles Kao and George Hockham in 1966, and followed by successful demonstrations and developments by Corning Glass Works in the 1970s, optical fiber has revolutionized the telecommunication industry and played a major role in the advent of the "Information Age." Because of its less propagation loss and higher bandwidth capacity over conventional electrical cable, optical fibers have replaced copper wires in all the core and metro networks, and are pushing closer and closer to end users in the access networks (see Figure 1.3).

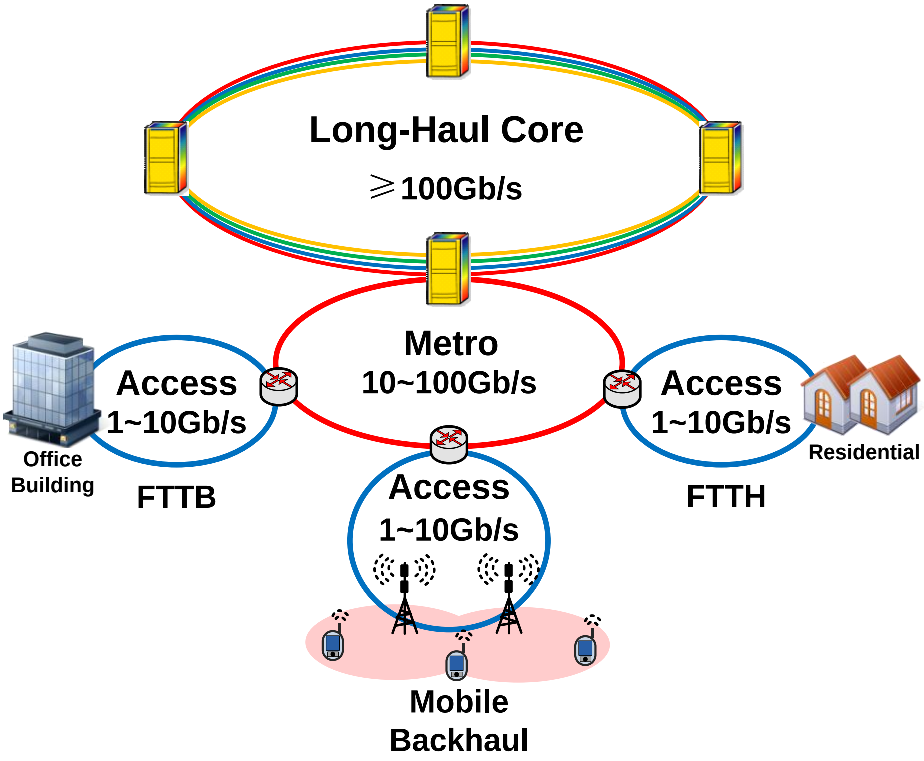

Figure 1.3. Architecture of fiber-optic communication network and its applications.

The current research interests in the Optical Fiber Communication Society mainly focus on two areas: (1) The enabling technologies to further increase transmission capacities of optical fibers in the metro and long-haul optical networks to accommodate ever-increasing data traffic demands in the core networks; (2) The enabling technologies to provide cost-effective solutions for the high-speed optical access networks and their seamless convergence with wireless access networks.

On the other hand for the wireless communication society, the discovery of electromagnetic waves for communication purposes can be traced back to 1888, when Heinrich Hertz demonstrated the radio wave propagation for the first time. Over more than one century, numerous technologies have been developed to continuously advance the wireless communication theories. Nowadays the applications of wireless communications are all around in our daily lives: from remote garage door openers to smart phones; from GPS navigations to satellite televisions, people enjoy the convenience of wireless technologies, and keep pursuing for higher speed and better quality experiences.

The evolution of modern cellular phone networks is a great example of the continuous innovations of wireless communication technologies. The advances can be traced in successive generations from the early "0G" services to first generation (1G) analog cellular networks, second generation (2G) digital cellular networks, third generation (3G) broadband data services to the current state of the art, fourth generation (4G) native-IP networks, and future 4G-LTE networks. Every step forward provides mobile subscribers with more mobile services at higher speeds.

However, to keep up with the fast increasing mobile data traffic, future mobile networks need to provide even higher capacity and seamless connectivity between all different types of mobile devices. As Dr. Siavash Alamouti pointed out at the wireless communication and networking conference (WCNC) in 2012 [5], the existing wireless technologies for point-to-point wireless transmission within a given RF bandwidth have been pushed very close to the Shannon theoretical limit by using high-level modulation formats (e.g. 64QAM-OFDM), multiple-input and multiple-output (MIMO) techniques, and advanced channel coding schemes (e.g. LDPC and Turbo code). However, there are still some potential areas that can be further explored to increase the total system capacity, as listed in Table 1.1. As we can see, the ultimate solutions for future mobile networks come down to use smaller cell size with higher carrier frequencies, and also be able to support intra-cell and inter-cell coordination to enhance the overall system spectral efficiency.

Table 1.1. Next-generation wireless communication technologies [5].

Approaches	***Potentials***
Link Spectrum Efficiency	Near limit
System Spectrum Efficiency	Great potential, but challenging
More Spectrum	Only in high frequencies
Smaller Cell	Almost unlimited potentials, but expensive

The similar prediction was given by Dr. Milo Medin in his keynote speech at optical fiber communication conference (OFC) 2012 [6]. He mentioned that the only way to scale the mobile network to support exponentially increasing data traffic is by reducing the cell size. Therefore, he suggested that the future cellular networks would be very similar to today’s WiFi networks (or converge with WiFi networks) with smaller cell size to provide higher throughput.

However, many practical issues associated with this small-cell architecture are still under discussions. For example, what is the cost-effective way to design this small-cell architecture in a large-scaled system with lots of base stations? What technologies should be used to provide the high-speed backhaul networks? How to deploy a heterogeneous network to leverage existing investments? Just like the name of the 4G-long term evolution (LTE) technologies suggested, this evolution will take time, and many interesting research topics along the path need to be addressed and resolved.

1.2 Research Background and Challenges

The background of high-speed optical and wireless communication is introduced in this section. Two particular research topics are investigated: (1) Next-generation converged optical-wireless access systems; 2) High-speed coherent optical communication systems. The challenges of both research areas are introduced as well.

1.2.1 Next-Generation Converged Optical-Wireless Access Networks

As mentioned previously in Section 1.1, the future wireless access networks are designed with 1) smaller cell size; 2) higher carrier frequency; 3) centralized processing power for intra-cell and inter-cell coordination; 4) supported by high-speed backhaul networks. In this section, small-cell cloud radio access networks (cloud-RAN) based on high-speed fiber-optic backhaul will first be discussed. Then cloud radio-over-fiber (cloud-RoF) techniques are introduced that further simplifies the design of small-cell wireless access networks. In addition, higher RF carrier frequency of millimeter-wave (mm-wave) band is introduced and combined with cloud-RoF systems to provide ultimate link throughput and system capacity for the next-generation wireless access networks. Also current challenges of mm-wave cloud-RoF system design will be discussed.

First of all, compared with conventional macrocell systems, small-cell systems reduce the cell size and reuse RF spectra among small cells more frequently, thus enhancing the total system capacity. Small-cell systems are likely to be deployed in traffic ‘hot-spots’ and ‘not-spots’, and to complement existing macrocell systems to form a heterogeneous network (Het-Net) [7].

To support the small cells, optical fibers are considered as ideal backhaul media to provide sufficient bandwidth as well as future-proof capacity upgrade. Therefore, optical-wireless integrated technologies for the next-generation small-cell wireless access networks become important topic and require strong interdisciplinary research efforts.

Recently, cloud-based radio access network (cloud-RAN) of small cells was proposed in this direction and has been advocated by both operators (e.g., NTT, KT, France Telecom/Orange, Telefonica, SoftBank/Sprint, and China Mobile [8]) as well as service providers (e.g., Alcatel-Lucent LightRadio [9], Nokia-Siemens Liquid Radio [10]). The basic concept of cloud-RAN is to separate the digital baseband processing units (BBUs) of conventional cell sites, from the largely analog radio access units / remote antenna units (RAUs), and move the BBUs to the “cloud” (BBU pool) for centralized signal processing and management. By centralizing the processing power, conventional complicated cell sites can be simplified to cost-effective and power-efficient RAUs, which is very important for the deployment of large-scale small-cell systems. In addition, the centralized processing power enables more advanced and efficient network coordination and management. For example, the coordination among several cell sites (or RAUs) enables inter-cell interference cancellation for cell-edge users and enhances their throughput in the concept of network multiple-input and multiple-output (network-MIMO) [11]. This inter-cell coordination can be achieved more efficiently in the cloud-RAN system with centralized processing power. Therefore, cloud-RAN architecture provides flexible, powerful, and more centralized network management for small-cell wireless access systems in a cost-effective and power-efficient way.

However, the design of optical backhaul networks to connect BBU pool with many small-cell RAUs and support high-speed backhaul data transmission is very critical for cloud-RAN systems. Currently, the small-cell backhaul is at an early stage of development, with a wide range of solutions being proposed and considered. The most prevailing method is to transmit digital baseband oversampled in-phase/quadrature (I/Q) streams in the backhaul link based on Common Public Radio Interface (CPRI) [12] or Open Base Station Architecture Initiative (OBSAI) [13]. However, due to I/Q streams are oversampled and multiple streams are needed to support multiple antennas for both intra-band inter-cell MIMO applications, this approach requires high system throughput and capacity of the backhaul networks. In addition, since MAC and PHY layer functions are separated at BBU and RAU respectively, latency and jitter must be carefully controlled in the cloud-RAN backhaul networks.

Therefore, evolving from the concept of small-cell cloud-RAN with centralized processing, our group at Georgia Tech has proposed a novel small-cell wireless access architecture based on radio-over-fiber (RoF) technologies [14]. By transmitting analog RF signals over fiber-optic backhaul, the functions of RAUs can be further simplified. More importantly, unlike the conventional digital-baseband-transmission approach that typically supports one service at a time, the analog-RF-over-fiber method enables multi-service multi-operator coexistence in a shared infrastructure without extra interference. In addition, it is beneficial to integrate with optical wavelength division multiplexing (WDM) techniques to provide more versatility and flexibility to the backhaul networks. Therefore, multiple system operational advantages can be achieved by in the proposed small-cell cloud-RoF system: Firstly, multiple operators can co-exist in a shared small-cell infrastructure by using different WDM wavelengths; Secondly, within each operator, different wireless services (including existing wireless services carried on lower RF bands (GSM, 3G, 4G-LTE) as well as the future-proof higher-RF-band services) can co-propagate in the RoF backhaul in a simplified way; Thirdly, for each wireless service, multiple MIMO data streams and multiple sub-bands (e.g. cognitive radio uses multiple RF sub-bands adaptively) can also coexist in the RoF link without incurring undesirable interference that hamper the high-bit-rate data services; Finally, multiple operators, multiple services, and multiple wireless techniques can share the same small-cell infrastructure while maintaining independent configurability through the centralized management.

Figure 1.4 and Figure 1.5 illustrate the conventional macrocell cellular systems and small-cell cloud-RoF systems, respectively. The differences are summarized in Table 1.2. First of all, the radius of small cells is reduced from 1km~10km of conventional macrocells to less than 500m. The radio frequency of the small cells can be either conventional low-RF microwave (700MHz ~ 5GHz) as well as future-proof millimeter -wave (mm-wave) band. Notice that for the mm-wave small cells, the cell size is limited to the scale less than 100 meters due to the high propagation loss, which makes them more likely to be deployed in in-building or out-door traffic "hot-spot" environments. Optical fibers are exclusively used as the backhaul media for the small-cell and multi-band cloud-RoF access system, which has major advantages over the conventional macrocell systems.

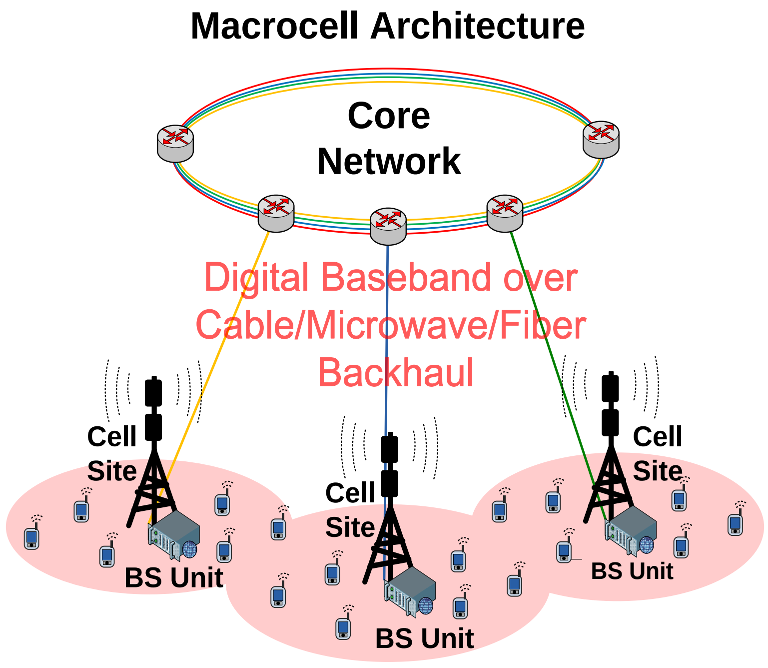

Figure 1.4. Conventional macrocell cellular system with digital baseband backhaul transmission.

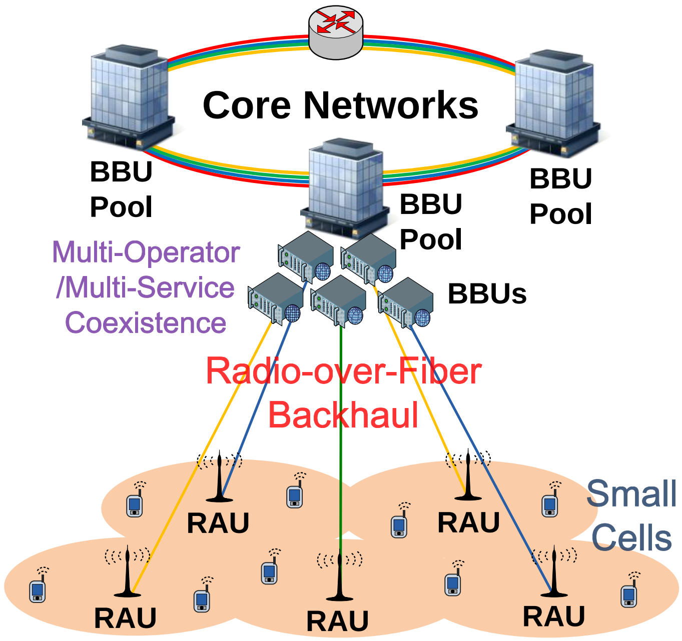

Figure 1.5. Small-cell cellular system with cloud-RoF backhaul.

Table 1.2. Comparison of macrocell and small-cell cloud-RoF systems.

	Macrocell	**Small-Cell Cloud-RoF**
Cell Size (radius)	1km~10km	10m~500m
Radio Frequency	700MHz ~ 5GHz	Microwave/ Mm-wave bands
Cell Site Functions	Baseband Processing/ RF Frontend	Simplified to RAU
Backhaul Media	Microwave/Cable/Fiber	Optical Fiber
Backhaul Signal Format	Digital Baseband	Analog RF

More importantly, the functions of central office and cell sites (or BBU and RAUs in cloud-RAN systems) as well as the associated signal transmission formats in the backhaul links are enhanced for the cloud-RoF system. The comparisons are illustrated in Figure 1.6. Comparing conventional cloud-RAN with macrocell, the cell sites are simplified to radio access units (RAUs) by shifting the MAC layer functions and baseband signal processing to the central office or BBU, and the digital I/Q samples are transmitted in the backhaul link. However, for the proposed cloud-RoF system, the function of RAU is further simplified by shifting DAC/ADC and RF frontend to the BBU. Therefore, only O/E and E/O conversion, and RF antennas are needed in the remote antenna units (RAUs). Since RF front-end is shifted to BBU, RF signals are generated at BBU and transmitted to RAUs through radio-over-fiber backhaul links. Therefore, multi-band/multi-service/multi-operator radios can coexist in the fiber-optic backhaul just like they coexist in the air. This infrastructure-sharing feature can help to further reduce the cost related to the small-cell deployment, and also provide versatility to the small-cell cloud-RoF systems.

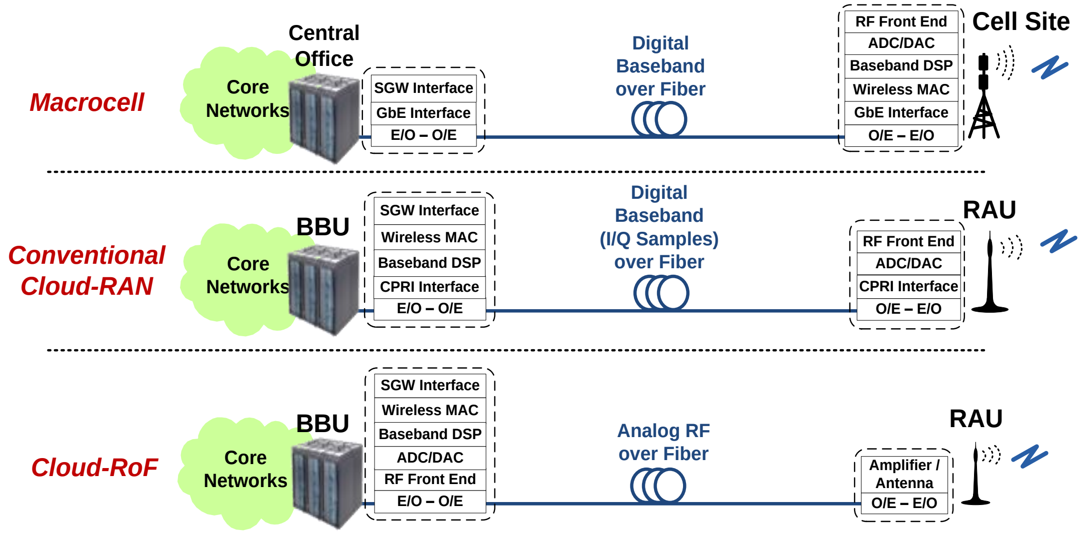

Figure 1.6. Functions of central-office and cell-sites (or BBU and RAUs) for macrocell, conventional cloud-RAN, and the proposed cloud-RoF systems.

On the other hand, exploration of higher radio carrier frequencies is another dimension to increase wireless transmission capacity, which is also a very hot research area independent of the aforementioned small-cell architecture study. However, due to the limited transmission range at higher RF bands, the combination of small-cell architecture and higher-RF band is a straightforward attempt and provides a promising solution to drastically increase the system capacity through both frequency exploitation and frequency reuse.

Therefore, in the following section, higher RF bands are introduced, and in particular, millimeter-wave (mm-wave) band is emphasized. The combination of mm-wave radio with cloud-RoF architecture will be discussed and the current challenges will be explained.

Radio frequency (RF) is the frequency of radio waves in the range of 3 KHz to 300GHz. Within this range, microwave band (300 MHz to 300GHz) is mainly used for high-speed mobile communications. Typically, the conventional cellular frequency band is from 800 MHz to 5GHz along with many other services, like wireless local area networks (LAN), and wireless personal area networks (PAN), as shown in Figure 1.7.

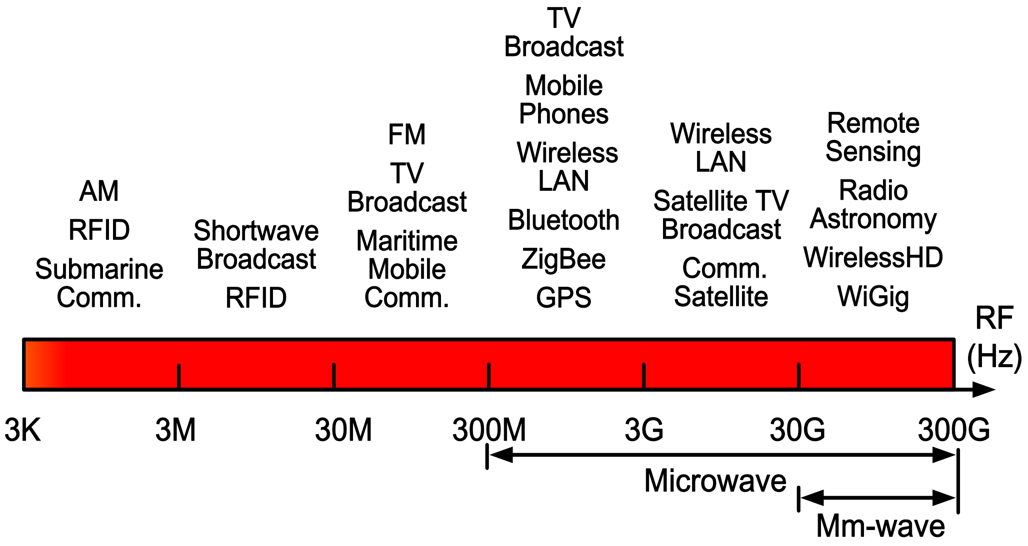

Figure 1.7. Radio frequency spectrum and example uses.

On the other hand, at the high end of the RF spectrum, particularly from 30GHz to 300GHz, more and more attentions have been drawn for ultra-high-speed wireless communication purposes. Since this RF band has a wavelength around one to ten millimeters, it is also called millimeter-wave (mm-wave) band. Within this mm-wave band, the frequencies near 60GHz range attract the most research interests. This is because many countries around the world have an approximately 7GHz unlicensed bandwidth around 60GHz, as shown in Figure 1.8. This huge bandwidth resource provides 100 times more bandwidth than the conventional cellular band, and therefore can easily support multi-gigabit even tens of gigabit wireless transmission.

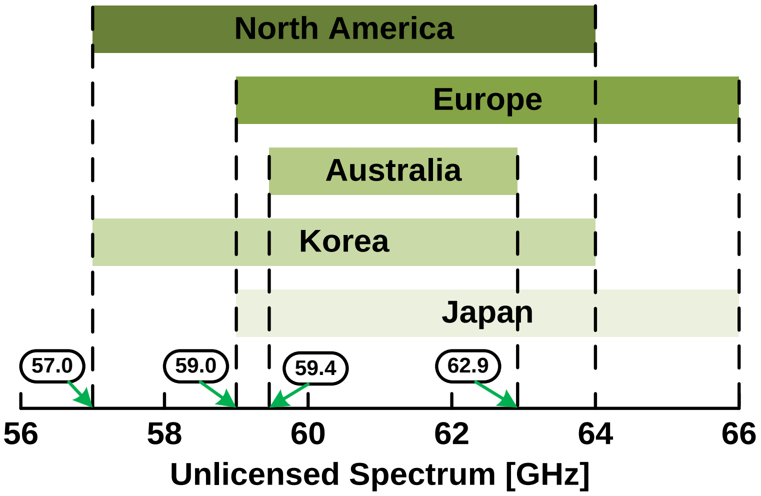

Figure 1.8. Worldwide unlicensed spectrum around 60GHz mm-wave band.

Because of the attractive bandwidth resources at 60GHz mm-wave band, many efforts are focused on standardizations at 60GHz band. For example, standards such as IEEE 802.15.3c [15], ECMA 387 [16], and WirelessHD [17] have been proposed for wireless personal area network (WPAN) applications. At the same time, IEEE 802.11ad [18] and wireless gigabit alliance (WiGig) standards [19] are in process targeting at wireless local area network (WLAN) applications at 60GHz.

However, there are several challenges of using 60GHz band for wireless communication, one major challenge is the limited transmission range. The limitation mainly comes from two aspects: 1) strong absorption by oxygen molecules in the air; 2) the quickly decayed received RF power in direct proportion to the square of radio frequency defined by the Friis transmission equation [20].

While this strong channel attenuation limits potential transmission range, on the other hand, it fits into the small-cell concept perfectly that allows more frequency reuse to increases the total system capacity. In addition, due to the line-of-sight (LOS) transmission nature at mm-wave band, not only very limited inter-cell interference is expected, but also it opens up a whole new dimension of multiplexing ("spatial" division multiplexing) among multiple users within the same cell.

Therefore, the combination of mm-wave band with aforementioned small-cell cloud-RoF architecture is a promising solution to increase the system capacity through both frequency exploitation and frequency reuse. A schematic diagram of the mm-wave cloud-RoF access system is shown in Figure 1.9.

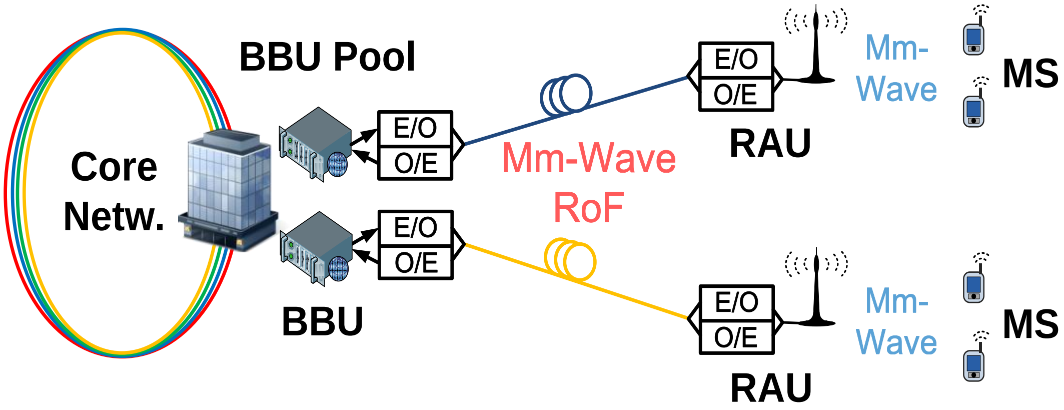

Figure 1.9. Combination of mm-wave band and cloud-RoF access.

The essential components to achieve the RoF transmission are the electrical-to-optical (E/O) and optical-to-electrical (O/E) conversion modules. The E/O conversion modulates the RF electrical signal onto optical carrier for both downlink and uplink RoF transmissions. The O/E conversion uses a photodetector (PD) to detect the RF signals carried on optical waves and convert them back to electrical domain.

At a lower carrier RF, this E/O and O/E conversions are not difficult to achieve. There have been commercial products that integrate the O/E and E/O functions in a single transceiver module that can support up to 6GHz RF bandwidth [21][22], which covers the conventional wireless communication band. However, when the RF carrier frequency becomes higher and higher up to the mm-wave band, it is over the electrical bandwidth limits of current available optoelectronics components.

Therefore, to get around this electrical bandwidth limitations, people have proposed several ways to first create optical mm-waves, and then generate the electrical mm-waves through optical beating at a photodetector [23]-[36]. These approaches include using fiber nonlinearity [32], injection locking [33], and double-sideband optical-carrier-suppression (DSB-OCS) through external modulations [26][34][35]. Among all the approaches, DSB-OCS scheme is the most widely used method because of its simplicity and reliability.

The basic idea of DSB-OCS scheme is to generate 60GHz mm-wave with only half of the electrical bandwidth (30GHz) required at the central office. There are several different ways to achieve DSB-OCS optical mm-wave generations, and to modulate data on the generated optical mm-waves. The detailed discussions will be given in Section 3.1.

At the receiver side, after photodetection, the beating between the two sidebands of the optical mm-wave will generate the electrical mm-wave carrying data. However, because of the data information are originally carried on both optical sidebands in the DSB-OCS scheme, after beating at a photodetector, the original data is squared that eliminates its phase information, and results in interferences. For the conventional on-off keying (OOK) modulation format, the original two-level information keeps unchanged after beating and square function. However, for vector signals (i.e. the signal with phase information) or analog signals carried on intermediate frequencies, the square function is detrimental to the original information. Therefore, the transmission of vector signals in the DSB-OCS mm-wave RoF system is a big challenge, and needs to be resolved.

In this dissertation, we will first discuss different optical mm-wave generation schemes, introduce different data modulation methods in the mm-wave RoF systems, and theoretically analyze the issues of vector signals transmission in different types of optical mm-wave RoF systems. Then we propose and demonstrate several novel system architectures that enable vector signal delivery in DSB-OCS mm-wave RoF systems. In addition, for a specific vector signal modulation format, duobinary (DB), we will design a novel RF receiver that reduces the receiver complexities to provide more robust system operations.

1.2.2 High-Speed Coherent Optical Communication Systems

In addition to the dramatic increase of data traffic demands in the access networks, the required transmission capacities in the underlying optical core networks have also increased significantly. Recently, optical transceiver modules have been commercialized to achieve 100Gb/s transmission rate using a single optical wavelength in a single mode fiber based on coherent detection techniques. This has a great impact on optical communication society, not only because the bit rate has upgraded from conventional 10Gb/s or 40Gb/s direct-detection link, but also the significant advances in the fundamental coherent communication technologies that enable future fiber capacity increase.

Different from conventional direct detection that only captures the amplitude information of the optical signals, coherent receiver detects both amplitude and phase information of the optical signals. Therefore, more advanced modulation formats (e.g. quadrature phase shift keying) can be used to increase the spectral efficiency. For example, in the current 100G implementation, it is based on single-core, single-mode fiber using single-carrier polarization-division multiplexed quadrature phase shift keying (PDM-QPSK) modulation format with associated coherent detection and digital signal processing (DSP) techniques [39][40].

Optical transmission of bit rates per-channel beyond 100G will soon be required to meet the increasing demand. With the same goal of increasing the overall channel capacity, many approaches have been proposed and investigated as shown in the Figure 1.10. The current 100G approach is also shown as a reference.

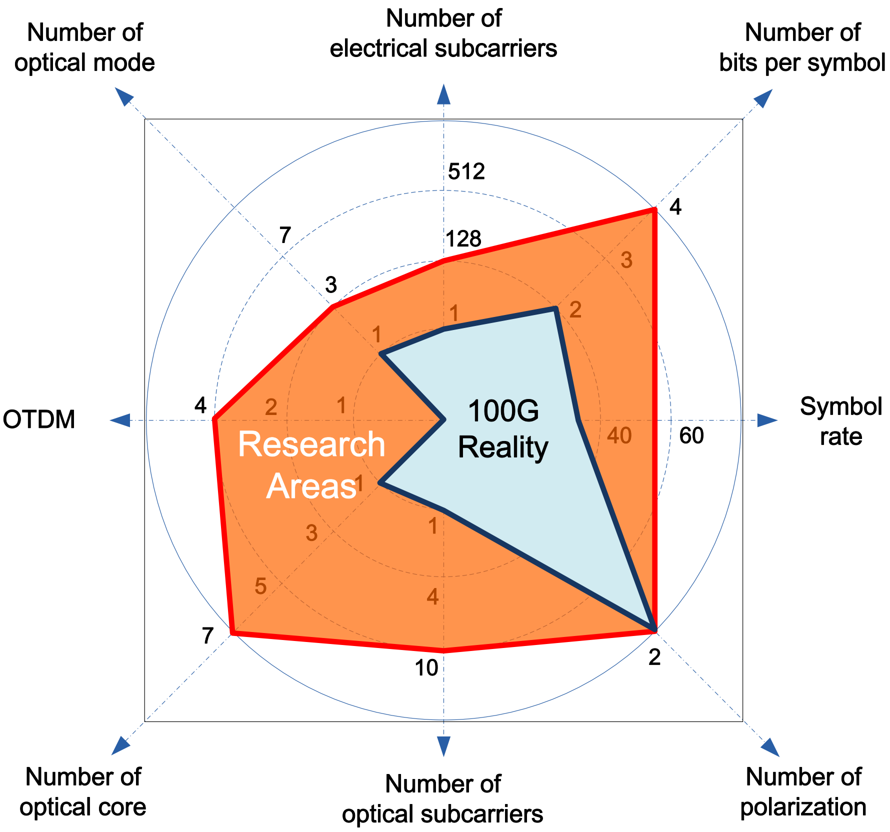

Figure 1.10. Research areas of increasing capacity beyond current coherent 100G technology.

Optical time division multiplexing (OTDM) is one of the classical approaches to increase the channel data rate by multiplexing several very narrow laser pulses in the time domain. However, this approach occupies a large amount of spectra resources, and has issues with the system stability, and therefore is limited in research laboratories at the current stage.

Spatial division multiplexing (SDM) that uses multi-core fiber (MCF) or few-mode fiber (FMF) and combined with multiple-input multiple-output (MIMO) signal processing is under very active investigations recently. Theoretical predictions and recent advances show promising results in terms of the special fiber fabrication and transmission performance [41][43]. However, because of the special design of these new fiber types, the associated E/O and O/E interfaces, optical amplifiers, and system integrations all need to be re-designed accordingly, which makes this approach a long way to go before the commercialization.

In the next few years, especially for the upcoming 400GE and 1TE standard, it is believed that the adopted approach will be implemented with existing technologies and components. According to this, three major dimensions are more practical for near-term industrial realizations.

As shown in Figure 1.10, the most straightforward way is to increase symbol rate to a higher speed. This requires the state of the art electronic technologies. Currently, symbol rates up to 40GBaud using differential phase shift keying (DPSK) have been deployed in the field [44], while 100Gbaud with NRZ is demonstrated in research experiments [45], and both demonstrations use direct detection schemes. Today’s 100Gb/s commercial systems or 400Gb/s dual-carrier prototypes are limited at 30Gbaud to transport QPSK or 16 quadrature amplitude modulation (16-QAM) signals in the coherent detection manner [46]. In research laboratories, 16-QAM signals with symbol rates up to 56Gbaud have been reported at the expense of reduced transmission distances [47].

The second dimension is to use higher level modulation formats, which achieves higher spectral efficiency. People are studying 16QAM or even higher level QAM formats over conventional QPSK format. However, the trade-off is the much higher required signal to noise ratio and receiver sensitivities, which limits the achievable optical reach [47].

The third approach is by grouping a number of tightly spaced optical subcarriers to form a so called *superchannel* signal. This approach increases the channel capacity while minimizing the need for high-level modulation formats and high baud rates, which may allow existing format, baud rate and components to be exploited. Therefore, this approach has attracted both research lab interests [48][49] as well as industrial interests with many field trails [50][51].

Nyquist-WDM [52][53] and coherent optical orthogonal frequency division multiplexing (CO-OFDM) [54] are the two main approaches to generate superchannel signals optically, and both of them are ideally orthogonal systems. We note that electrical OFDM has features similar to CO-OFDM although the sub-carriers are initially generated in the electrical domain [55][56].

For Nyquist-WDM superchannel systems, the ideal spectral shape of each subchannel is rectangular with the subchannel spacing equals to the baud rate B, as shown in Figure 1.11. Therefore, no inter-channel interference (ICI) exists. On the other hand, because of the rectangular spectrum, the time-domain pulse of each subchannel is *sinc* shape with zero-crossing point at integer times of symbol period T, which achieves Nyquist pulse with inter-symbol interference (ISI) free. In contrast, for CO-OFDM system, each subchannel is *sinc* shape in the frequency domain, and rectangular in the time domain. Therefore, theoretically both schemes achieve ICI and ISI free simultaneously [57][58].

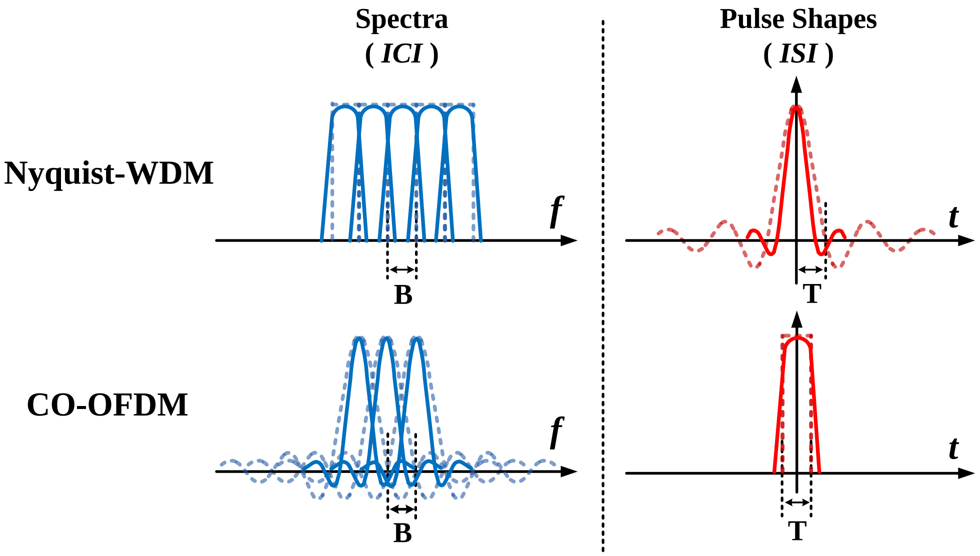

Figure 1.11. Spectra and pulse shapes for ideal (dash) and practical (solid) Nyquist-WDM and CO-OFDM systems.

However, in practical systems, neither of the two superchannel schemes is perfectly ICI and ISI free. For CO-OFDM systems, the generation and maintenance of rectangular time-domain pulse through the transmission system is very difficult, especially at higher baud rate. In addition, the subchannel (subcarrier) separation at the receiver side is not trivial that requires an FFT function implemented either in electrical domain [54][59] or optical domain [60][61]. For the electrical subcarrier separation case, a banded detection scheme is usually used by detecting more than one subcarrier per digital sampling, which further reduces the achievable baud rate per channel resulting from the limited ADC sampling rate.

For Nyquist-WDM systems, practical issues are raised by the requirement of perfect rectangular spectral shaping. Since the subchannels are closely packed at channel spacing equal to the baud rate with no guard band in between, any slight spectral imperfection results in strong ICI and degrades the system performance.

Conventional methods to mitigate ICI effects in Nyquist-WDM systems include pre-shaping the signal spectrum using optical [62] or digital [57] filters to approach a near-rectangular spectrum at the receiver. Alternatively, strong optical filters can be applied on each subchannel, followed by DSP to cancel the induced ISI in the time domain [63]. However, both methods still experience difficulties in the generation of required spectra, and ISI or ICI penalties occur at tight channel spacing conditions.

Therefore, in this dissertation, we introduce a novel “super-receiver” architecture to jointly detect and demodulate multiple subchannels, and mitigate the penalties associated with the limitations of creating ideal Nyquist-WDM spectra. Compared to conventional Nyquist-WDM systems, the proposed “super-receiver” scheme relaxes the stringent requirements of optical shaping filters, and also achieves better overall system performance. The detailed discussions will be given in Section 4.1.

1.3 Organization of Dissertation

The dissertation is organized as follows. After the introduction to research background and challenges in Chapter 1, Chapter 2 demonstrates a reconfigurable in-building small-cell cloud-RoF access system. Two small-cell network configurations (DAS: distributed antenna system, and FFR: fractional frequency reuse) are considered, and multiple-service (or multiple-operator) coexistence in the cloud-RoF access system is demonstrated based on the combination of RoF techniques and wavelength-division multiplexing (WDM) technologies.

Millimeter-wave cloud-RoF access system is introduced in Chapter 3. We will first discuss different optical mm-wave generation schemes, introduce different data modulation methods in the mm-wave RoF systems, and theoretically analyze the issues of vector signals transmission in different types of optical mm-wave RoF systems. Then we propose and demonstrate several novel system architectures that enable vector signal delivery in DSB-OCS mm-wave RoF systems. In addition, for a specific vector signal modulation format, duobinary (DB), we will design a novel RF receiver that reduces the receiver complexities to provide more robust system operations.

In Chapter 4, high-speed coherent optical transmission system is considered for long-haul core network applications. Based on superchannel coherent optical systems, a joint coherent receiver architecture with several joint digital signal processing techniques are proposed and demonstrated through both simulations and experiments. The performance of proposed joint detection scheme is evaluated under different system configurations and compared with conventional independent detection method.

The contributions of the research work are summarized in Chapter 5. Future research opportunities are also discussed in the end.

CHAPTER 2: RECONFIGURABLE SMALL-CELL MOBILE BACKHAUL

2.1 Reconfigurable Small-Cell Backhaul

2.1.1 Introduction to Distributed Antenna System and Frequency Reuse Scheme

As mentioned in the introduction, small-cell system with centralized processing power provides a cost-effective and power-efficient solution for the deployment of a large-scale small-cell system. By having the centralized processing power, more advanced and efficient network management is enabled. For example, both intra-cell and inter-cell interference can be cancelled based on coordinated multi-point transmission (CoMP) in the concept of network MIMO [11]. Therefore, we introduce another aspect of network management based on the centralized processing power of cloud-RAN and cloud-RoF systems.

Conventionally in a cloud-RAN (or a cloud-RoF system), a one-one logical mapping exists between a BBU and an active RAU. Hence, one BBU is logically assigned to generate a frame (or a RF waveform) for a given active RAU, although the mapping can change across time. We argue that such a mapping is sub-optimal for two reasons: (i) Generating a distinct radio signal for each small cell is important for capacity enhancing techniques such as dynamic frequency reuse (e.g. dynamic FFR [64]) or coordinated multi-point transmissions (e.g. CoMP in LTE [65]). However, such schemes are applicable only for static users. Indeed for mobile users, for whom the problem of handovers is exacerbated in small cells, a traditional DAS (distributed antenna system [66]) based scheme is more appropriate. In DAS, the same radio signal is transmitted to multiple small cells to provide increased coverage and diversity gain. (ii) When the traffic load is sparse in a given region, a single BBU can manage the load of multiple small cells, by serving them through a DAS. Whenever there is an opportunity to serve multiple small cells through a DAS, this reduces the number of BBUs and hence the processing (cores, DSPs, FPGAs) needed to manage a given set of RAUs, thereby resulting in energy savings in the cloud.

To demonstrate the difference between DAS and FFR, an example of 3-RAU configuration is illustrated in Figure 2.1 [67]. In the DAS scenario, the same signal from a single BBU is distributed to all RAUs to extend coverage especially for mobile users. However, all three mobile subscribers (MS) share the total bandwidth B, and each of the MSs occupies bandwidth of B/3. On the other hand, in the FFR scenario, different signals from 3 BBUs are transmitted to different RAUs to exploit frequency reuse. In this particular example (frequency reuse factor of 2), RAU1 and RAU3 will reuse the same spectrum in non-overlapped geographic regions without interference. Therefore, each one of the 3 MSs in different RAU areas occupies bandwidth of B/2. While DAS provides less hand-off complexity and better power efficiency to mobile users, FFR increases total system capacity especially for static users.

However, allowing the cloud-RAN or clou-RoF system to cater to heterogeneous user (static and mobile) and traffic profiles, while also leveraging energy savings, in turn requires the backhaul to be flexible enough to support one-one as well as one-many logical mappings between BBUs and RAUs.

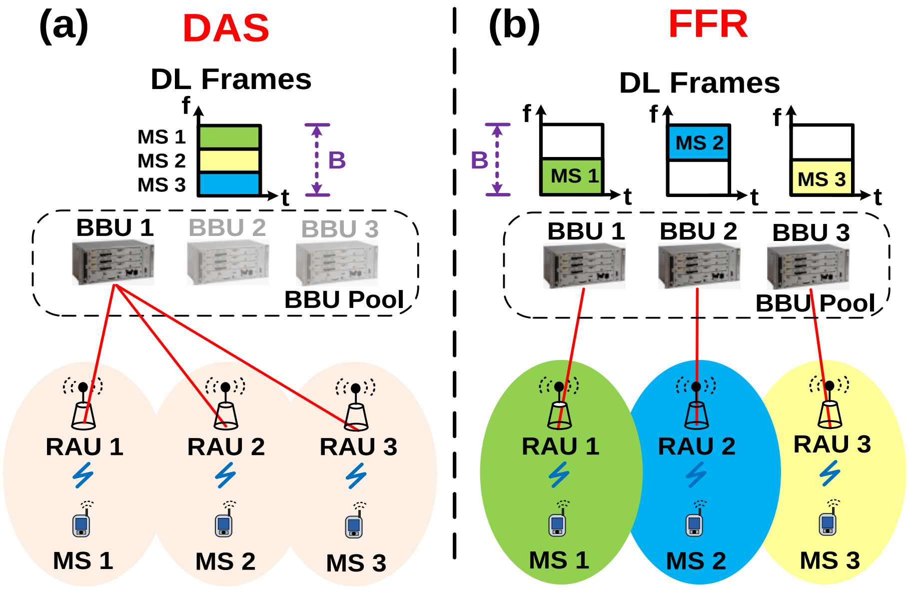

Figure 2.1. Illustration of (a) distributed antenna system (DAS) and (b) fractional frequency reuse (FFR) scheme for 3-RAU configuration.

2.1.2 System Design of Reconfigurable Small-Cell Backhaul

Towards the goal of accommodating heterogeneous user (static and mobile) and traffic profiles, we propose a cloud-RoF wireless access system with a flexible backhaul architecture. In addition, multiple-service and multiple operator coexistence in the backhaul network are enabled by the combination of radio-over-fiber and WDM techniques. The proposed system architecture (two-operator/3-RAU example) is shown in Figure 2.2.

In this example, Operator 1 uses DAS configuration while Operator 2 adopts FFR configuration. At the BBU pool, where the centralized digital processing power is located, the baseband data traffic from core networks is processed and up-converted to RF via BBUs. Since different operators and/or wireless services occupy different RF spectral bands, f_1, f_2, and f_3 represent the RF carrier frequencies of signals from different BSs. Notice that since Operator 2 uses FFR scheme, BS 2 and BS 4 occupies the same carrier frequency (f_2) but transmitting different information. Each downstream RF signal is then intensity modulated onto a different CWDM optical wavelength, λ_1, λ_2, λ_3, λ_4, respectively. Integrated RoF transceivers (Tx/Rx in Figure 2.2) for bi-directional intensity modulation and direct photodetection are commercially available to support RF bandwidth from DC to 6GHz [21]. Optical splitters (OS) and coarse wavelength division multiplexing (CWDM) multiplexers (MUX) are used at the BBU pool to split and multiplex the downlink and uplink signals. An optical switch with built-in independent on-off sub-switches is used to establish reconfigurable fiber-optic connections between the centralized BBUs and distributed RAUs. Notice that the switching functions can also be realized in the electrical domain by the virtualization of BBU pool.

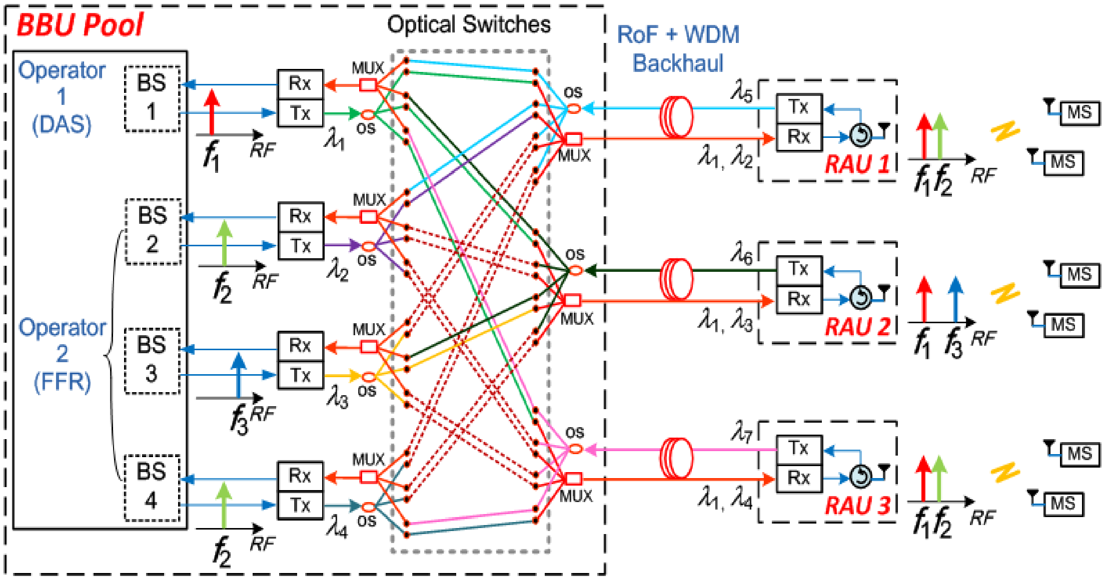

Figure 2.2. Reconfigurable small-cell cloud-RoF access architecture for multi-service/multi-operator coexistence.

By properly configuring the optical on-off switches in Figure 2.2, the signal from BBU1 on f_1 and λ_1 (from Operator 1) can be distributed to all three RAUs, as in a DAS scenario. To simultaneously emulate FFR scheme with a spectral re-use factor of 2 for Operator 2, the optical switches can be configured to distribute the signal from BBU2 on f_2 and λ_2 to RAU1, and signal from BBU3 on f_3 and λ_3 to RAU2, while the signal from BBU4 on f_2 and λ_4 is distributed to RAU3. After the optical switch, downstream signals are CWDM-multiplexed and delivered to several in-building RAUs via radio-over-fiber links. In the cloud-RoF architecture, multiple wavelengths carrying multiple RF signals from different operators are all detected simultaneously by a single photodetector (PD) at each RAU, yet without interference. This key receiver-side feature of the architecture is enabled by the integration of CWDM with RoF systems [68]. Following photodetection, the multiple RF signals on different carrier frequencies are transmitted wirelessly to mobile subscribers (MS), where RF carrier frequency selection is executed, enabling multi-service support. Finally, as shown in Fig. 3, upstream transmission on the same RF spectral bands is enabled by CWDM wavelengths λ_5 to λ_7 using the switching mechanism above.

Therefore, the proposed architecture provides flexible network configuration to different operators or services independently. Infrastructure sharing among multiple operators and multiple services is enabled by radio-over-fiber and WDM techniques to further reduce the cost. The theoretical analysis of multi-service/multi-operator coexistence is given in the following section.

2.2 Multi-Service/Multi-Operator Coexistence

2.2.1 **Theoretical Analysis**

In the reconfigurable cloud-RoF architecture, multiple wavelengths carrying multiple RF signals from different operators are detected simultaneously by a single photodetector (PD) at each RAU, yet without interference. This key receiver-side feature of the novel architecture can be analyzed with a dual-wavelength, dual-service example, as follows: the electrical field of the optical multiplexed signals can be represented as:

$$E(t) = [D + \gamma S_1(t)] \exp\left(j\omega_{opt1} t\right) + [D + \gamma S_2(t)] \exp\left(j\omega_{opt2} t\right) \ , \qquad (2.1)$$

where $S_1(t)$ and $S_2(t)$ denote the RF signals carried on wavelength λ_1 and λ_2 (angular frequencies ω_{opt1} and ω_{opt2}, respectively), D is the DC bias needed for intensity modulation, and γ represents the optical modulation index. After fiber transmission to the RAU, the signals are directly detected by a single PD. The generated electrical current is then given by:

$$\begin{aligned} I(t) = \|E(t)\|^2 = \left([D + \gamma S_1(t)]^2 + [D + \gamma S_2(t)]^2\right) \\ +\left(2[D + \gamma S_1(t)][D + \gamma S_2(t)] cos\left(\omega_{opt1} - \omega_{opt2}\right) t\right) . \qquad (2.2) \end{aligned}$$

From Equation (2.2), we observe that the transmitted RF signals can be recovered from the expansion of the first term, while the second term represents the crosstalk between the two RF signals, carried on a radio frequency that is determined by the CWDM channel spacing. By proper selection of CWDM wavelengths, this crosstalk term will fall beyond the electrical bandwidth of the receiver-side PD and can thus be ignored. Consequently, the proposed architecture can enable infrastructure sharing among multiple operators without interference.

2.2.2 Experimental Validation

The experimental setup for validating the proposed multi-operator, multi-service small-cell cloud-RoF backhaul architecture is shown in Figure 2.3 for the case of two operators and a single RAU.

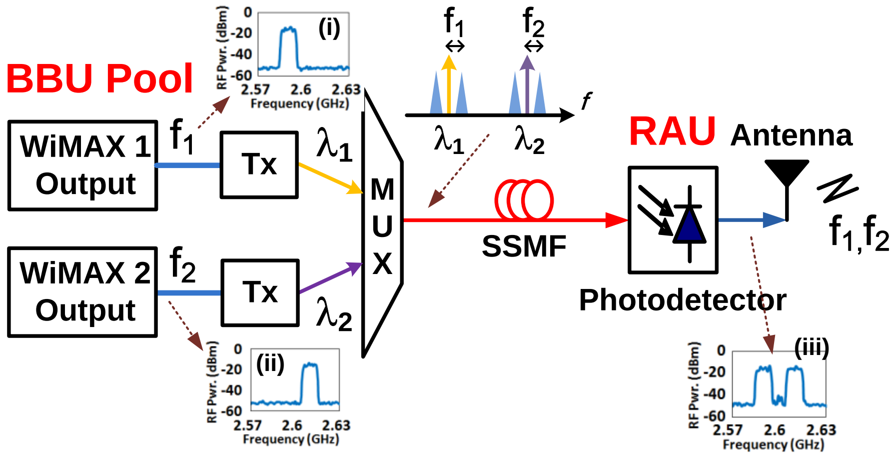

Figure 2.3. Validation of optical infrastructure sharing between two operators.

Specifically, two commercial WiMAX BSs are first used to generate independent 10MHz radio signals centered on two different RF carriers (f_1 = 2.59GHz, f_2 =2.61GHz). The measured electrical spectra at the BS outputs are shown in insets (i) and (ii). Following intensity modulation onto wavelengths λ_1 = 1550nm and λ_2 = 1570nm, the double sideband optical signals are CWDM-multiplexed and transmitted over 100m of standard single mode fiber (SSMF), corresponding to an in-building small-cell backhaul scenario, and photodetected by a 3-GHz PD. The measured electrical spectrum following the PD is shown in inset (iii) of Figure 2.3, confirming the removal of the unwanted interference term, as described in Equation (2.2). Finally, following single-hop wireless transmission of 2-15m, the downlink throughput was measured by a network bandwidth testing tool *iperf*, which computes successfully recovered layer-4 packets per unit time under the User Datagram Protocol (UDP). For the transport-layer throughput measurements, commercial WiMAX BSs and laptops equipped with commercial WiMAX client cards were used. The measured results are shown in Figure 2.4.

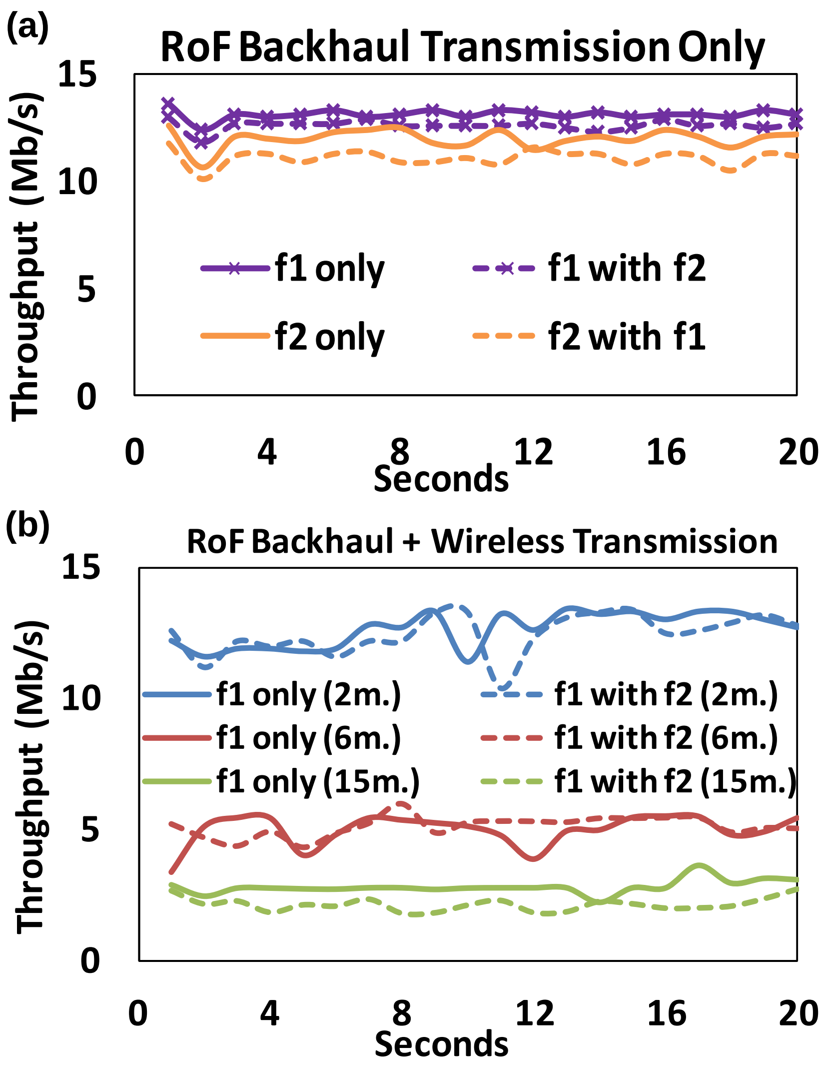

Figure 2.4. (a) measured downlink throughput for small-cell optical backhaul transmission only; (b) measured downlink throughput after optical backhaul and single-hop wireless transmission.

For the optical backhaul only case (Figure 2.4(a)), stable 12-13Mb/s downlink throughputs were observed, with only minimal performance degradation due to the coexistence of signals on f_1 and f_2. A similar trend was observed for the optical plus wireless transmission cases (Figure 2.4(b)), where, due to wireless transmission loss, multipath, and shadowing effects, throughput decreased from 12Mb/s to just under 3Mb/s as wireless transmission distance was increased from 2m to 15m. This significant throughput degradation within short wireless transmission distance was due to intentional attenuated RF transmitting power at RAU.

From the results, we conclude that no performance degradation is introduced by transmitting multiple services in the shared backhaul infrastructure based on radio-over-fiber and WDM techniques.

2.3 In-Building Small-Cell Cloud-RoF Testbed and Results

Based on the proposed multi-service reconfigurable architecture, an in-building small-cell cloud-RoF testbed was set up as shown in Figure 2.5(a). In this case, 4 WiMAX BBUs were centralized at the BBU pool, while 3 RAUs were distributed in the building as shown on the floor plan of Figure 2.5(a). As shown in Figure 2.5(b), 1 WiMAX BBU (f_1 = 2.57GHz) is used in the DAS configuration to serve 2 mobile users MS1 and MS2 along a moving path denoted by checkpoints L1 - L7. The remaining WiMAX BBUs are used in the FFR configuration (f_2 = 2.61GHz, f_3 = 2.59GHz; reuse f_2 for BBU2 and BBU4), serving two static users (SS1 and SS2.) Both DAS and FFR configurations were thus running simultaneously. The output RF signals of four BSs are carried on four CWDM wavelengths ($\lambda_1, \lambda_2, \lambda_3, \lambda_4$) = (1490nm, 1510nm, 1530nm, 1550nm), respectively, with 4dBm per-λ optical launch power.

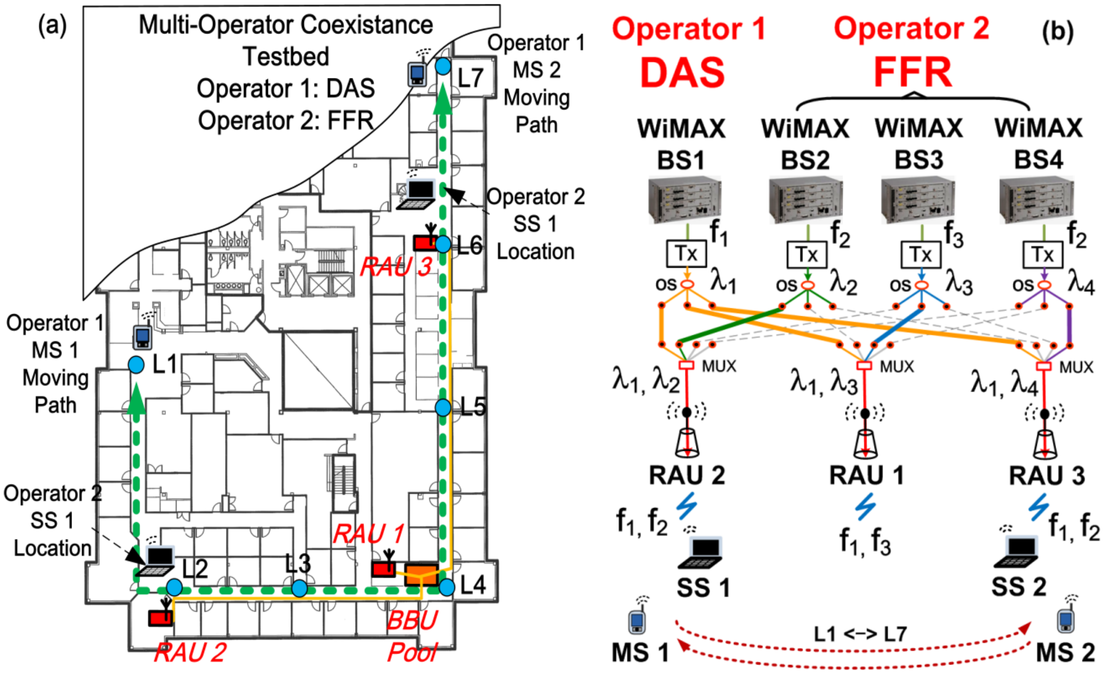

Figure 2.5. (a) In-building multi-operator co-existence testbed; (b) detailed network configuration (with only downlink shown here)

The measured downlink throughputs for the DAS and FFR scenarios are shown in Figure 2.6 (a) and (b), respectively. For Operator 1, since the DAS configuration is used, the mobile users experience no degradation in the steady 6Mb/s throughput while moving across three small cells (L1 to L7, and back), even at the cell edges, highlighting the key coverage benefits of DAS. For Operator 2, since FFR with a reuse coefficient of 2 was exploited for static users, the system throughput is doubled to 12Mb/s for each user, which demonstrates the capacity benefits of this scheme. Consequently, this architecture enables both operators to simultaneously run different small-cell backhaul scenarios by sharing the in-building optical infrastructure, without interference.

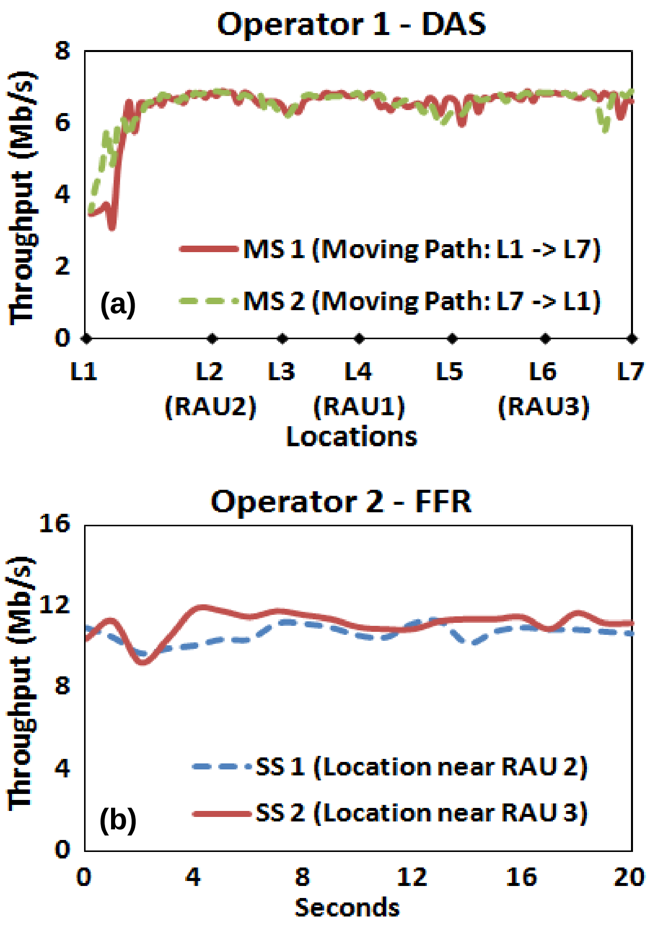

Figure 2.6. (a) Measured downlink throughput of mobile users of Operator 1 at different locations; (b) Measured downlink throughput of static users of Operator 2.

CHAPTER 3: MILLIMETER-WAVE CLOUD-ROF ACCESS SYSTEMS

3.1 Theoretical Analysis of Signal Transmission in Mm-Wave Cloud-RoF Systems

In this section, different input signal formats are categorized and the issues of vector signal transmission in mm-wave RoF systems will be discussed with theoretical analysis.

As mentioned previously in Section 1.2, double-sideband optical-carrier-suppression (DSB-OCS) scheme is the most widely used optical mm-wave generation method. Compared to the direct modulation scheme, the DSB-OCS scheme only requires half of the electrical bandwidth for mm-wave generation, which is very important for high carrier frequency such as the mm-wave band. In addition, compared to the single sideband (SSB) optical mm-wave generation method, DSB-OCS provides higher optical to electrical conversion efficiency after photodetection and also achieves more stable operation.

Two typical DSB-OCS optical mm-wave generation schemes are shown in Figure 3.1. For the first method, Figure 3.1 (a), a dual-arm Mach-Zenhder modulator (MZM) is driven by a 30GHz RF signal at one arm, while the other arm is driven by the same RF source except after a 180 degree phase shift. The DC bias is at the minimal intensity-output point $V\pi$. Therefore, the generated optical mm-wave spectrum has double optical sidebands with the central carrier suppressed, which is shown in the inset of Figure 3.1 (a). The detailed theoretical derivation of this DSB-OCS generation method can be found in reference [36].

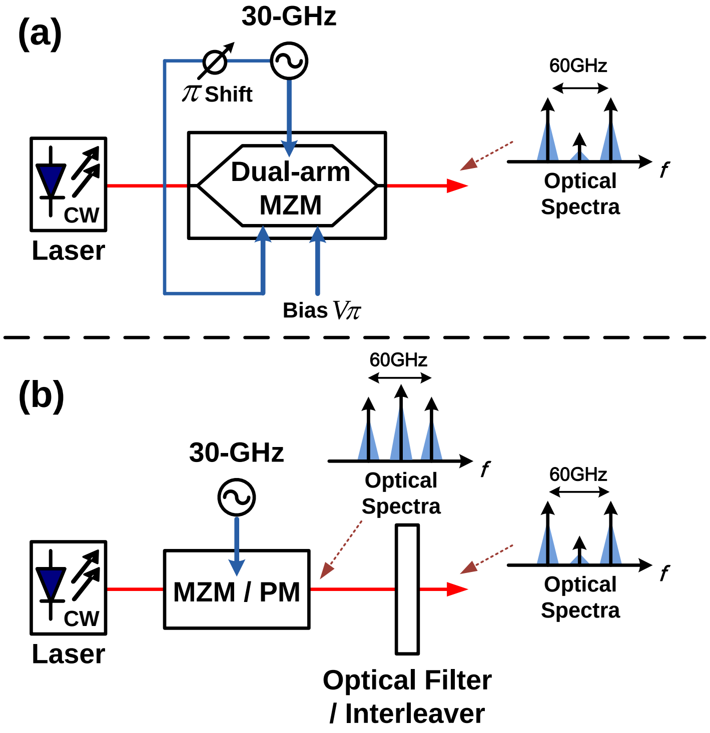

Figure 3.1. Two DSB-OCS optical mm-wave generation methods. (a) Driving a dual-arm MZM at a specific point; (b) Driving a MZM or PM plus an optical filter.

For the second DSB-OCS optical mm-wave generation method, Figure 3.1 (b), a MZM or a phase modulator (PM) is driven by a 30GHz RF signal to generate multiple coherent optical subcarriers. Then an optical filter or an optical interleaver is used to suppress the center optical carrier to generate the DSB-OCS optical mm-waves. Compared to the first generation method, which requires dedicated biasing and phase shifting, the second generation method is easier and more robust. Therefore, the second method is mostly used in this thesis.

To modulate the data information on top of the DSB-OCS optical mm-waves, two approaches are commonly used: the dual-stage and single-stage modulation methods, as illustrated in Figure 3.2. Although both approaches modulate data on two optical sidebands as shown in the generated optical mm-wave spectra, the recovered signals after transmission and photodetection are very different depending on different modulation formats of the input signals. Therefore, in the following section, different types of signal modulation formats are differentiated and their performances are compared theoretically in both dual-stage and single-stage DSB-OCS optical mm-wave systems.

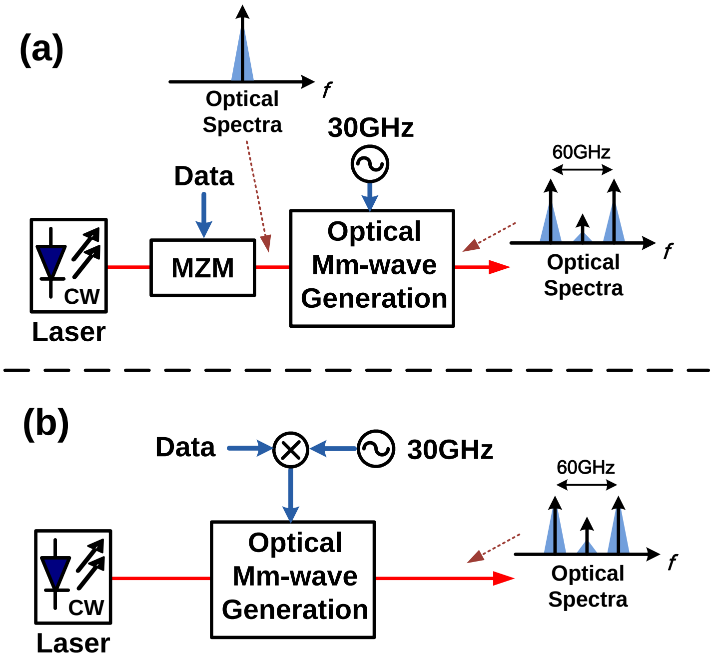

Figure 3.2. Two methods of modulating data onto DSB-OCS optical mm-waves: (a) Dual-stage modulation; (b) Single-stage modulation.

First of all, we define several different types of input signal modulation formats, as categorized in Table 3.1. The two main categories are digital baseband

and analog intermediate frequency (IF) signals that represent two different applications at 60GHz mm-wave band. For the digital baseband signal, it is targeted at specified services at 60GHz band, for example the HD-wireless transmission and very-high-speed data transmission at 60GHz. These services are originated at baseband in the digital formats, and then upconverted to the 60GHz band for wireless transmission.

Table 3.1. Different input signal formats of mm-wave RoF systems.

Digital Baseband		***Analog Intermediate Freq.***	
Scalar Signals	**Vector Signals**	**Single-Carrier**	**Multi-Carrier**
OOK, ASK, etc.	BPSK, QPSK, Duobinary, m-QAM, etc.	QPSK IF, m-QAM IF, etc.	OFDM on IF, etc.

For the analog IF signal format, since the 7GHz unlicensed band at 60GHz can be divided into several sub-bands according to the ECMA 387 standard [16], the existing wired and wireless services at lower carrier frequencies can be aggregated and fit into one of the 60GHz sub-bands to provide multiple services through the 60GHz channel simultaneously. In this case, the existing services at lower carrier frequencies are considered as analog signals carried on intermediate frequencies (IF).

For the digital baseband signals, they are further categorized into scalar signals and vector signals as shown in Table 3.1. For scalar signals, the modulation is done only on the amplitude of the signal, like on-off keying (OOK) and amplitude shift keying (ASK). For vector signals, the modulation is done on both amplitude and phase, which provides higher spectral efficiency than the scalar modulation formats. From the constellation representations, vector signals have both in-phase and quadrature components, while scalar signals only have in-phase components.

The reasons to differentiate the two types of baseband modulation formats are due to their different optical modulation and detection schemes, as illustrated in Figure 3.3.

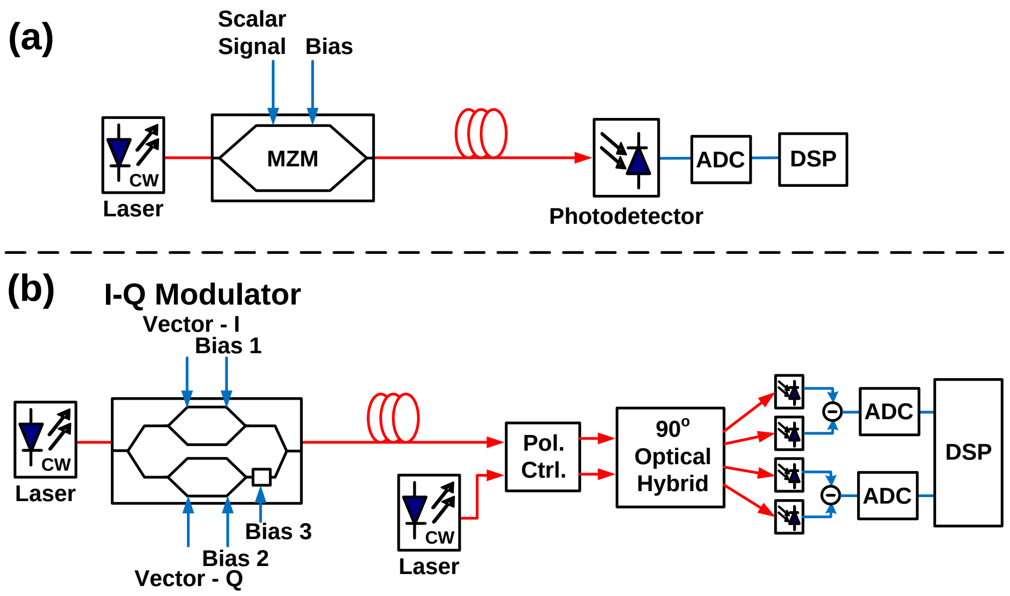

Figure 3.3. Optical modulation and detection for scalar (a) and vector (b) signals.

For the scalar signal optical modulation, a single MZM is used to generate optical scalar signal by biasing the electrical driving signal at the linear regime. However, for vector signals, an I-Q modulator is needed to modulate both in-phase and quadrature components on to the optical carrier.

The optical detection or optical demodulation is also very different between the two types of modulation formats. For conventional scalar signal detection, a simple photodector (PD) is used to directly detect the amplitude variations of the optical carrier and ignore the optical phase change. However, for the vector signal, since information is modulated on both amplitude and phase of the optical carrier, a coherent optical receiver is needed to fully recover the original signal. As shown in Figure 3.3, a typical coherent optical receiver is composed of a local oscillator (LO) laser, a polarization controller, a 90 degree optical hybrid, and four balanced photodetectors with subsequent analog to digital convertors (ADC) and DSP functions. Overall, the generation and detection of vector signals require much higher system complexities.

On the other hand, for the analog IF input signals, since all the information is contained in the time-varying amplitude, the optical modulation and demodulation is almost identical to the digital baseband scalar case. However, the analog IF signals require higher linearity of the optical transceivers to maintain the integrity of signals.

In the following sections, the challenges of vector and analog IF signal transmission in DSB-OCS mm-wave RoF systems are explained through theoretical derivations. We first separate the discussions for two different optical mm-wave upconversion methods: 1) dual-stage optical mm-wave upconversion; 2) single-stage optical mm-wave upconversion.

As shown in Figure 3.2(a) previously, for the dual-stage optical mm-wave upconverison, the data is modulated onto an optical carrier through a single MZM at the first stage (first consider the case of scalar input signals or analog IF input signals). The modulated optical carrier after the first stage (MZM) can be represented in the phasor form as shown in Equation 3.1:

$$E_{S1-MZM}(t) = (1 + \gamma \cdot S(t))\exp(j\omega_0 t)\,. \qquad (3.1)$$

γ represents the modulation index of the MZM. 1 means that the signal *S(t)* is biased at the middle point of the MZM linear regime and its amplitude is normalized to 1. Exp($j\omega_o t$) is the phasor form of the optical carrier at angular frequency of ω_o.

Notice that for input signal *S(t)*, it is represented differently for different signal formats. For the baseband scalar signal, it can be represented as:

$$S_{bb-scalar}(t) = I(t)\,. \qquad (3.2)$$

For the analog IF signals, the single-carrier signal is represented as Equation 3.3, and the multi-carrier signal (e.g. OFDM signal) is represented as Equation 3.4:

$$S_{IF-sc}(t) = I(t)\cos(\omega_{IF} t) + Q(t)\sin(\omega_{IF} t)\,, \qquad (3.3)$$

$$S_{IF-mc}(t) = \sum_{k=-(N-1)/2}^{(N-1)/2} \left[I_k \cos(\omega_{IF} + k\Omega)t + Q_k \sin(\omega_{IF} + k\Omega)t \right]. \qquad (3.4)$$

ω_{IF} is the IF carrier angular frequency, while I(t) and Q(t) are the in-phase and quadrature components, respectively. For the multi-carrier case, there are totally N subcarriers centered at ω_{IF}, and the subcarrier spacing is Ω.

However, for the vector baseband input signal case, the data is modulated onto the optical carrier through an I-Q modulator at the first stage. The modulated optical carrier after the first stage (I-Q modulator) can be represented as Equation 3.5 in the phasor form:

$$E_{S1-IQ}(t) = S(t)\exp(j\omega_0 t) \tag{3.5}$$,

while the input baseband vector signal *S(t)* is represented as:

$$S_{bb-vector}(t) = I(t) + j \cdot Q(t)\,. \tag{3.6}$$

At the second stage, two coherent optical carriers are generated through a DSB-OCS method while both carriers carrying the modulated data, which can be represented as $E_{S2\text{-}MZM}$ (Equation 3.7) and $E_{S2\text{-}IQ}$ (Equation 3.8), for scalar (or analog IF) and vector input signal cases respectively:

$$E_{S2-MZM}(t) = (1 + \gamma \cdot S(t))\left[\exp(j(\omega_0 - \Delta)t) + \exp(j(\omega_0 + \Delta)t)\right], \tag{3.7}$$

$$E_{S2-IQ}(t) = S(t)\left[\exp(j(\omega_0 - \Delta)t) + \exp(j(\omega_0 + \Delta)t)\right]. \tag{3.8}$$

Δ is the frequency of the driving RF signal, which is 30GHz in this 60GHz optical mm-wave generation case. After the optical fiber transmission, ignoring the fiber channel impairments, the optical mm-wave signals are detected by a high-speed PD to generate the electrical mm-wave signals. The generated electrical signals at 60GHz are represented as Equation 3.9 and Equation 3.10 for scalar (or analog IF) and vector input signal cases respectively:

$$\begin{aligned} E_{D-S\_RF\_MZM} &= \left\|E_{S2-MZM}(t)\right\|^2 = (1 + \gamma \cdot S(t))^2 \cos(2\Delta t) \\ &= (1 + \underline{2\gamma \cdot S(t)} + \underline{\underline{\gamma^2 \cdot S^2(t)}})\cos(2\Delta t) \end{aligned}, \tag{3.9}$$

$$E_{D-S\_RF\_IQ} = \left\|E_{S2-IQ}(t)\right\|^2 = S^2(t)\cos(2\Delta t)\,. \tag{3.10}$$

Notice that $\cos(2\Delta t)$ represents the generated RF carrier at 60GHz. For the baseband scalar or IF analog input signal case, Equation 3.9, the generated signal have several components: 1 is the pure RF carrier, $2\gamma S(t)$ is the desired data information that is recovered after RoF transmission and detection, and $\gamma^2 S^2(t)$ is the interference term generated after photodetection. This interference term shows different effects depending on different signal formats, which is shown in the generated 60GHz RF spectra in the Figure 3.4. For the baseband scalar signals, the interference components sit below the original data spectra. For analog IF input signals, the interference terms are mainly located at the center and on both sides of 60GHz with twice of the IF spacing. In this case, there is no interference to the in-band signals, but may cause problems to other wireless signals on other channels. However, for baseband vector input signals, Equation 3.10, the original information is totally lost with only the interference term appears around 60GHz.

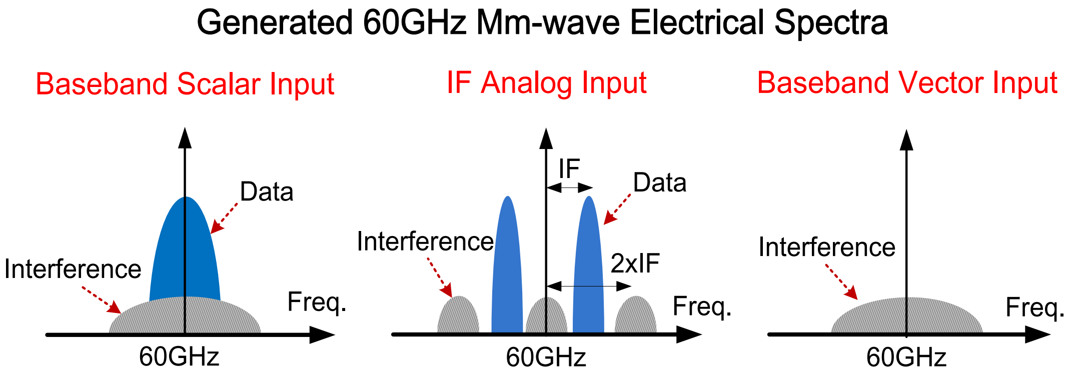

Figure 3.4. Generated 60GHz RF spectra after RoF transmission and detection for different input signal formats in the dual-stage DSB-OCS optical mm-wave upconversion scenario.

Next we consider the single-stage optical mm-wave upconversion scenario. For the single-stage case, we assume the input signal formats are the same as the dual-stage case with three different types. At the optical mm-wave upconversion stage, the input signal is first mixed with the 30GHz RF clock, and then drive a MZM or PM, as shown previously in Figure 3.2(b).

The input signal after mixing with 30GHz RF clock is represented as:

$$E_{S-S\_Input} = S(t)\cos(\Delta t)\,. \tag{3.11}$$

After single-stage DSB-OCS optical mm-wave upconversion, the generated optical mm-wave can be represented as:

$$E_{S-S\_Optical}(t) = S(t)\left[\exp(j(\omega_0 - \Delta)t) + \exp(j(\omega_0 + \Delta)t)\right]. \tag{3.12}$$

After photodetection, the generated RF signal at 60GHz is

$$E_{S-S\_RF} = \left\| E_{S-S\_Optical}(t) \right\|^2 = S^2(t)\cos(2\Delta t)\,. \tag{3.13}$$

Therefore, for the single-stage optical mm-wave generation scheme, the modulated data cannot be successfully recovered after photodetection because of the square of original signal.

However, among all the input signal formats, the OOK signal is an exception because the two-level (0, 1) property maintains after the square function. This is why in the conventional mm-wave RoF systems, OOK signal is the only modulation format that can be transmitted in any kind of DSB-OCS upconversion scheme (either single-stage or dual-stage).

The transmission conditions for different input signal formats in both single-stage and dual-stage DSB-OCS optical mm-wave upconversion schemes are summarized in Table 3.2.

As we can see, except OOK signal, all other signals experience interferences when transmitting through the DSB-OCS mm-wave RoF systems. Some of the signals are even impossible to be recovered. Therefore, in the following sections, we propose several novel methods that enable baseband vector and analog IF signal delivery over DSB-OCS mm-wave RoF systems.

Table 3.2. Feasibility of different signal format transmission in DSB-OCS RoF systems.

	DSB-OCS Optical Mm-Wave Upconversion Methods	
Input Signal Formats	**Single-Stage**	**Dual-Stage**
OOK	Yes	Yes
Baseband Scalar (except OOK)	Yes / with Interference	Yes / with Interference
Baseband Vector	No	No
Analog IF	No	Yes / with Interference

3.2 OFDM Signal Transmission in DSB-OCS Mm-Wave RoF Systems

Orthogonal frequency division multiplexing (OFDM) signal is a multi-carrier signal that consists of many closely spaced orthogonal sub-carriers. Therefore, higher spectral efficiency is achieved compared to single-carrier modulation formats. OFDM modulation format is widely used in both wired (e.g. ADSL, digital cable TV, etc.) and wireless (e.g. WiFi, WiMAX, 4G-LTE, etc.) communications.

In our experiments, we take the OFDM signal as the input signal to the mm-wave RoF system. As mentioned previously, OFDM signal is considered as one type of IF analog signal.

As shown in Table 3.2, analog IF signal cannot be transmitted directly in the single-stage DSB-OCS mm-wave RoF systems. For the dual-stage DSB-OCS scheme, analog IF signal can be transmitted, but with interferences.

Therefore, we propose two novel schemes that enable analog IF signals (i.e. OFDM signals) to be transmitted through single-stage upconverted DSB-OCS mm-wave RoF systems, and the same concept can be used for other types of input signals.

3.2.1 **LO Power Feedthrough Scheme**

The first scheme is based on the LO power feedthrough effect of a mixer. The proposed system architecture is shown in Figure 3.5 [69][70].

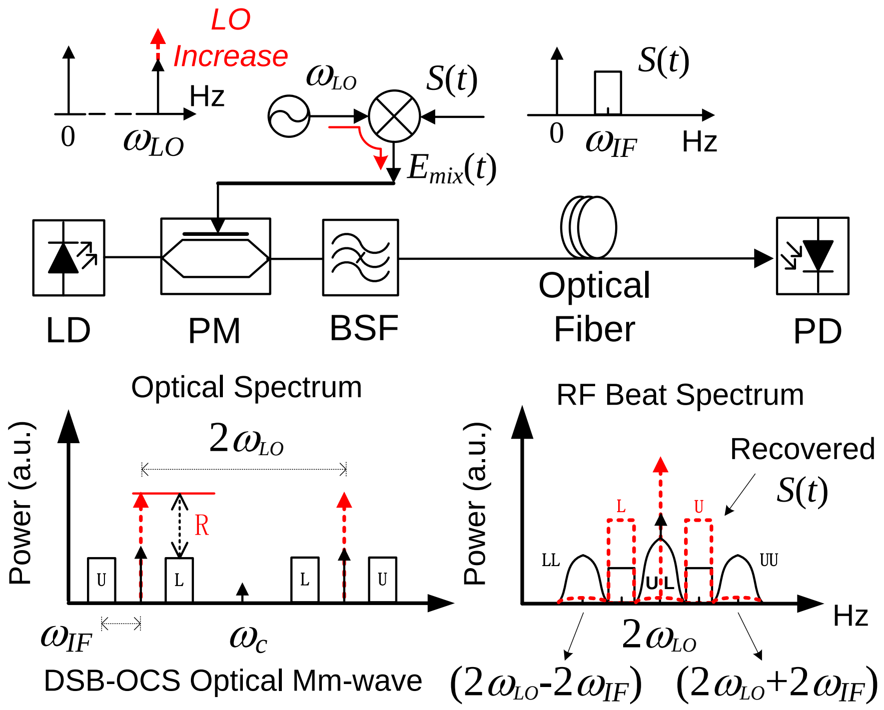

Figure 3.5. Analog IF signal delivery over single-stage DSB-OCS optical mm-waves through LO power feedthrough.

The input signal S(t) is an OFDM signal carried on an IF, as shown in Equation 3.4. This analog IF signal is mixed with an electrical local oscillator (LO) at ω_{LO} with field intensity E_{LO}. We notice that for a practical RF mixer, LO power will feed into the RF output port through the power leakage. Assuming the leakage ratio is r, the upconverted RF signal can be expressed as:

$$E_{mix}(t) = [S(t)(1-r)+r]E_{LO}\cos\omega_{LO}t = [A+S(t)]E'_{LO}\cos\omega_{LO}t\,, \qquad (3.14)$$

where $A=r/(1-r)$, and $E_{LO}'=(1-r)E_{LO}$. Then the single-stage DSB-OCS optical mm-wave signal is generated as shown in Figure 3.5. The mixed signal is used to modulate a continuous wave (CW) from a laser diode (LD) by using an externally optical phase modulator (PM). An optical bandstop filter (BSF) is used to suppress the center optical carrier to achieve the DSB-OCS scheme.

As illustrated in the inset of Figure 3.5, the resulting optical carriers have upper and lower optical sidebands spaced at $2\omega_{LO}$, and each of them carries the OFDM signals on two IF bands: an upper IF band (U) and a symmetric lower one (L) as the image copy. Here we define **R** as the power ratio between the optical carrier and the IF signal. After optical fiber transmission and direct detection at a photodetector (PD), the generated electrical signal at $2\omega_{LO}$ is given by:

$$E_{RF}(t) = E_0{}^2 E'_{LO}{}^2\, \beta^2 [A^2 + 2A\cdot S(t) + S^2(t)]\cdot \cos(2\omega_{LO}t)\,, \qquad (3.15)$$

where E_0 is the transmitted electrical field of the CW light, and β is the phase modulation index. The term $2A\cdot S(t)$ is the desired OFDM IF signal that has been recovered and enhanced by the LO power feedthrough. As increasing the feedthrough LO power, it is equivalent to increase the power ratio **R**, and therefore enhancing the beating between the DSB optical carriers to recover the original signal. In the conventional case of ignoring the LO feedthrough power, the $2A\cdot S(t)$ term is zero, and the inter-band interferences (IBI) term: $S(t)^2$ is dominant, shown as UL, UU, and LL in Figure 3.5, which is caused by the beating between L and U bands. We notice that the IBI can be suppressed by further increasing the LO power. In this case, LO input power could be enlarged to the extent that the mm-wave mixer starts working at gain-saturation region so as to decrease the IBI and increase the signal to interference ratio.

To validate the proposed scheme, an experimental demonstration is conducted as shown in Figure 3.6. The tested vector signal is a tri-band 16QAM-OFDM signal.

The IFs for three different bands are 60MHz, 120MHz, 180MHz, respectively, and each IF carries a 250Mb/s data, which is generated by an arbitrary waveform generator (AWG). After DSB-OCS optical mm-wave generation and transmission over 100-km standard single-mode fiber (SSMF) and 5-meter wireless distance, this 60GHz RF signal is down-converted to IF band, and then sampled by a digital phosphor oscilloscopes (DPO) for off-line demodulation.

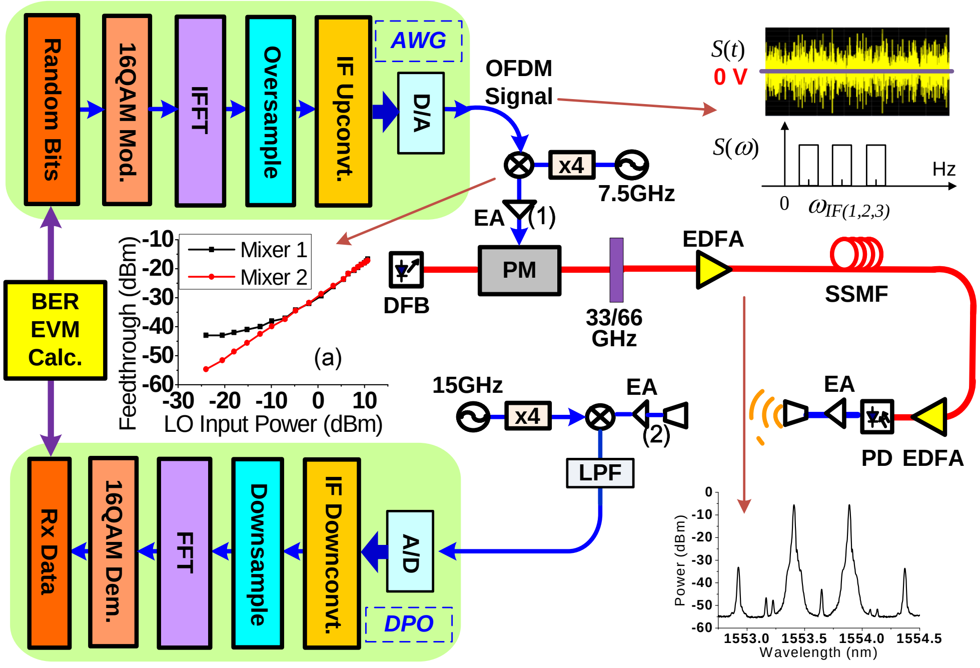

Figure 3.6. Experimental setup of tri-band 16AM-OFDM signal transmission over single-stage DSB-OCS mm-waves RoF system through LO power feedthrough.

To study the LO power feedthrough effect, we characterized two 30GHz RF mixers from different manufacturers, and the measured feedthrough power versus input LO power is shown in the inset (a) of Figure 3.6. About 30dB isolation (from LO port to RF port) was observed when the input LO power is between -10 and +10 dBm, and the feedthrough power was increased linearly with the LO power.

Although the feedthrough power is low, the experimental results show that this small amount of feedthrough power is sufficient to recover the original analog IF signals.

Figure 3.7(a) illustrates the measured RF power of the electrically upconverted 16QAM-OFDM signal and the 30GHz RF carrier at different LO input power. In general, power ratio R increases as increasing LO input power. At the beginning, before LO power rises up to -8dBm, the conversion gain of the mixer keeps increasing, which enhances R dramatically. After then, the mixer starts to working at the gain-saturation region, in which the signal power will stop increasing while LO power rises. However, when further enlarging the LO input power, after certain threshold (around 3dBm), the electrical amplifier (EA) after the mixer starts to saturate, and therefore suppresses the upconverted signal power. Figure 3.7(b) shows the measured RF power of the desired signal (U) and the IBI tone (UU) after a PD. When the RF power of LO is low, the power of signal band is small, and the feedthrough power is not high enough to give a better beating efficiency at the PD. As the LO power increases, the signal power after beating is enhanced because of higher original signal power as well as stronger beating with optical carrier. However, when too much LO power is injected, the saturation would in turn decrease the signal power.

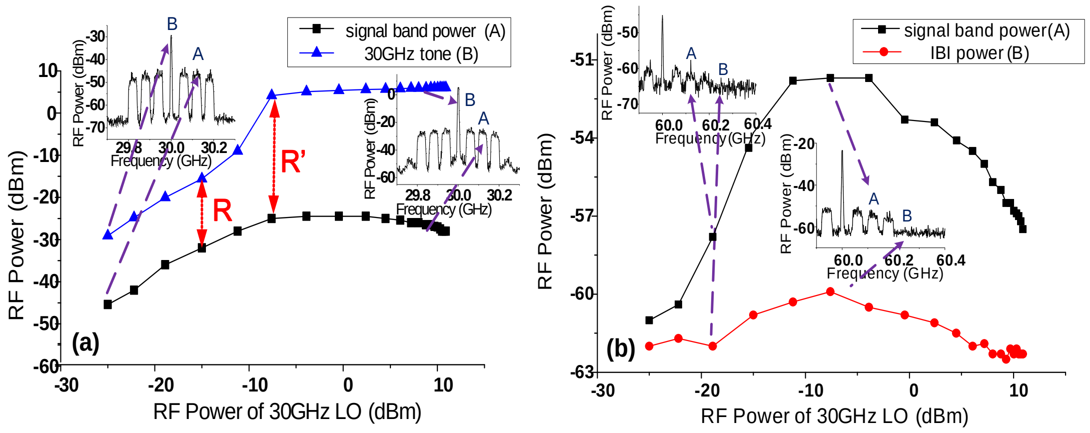

Figure 3.7. RF power of the 30GHz carrier and the upconverted OFDM signal (a) and the downconverted OFDM signal and IBI term (b) versus different LO input power measured at the point (1) and (2) in Figure 3.6, respectively.

Figure 3.8 shows the experimental results. Firstly, we calculated the received error vector magnitude (EVM) value for back-to-back (BtB) case under different LO input power, and found out the optimal LO power is around 0dBm, as shown in Figure 3.8(a). Then we fixed this LO power and tested the system performance under different conditions. For a 3-meter wireless transmissiondistance, the received EVM value versus different transmitted RF power for both BtB and 100km fiber transmission cases are shown in Figure 3.8(b). The transmitted RF power is measured before the transmitter horn antenna with 15dBi gain. After 100km fiber transmission, there is a big performance gap compared to the BtB case because of the amplified spontaneous emission (ASE) noise loaded at the erbium doped fiber amplifier (EDFA) used before the receiver to compensate the 20dB loss after 100km fiber transmission. Figure 3.8(c) shows the EVM results after 100km fiber transmission when the transmitted RF power was fixed to 2.8dBm, and the wireless transmission distance was scanned from one to five meters. It shows the EVM value degenerates with longer wireless distance because of the strong propagation loss at 60GHz. Finally, after 100-km fiber and 5-meter wireless transmission, the EVM value of 14.8% was achieved.

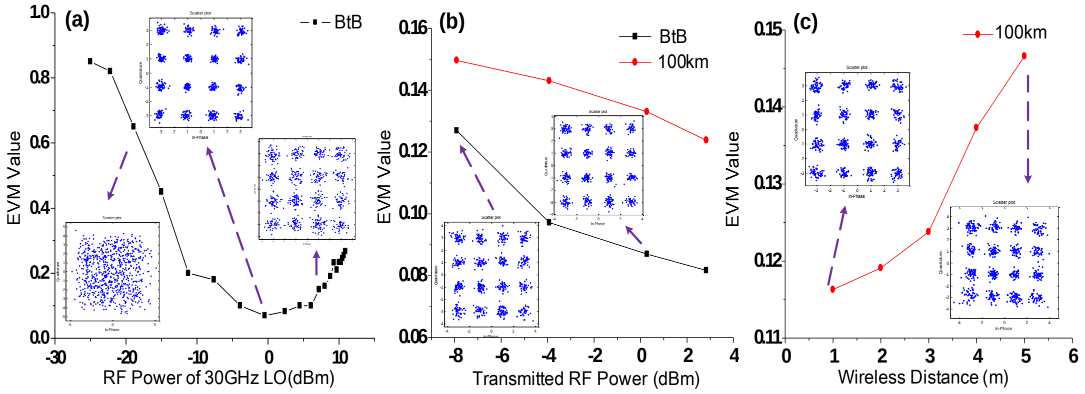

Figure 3.8. (a) BtB Demodulated EVM vs. 30GHz LO RF power; (b) EVM vs. transmitted RF power for BtB and 100km SSMF fiber transmission; (c) EVM vs. wireless distance after 100km SSMF fiber transmission.

Therefore, from the experimental results, we conclude that by taking advantage of the LO power feedthrough effect, the power of optical sideband carriers is enhanced that enables the analog IF signal transmission in single-stage DSB-OCS mm-wave RoF systems. However, this method depends on the mixer characteristics and the optimal operation region varies by different mixers. Therefore, we propose another method based on the direct current (DC) offset coupling to achieve the same goal but in a more stable and reliable way.

3.2.2 **DC Offset Scheme**

The second scheme is based on direct current (DC) offset. The system architecture is shown in Figure 19 [71].

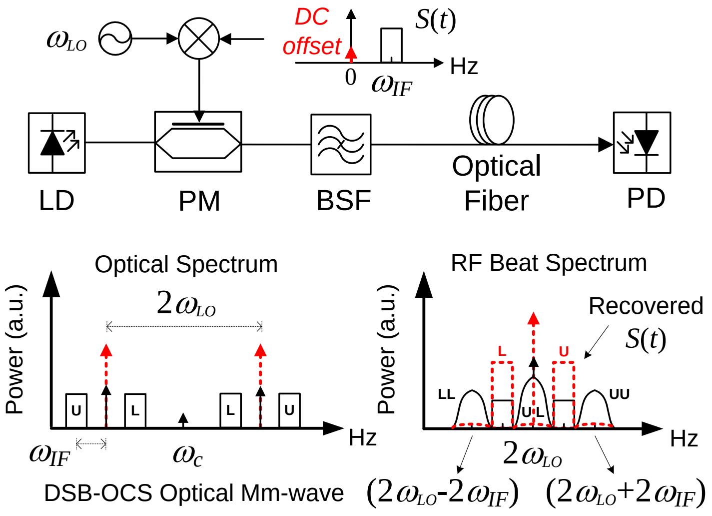

Figure 3.9. Analog IF signal delivery over single-stage DSB-OCS optical mm-waves through DC offset.

Assuming the input signal S(t) is the same as in the previous case, which is an OFDM signal carried on an IF. However, in this scheme, we intentionally add a DC offset (*D*) to the original analog IF signal. Then the resulted signal is mixed with a local oscillator (LO) at ω_{LO} = 30GHz. Considering the LO power feedthrough effect from a practical RF mixer, the upconverted signal can be represented as:

$$E_{mix}(t) = (D - Dr + r)E_{LO}\cos\omega_{LO}t + S(t)(1-r)E_{LO}\cos\omega_{LO}t\,, \qquad (3.16)$$

where *r* is the leakage ratio from the RF port to the LO port of a physical mm-wave mixer, E_{LO} is the field intensity of the LO, and D is the added DC term. After single-stage DSB-OCS mm-wave generation, the signal is transmitted over fiber and direct detection by a PD. The generated beating signal at $2\omega_{LO}$ is given by:

$$E(t) = E_0^{\,2}(E_{LO}')^2\beta^2[(D')^2 + 2D'S(t) + S(t)^2]\cos(2\omega_{LO}t)\,, \qquad (3.17)$$

where $D'=D+r/(1-r)$, $E_{LO}'=E_{LO}/(1-r)$, E_0 is the transmitted electrical field of the CW light, and β is the phase modulation index. The term $2D'S(t)$ contains the desired original signal that has been recovered and enhanced through the DC offset coupling. In the traditional case with no DC offset applied, the inter-band interferences (IBI) term: $S(t)^2$ is dominant resulting from the beating between L and U bands, and the interferences are located at $2\omega_{LO}$ and $2\omega_{LO} \pm 2\omega_{IF}$, as illustrated in Figure 3.9. We notice that the IBI can be suppressed by increasing the applied DC offset. In this case, the central carrier intensity of $E_{mix}(t)$ can be enlarged to the extent that saturates the mm-wave mixer so as to decrease the inter-band interferences and increase the signal to interference ratio.

To demonstrate the proposed DC offset scheme in a practical system, an experiment was conducted and its setup is shown in Figure 3.10. The tested analog IF signal is a 200 Mb/s QPSK-OFDM signal at IF of 100 MHz (1024 subcarriers, 1GHz sample frequency), which is generated by an arbitrary waveform generator (AWG). A weak DC power is added to the QPSK-OFDM signal at the output of AWG. The amplitude of the QPSK-OFDM signal is about 0.1Vpp, and the DC offset is swept between +/- 0.4V. The signal transmission and detection procedures are similar to the previous setup.

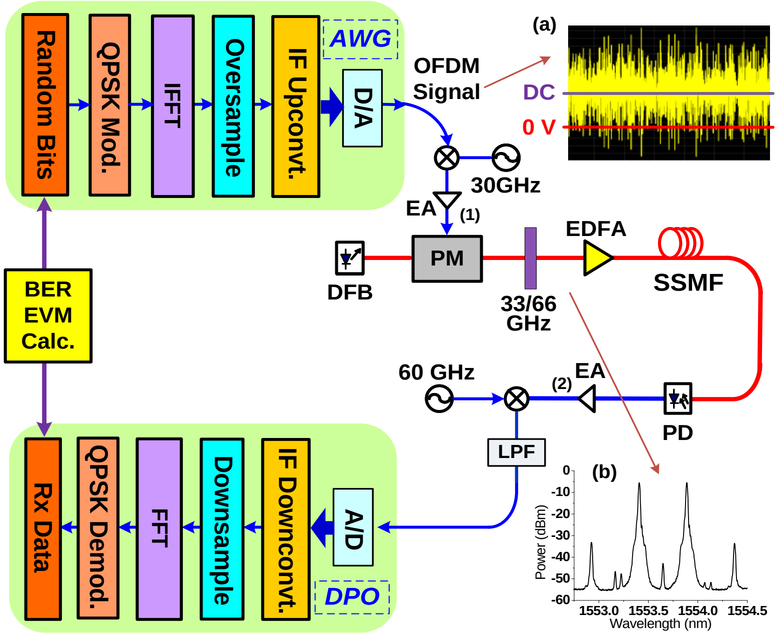

Figure 3.10. Experimental setup of QPSK-OFDM signal transmission over single-stage DSB-OCS mm-waves RoF system through DC offset coupling.

Figure 3.11(a) shows the measured RF power of the electrically upconverted QPSK-OFDM signal and the 30GHz RF carrier at different DC offsets. In general, the 30GHz carrier power is enhanced by increasing the DC offset. The vector signal will be highly suppressed as the carrier power increases to the extent that saturates the double-balanced RF mixer. The insets show the measured RF spectra. Next, we investigated how such power transition between 30GHz carrier and vector signal could be utilized to recover the desired signal after the photodetection. Figure 3.11(b) shows the measured RF power of the desired QPSK-OFDM signal (U) and IBI tone (UU) after photodetection and downconversion. When DC offset = -0.026V, the desired vector signal totally vanished while the IBI tone at 200MHz became maximum as shown in inset (ii). As more DC being applied, the QPSK-OFDM signal was gradually enhanced until the RF mixer started to saturate. Note that the worst case happens when DC offset equals to -0.026V instead of 0V. This is due to the LO power feedthrough effect from a practical RF mixer. As we derived earlier, when $\tilde{D}=D+r/(1-r)$ approaches to zero, it is the worst case with no original information recovered. At this time, the applied DC offset voltage D is a small negative value (i.e. -0.026V).

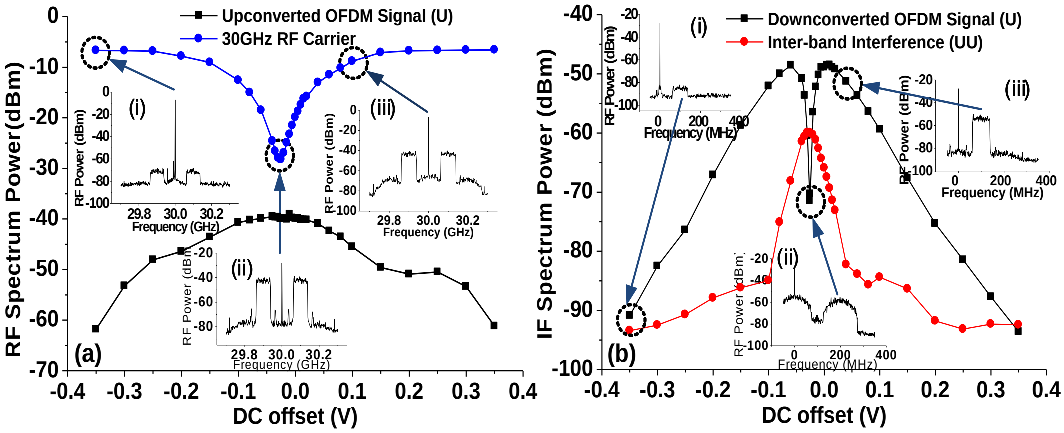

Figure 3.11. Measured RF power of (a) the 30GHz carrier and the upconverted OFDM signal and (b) the downconverted OFDM signal and inter-band interference term versus different DC offset voltages measured at the point (1) and (2) in Figure 3.10, respectively.

The measured signal quality (EVM value) under different system configurations are shown in Figure 3.12. The measured EVM value of the demodulated QPSK-OFDM signal as a function of applied DC offsets under back-to-back transmission case is shown in Figure 3.12(a). The results are consistent with the Figure 3.11(b). The insets show the signal constellations for the worse and the optimized EVM at DC offsets of -0.026V and +/-0.06V, respectively. The dashed line shows the EVM value of 26.5%, which corresponds to the error-free condition in our setup. Therefore, in this case, the min value of the required DC-to-signal amplitude ratio to achieve error-free condition is 0.1.

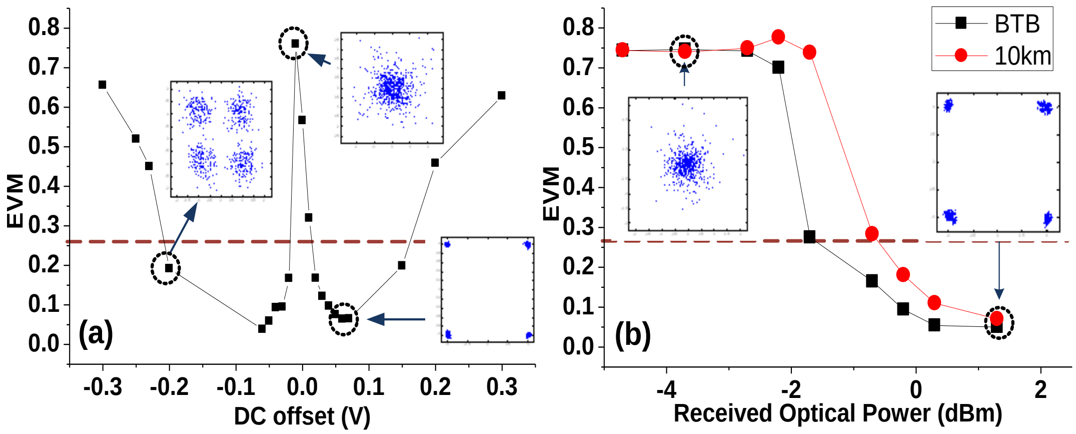

Figure 3.12. (a) EVM vs. DC offset (b) EVM vs. received optical power (for both BtB and 10km fiber transmission cases).

Figure 3.12(b) shows the obtained EVM versus the received optical power when the optimized DC offset voltage of +0.06V was applied for both BTB and 10km fiber transmission cases. Less than 1 dB penalty of the receiver sensitivity at EVM of 20% was observed. In addition, after 10km transmission of SSMF, the EVM value as low as 5.52% can be achieved at a receiver sensitivity of 1.2dBm. The high receiver sensitivity is due to the small effective area of the mm-wave band photodetector and can be enhanced through pre-amplification for longer transmission distance.

Therefore, to summarize the mixer LO power feedthrough scheme and the DC offset scheme, both schemes achieve successful analog IF signal transmission in the single-stage DSB-OCS mm-wave radio-over-fiber systems. Compare these two schemes, the second scheme (DC offset approach) is more flexible and more reliable than the LO power feedthrough scheme.

We notice that the key idea of these two approaches is to enhance the optical carrier power of the optical mm-wave sidebands, and therefore enhance the beating between optical carriers and the carried data to recover the original information. Therefore, the similar idea can be used as a generalized method for vector signal transmission in DSB-OCS mm-wave cloud-RoF systems. More detailed discussion will be given the next section.

3.2.3 Generalization for Vector Signal Transmission in DSB-OCS Mm-Wave RoF Systems

As two novel methods have been introduced in the previous section to enable analog IF signal (e.g. OFDM signal) transmission in the single-stage DSB-OCS mm-wave RoF system, we found the key idea is to enhance the optical carrier power of the optical mm-wave sidebands, thus enhancing the beating between optical carriers and the carried data to recover the original information. Similar concept can be used for baseband vector signal transmission for both single-stage and dual-stage DSB-OCS mm-wave RoF systems, and we separate the discussions for single-stage and dual-stage DSB-OCS mm-wave RoF systems separately.

3.2.3.1 Single-stage DSB-OCS scheme

First of all, recall the single-stage DSB-OCS optical mm-wave generation in Figure 3.2(b) and the issues related to baseband vector signal transmission in the single-stage DSB-OCS mm-wave cloud-RoF systems (Table 3.2).

Based on the same concept of optical-to-signal power ratio enhancement, we propose a modified single-stage DSB-OCS optical mm-wave generation scheme as shown in Figure 3.13.

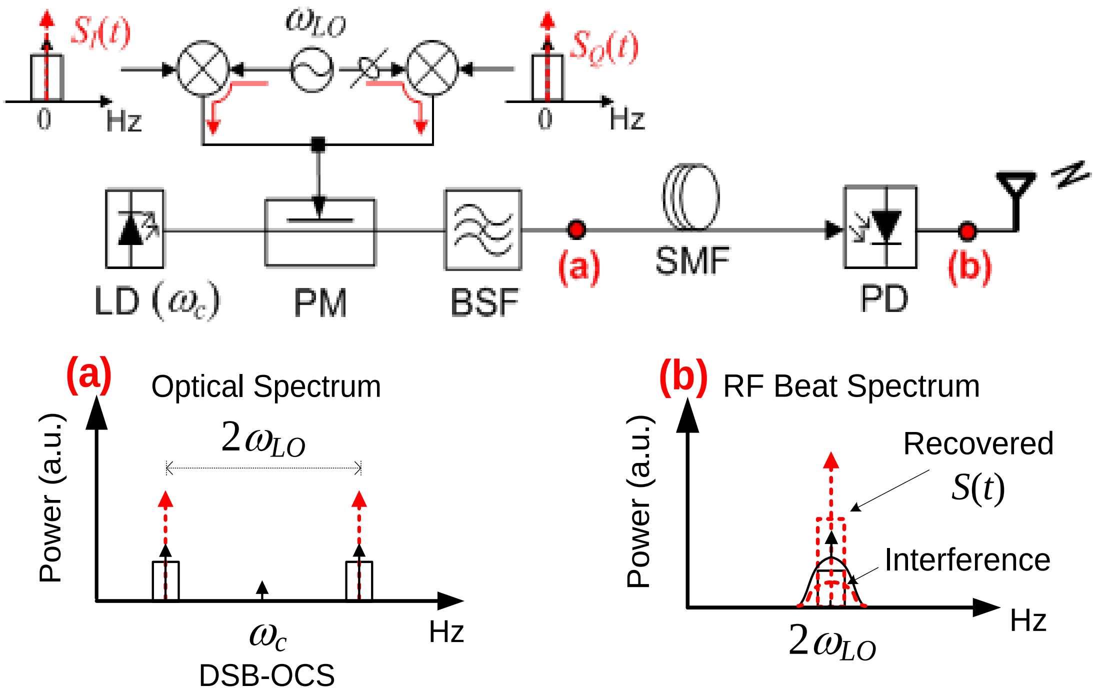

Figure 3.13. Proposed scheme for vector signal transmission in single-stage DSB-OCS mm-wave RoF systems.

Notice that both LO power feedthrough method and DC offset method can be used at the I/Q RF mixer to enhance the RF-carrier-to-signal power ratio. Therefore, at point (a), the optical-carrier-to-signal power ratio is enhanced, thus the original information can be recovered after photodetection at point (b). This scheme relies on the same concept of LO power feedthough and DC offset methods to recover the original signal.

Due to the limitations of Lab components, we conducted simulations in VPItransmissionMaker^{TM} instead of experiments to validate the proposed scheme. The simulation results can be seen in Figure 3.14.

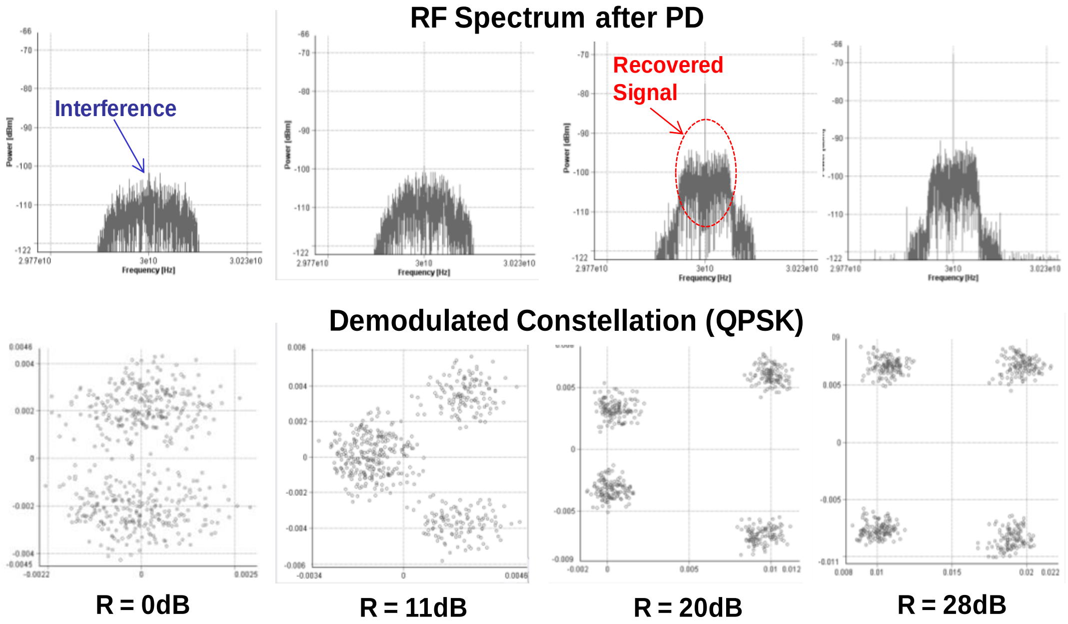

Figure 3.14. Simulation results of vector signal transmission in single-stage DSB-OCS mm-wave RoF systems.

Notice that the parameter R is defined as the RF power ratio of RF carrier to vector signal at the output of I/Q mixer. As we can see from Figure 3.14, when we increase the power ratio R (by either LO power feedthrough or DC offset), the desired signal can be recovered after PD, which can be observed from both RF spectrum and demodulated constellation. Therefore, this demonstrate the feasibility of vector signal transmission in single-stage DSB-OCS mm-wave RoF system based on carrier-to-signal power enhancement.

3.2.3.2 Dual-stage DSB-OCS scheme

Similar concept of carrier-to-signal power enhancement can be used for dual-stage DSB-OCS mm-wave RoF systems. A simple system setup is proposed as shown in Figure 3.15.

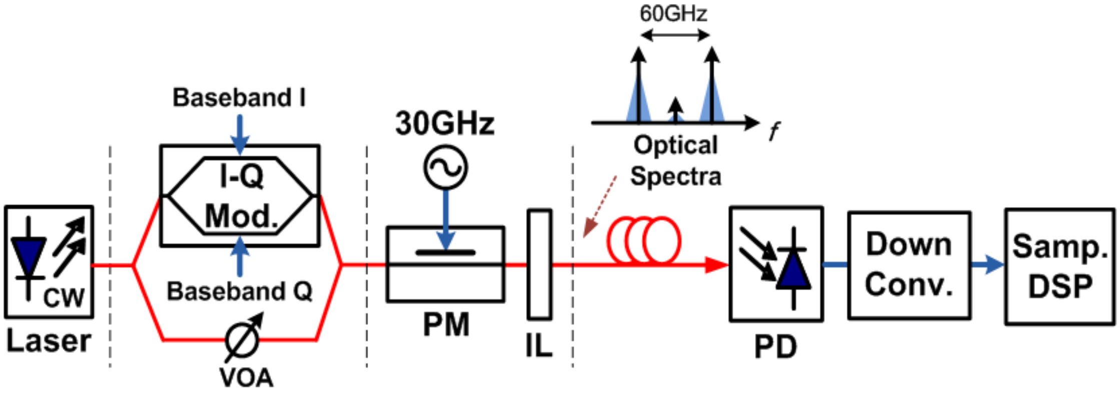

Figure 3.15. Proposed scheme for vector signal transmission in dual-stage DSB-OCS mm-wave RoF systems.

However, due to the limitations of experimental equipments, this proposed system has not been tested experimentally. However, simulations have been conducted and similar results as in Figure 3.14 have been obtained, which validate the proposed scheme for vector signal transmission in dual-stage DSB-OCS mm-wave RoF systems.

3.3 Simplified Duobinary Mm-Wave Receiver Design

As mentioned previously, scalar and vector signals are the two types of digital baseband format signals. Scalar signal has the advantage of simple modulation (single-arm MZM) while the vector signal modulation requires optical I-Q modulator with precise phase matching between I and Q arms. But vector signal provides higher spectral efficiency to further increase the data rate.

Therefore, to balance the tradeoffs between system complexity and the spectral efficiency in a high-speed communication system, a special vector signal modulation format, duobinary (DB), has attracted a lot of research interests.

In general, DB signal is a three-level signal represented as {-1, 0, +1} in the constellation as shown in Figure 3.16. The generation of optical DB signal is achieved by driving a Mach-Zehnder modulator (MZM) with an electrical DB (three-level) input signal biased at the null point of the MZM transfer function [72]. To generate the electrical DB signal from a binary data sequence, both digital and analog encoding can be used. The digital encoding way uses a delay-and-add circuit with a gain controller and a low-pass filter (LPF), while the analog encoding is simpler with only one analog LPF needed. The analog filter shape of Bessel and the bandwidth of 1/4 of the input binary data rate are commonly used. Notice that the binary input signal is usually precoded to prevent the error propagation at the receiver side.

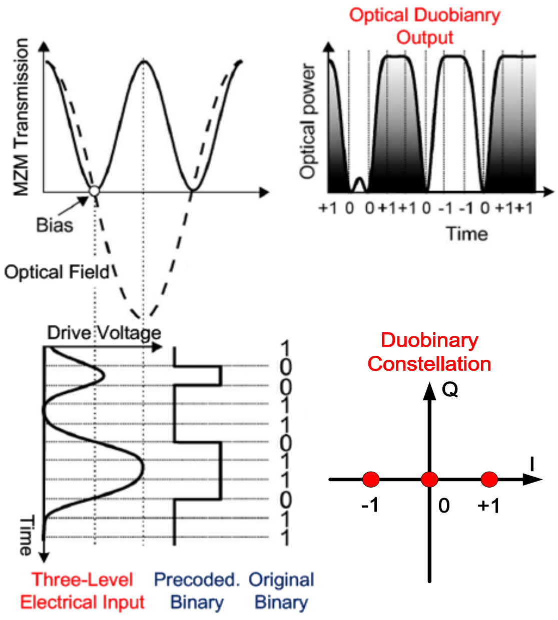

Figure 3.16. Constellation of duobinary (DB) signal and its generation through an optical Mach-Zehnder modulator (MZM).

DB belongs to the baseband vector signal format that cannot be recovered directly after the DSB-OCS optical mm-wave transmission. In the previous work [73], our lab has demonstrated the optical transmission of DSB-OCS optical mm-waves carrying DB data, but mm-wave wireless transmission carrying decoded binary data after photodetection. However, to preserve the three-level DB properties in both the optical and RF domain that maintains the spectral efficiency advantages throughout the signal transmission, we can use the idea introduced in previous sections to enhance the power of optical carriers. However, because of the limitations of the components, we cannot realize the baseband vector signal transmission in the DSB-OCS mm-wave RoF system experimentally. Therefore, we consider a different optical mm-wave generation scheme, namely, the single-sideband (SSB) optical mm-wave scheme.

For the SSB optical mm-wave generation scheme, only one of the two optical mm-wave sidebands is modulated with data, which gives the name of the single sideband (SSB). After the photodetection, the beating between the two optical sidebands will generate a 60GHz RF signal carrying original data information without the phase distortion. Compared to the DSB-OCS optical mm-wave, the generation of SSB optical mm-wave is usually more complicated, and the efficiency of the O/E conversion is also lower resulting in lower receiver sensitivity.

To achieve SSB optical mm-wave generation, two methods are commonly used: 1). two independent lasers; 2) coherent SSB generation. The first scheme uses two independent lasers as the two optical carriers, and modulates only one of them with data. For the second scheme (the coherent SSB generation), there are several different approaches. But the basic idea is to generate two ***coherent*** optical carriers, and modulate only one carrier with the data. Comparing these two SSB optical mm-wave generation methods, the coherent approach has the advantage of frequency and phase stability over the independent lasers approach, but it is more complicated with more system fine tuning and control.

Therefore, by combining the SSB optical mm-wave generation with the DB signal modulation, the DB signal transmission in the SSB mm-wave RoF system is shown in Figure 3.17 [75].

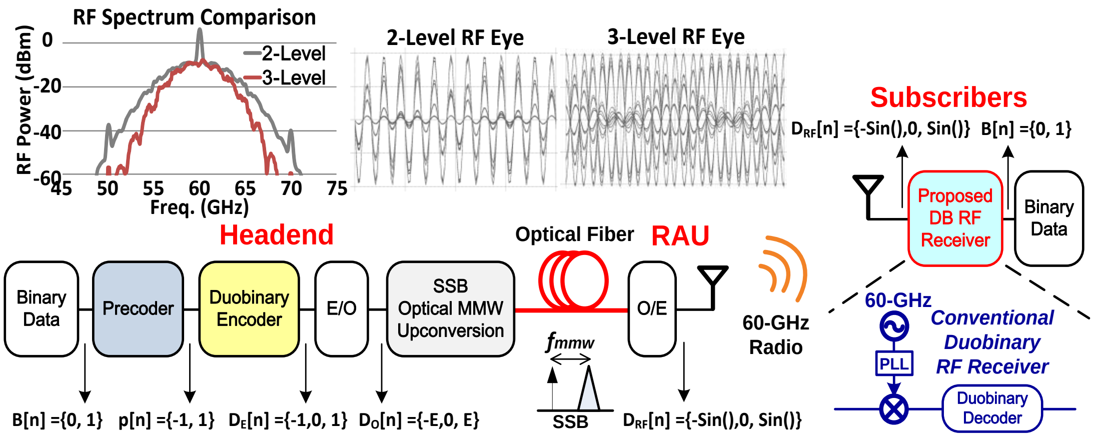

Figure 3.17. DB signal transmission in the SSB mm-wave RoF system with proposed duobinary RF receiver.

In the headend office, the original binary data B[n] is initially precoded (or differential encoded) to avoid complicated decoder at the receiver side and also to avoid error propagation effect [73]. The precoded binary data p[n] = {1, -1} are further encoded to generate three-level electrical DB sequence $D_E[n] = \{-1, 0, 1\}$. The following electrical to optical (E/O) conversion module is responsible for modulating the electrical DB sequence onto an optical carrier by driving an optical MZM biased at null point. Therefore, the output optical DB signal Do[n] = {-E, 0, E} exhibits two levels in terms of optical power while preserving three-level properties in optical phase. At the optical mm-wave upconversion stage, SSB optical mm-wave generation method is used to maintain the three-level phase information. The beating of SSB optical MMW carriers at the photodetector (PD) in remote antenna unit (RAU) generates a three-level RF DB signal $D_{RF}[n] = \{-\mathrm{Sin(RF)}, 0, \mathrm{Sin(RF)}\}$. The comparison of two-level and three-level RF spectra and the corresponding RF eye diagrams are shown in the insets of Figure 3.17. We can see the improved spectral efficiency by maintaining the three-level feature in the RF domain.

After mm-wave wireless transmission, to detect and demodulate the DB data (vector signal) carried on the 60GHz RF, conventionally a 60GHz local oscillator, a phase-locked loop (PLL), a mixer and a DB decoder are needed at the RF receiver [74]. However, to simplify the system design, a novel RF receiver scheme based on the self-mixing effect is proposed and demonstrated experimentally. The difference between a conventional DB RF receiver with the proposed self-mixing DB RF receiver is shown in Figure 3.18.

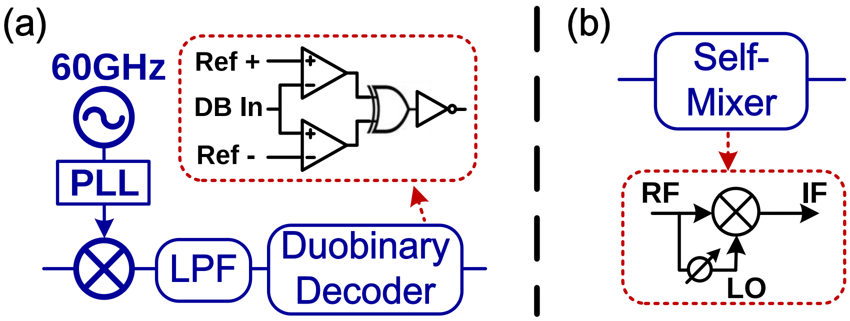

Figure 3.18. Comparisons between (a) conventional DB RF receiver and (b) proposed DB RF receiver based on self-mixing effect.

The principle of a self-mixer is to multiply the incoming RF signal with itself and then low-pass it to obtain the downconverted baseband signal. Since the signal is multiplied with itself, the in-phase mixing condition is easily satisfied, which enables stable mixing operation, and no PLL and LO is needed. For the DB decoding part, different from the conventional DB decoder, Figure 3.18(a) inset, which consists of two comparators with different slicing levels, by which ±1 are decoded as 1, and 0 is decoded as 0 [74]; we find out that the function of a self-mixer is equivalent to decoding ±Sin(RF) into 1, and 0 into 0. Therefore, by feeding a three-level RF DB signal $D_{RF}[n]$ = {-Sin(RF), 0, Sin(RF)} into a self-mixer, the output signal is both downconverted and decoded automatically, which gives the desired binary sequence B[n] = {0, 1}. Therefore, simple and stable RF downconversion and DB decoding are achieved simultaneously based on this self-mixing effect [76].

To demonstrate the proposed DB RF receiver in the context of DB signal transmission in a SSB mm-wave RoF system, an experiment was conducted as shown in Figure 3.19.

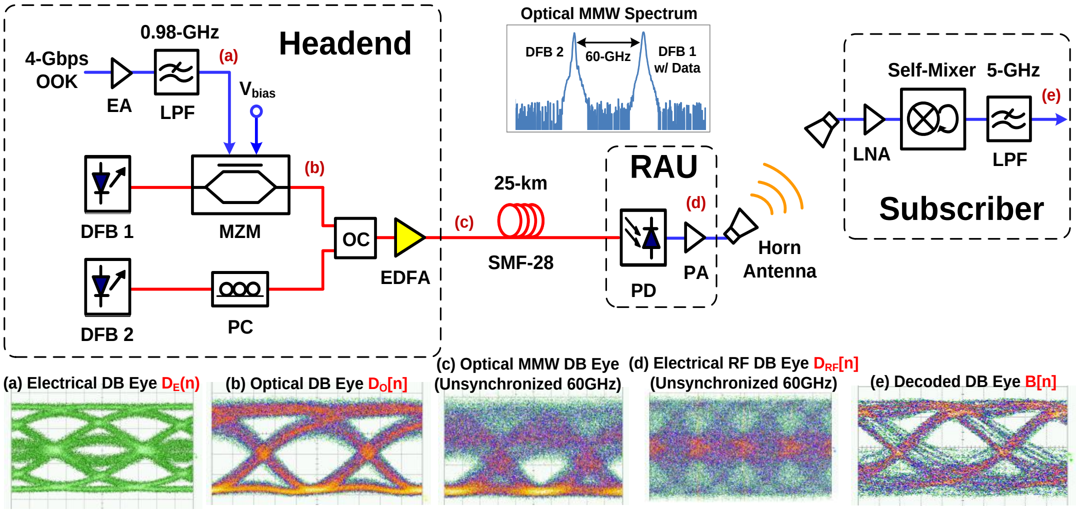

(a) Electrical DB Eye $D_E(n)$

(b) Optical DB Eye $D_O[n]$

(c) Optical MMW DB Eye (Unsynchronized 60GHz)

(d) Electrical RF DB Eye $D_{RF}[n]$ (Unsynchronized 60GHz)

(e) Decoded DB Eye $B[n]$

Figure 3.19. Experimental setup of DB signal transmission in SSB mm-wave RoF system with proposed self-mixing DB RF receiver.

In the headend office, a 4-Gbps pseudo-random binary sequence (PRBS) was considered as a precoded binary sequence, and was converted into a three-level electrical DB signal by passing through a Bessel electrical low-pass filter (LPF) with 3dB-bandwidth of 0.98GHz [73][77]. To generate the optical DB signal, a DFB laser

(DFB1) at 1554.18 nm was externally modulated by a $LiNbO_3$ optical MZM, which was driven by the three-level electrical DB signal with a bias voltage (V_{bias}) of 3.2V at its transmission null. The resulting optical DB eye is shown in the inset (b) of Figure 3.19 that exhibits two levels in terms of optical power, but actually three levels in optical phase. The other un-modulated DFB laser (DFB2) at the wavelength of 1553.7 nm was coupled with DFB1 through an optical coupler (OC) to achieve SSB optical mm-wave upconversion. The optical mm-wave signals were transmitted through 25-km SMF-28 to the RAU, and were directly detected by a 60GHz photodiode (PD) to generate the 60GHz DB RF signal. The eye diagrams of the optical mm-wave signal and the three-level DB RF signal are shown in inset (c) and (d) of Figure 3.19, respectively. Since the 60GHz RF is generated from the beating between two phase-unlocked lasers, which cannot be synchronized with the scope, we are not able to see the 60GHz clock on both eye diagrams as shown in the case of simulation (inset of Figure 3.17). After wireless transmission, the received three-level DB RF signal was then amplified and fed into a self-mixer. After the RF downconversion and DB decoding function were done within the self-mixer, the output binary sequence was sent into bit error rate (BER) tester for BER calculation.

Figure 3.20 shows the BER performance of demodulated DB signals at different received optical power as a function of wireless propagation distance with and without 25-km optical fiber transmission. As shown in Figure 3.20(a), error-free transmission (BER lower than $1x10^{-9}$) over 25-km SMF and 4-ft in-building wireless distance was achieved at received optical power of 1dBm. The high received optical power value is due to no optical pre-amplifier being used. There is about 1.5dB optical power penalty after 25-km SMF transmission compared with the back-to-back (BTB) fiber transmission case. This is mainly resulting from the degenerated phase noise from the two independent lasers after fiber transmission. As we can see from Figure 3.20(b), for the BTB case, with 3-dB increase in the received optical power (from -2dBm to 1dBm), the wireless distance can be extended by 3-ft while maintaining the same target BER. In addition, the insets of (a) show the measured eye diagrams of downconverted DB signal after 4-ft wireless distance at the received optical power of 1dBm with and without 25-km fiber transmission.

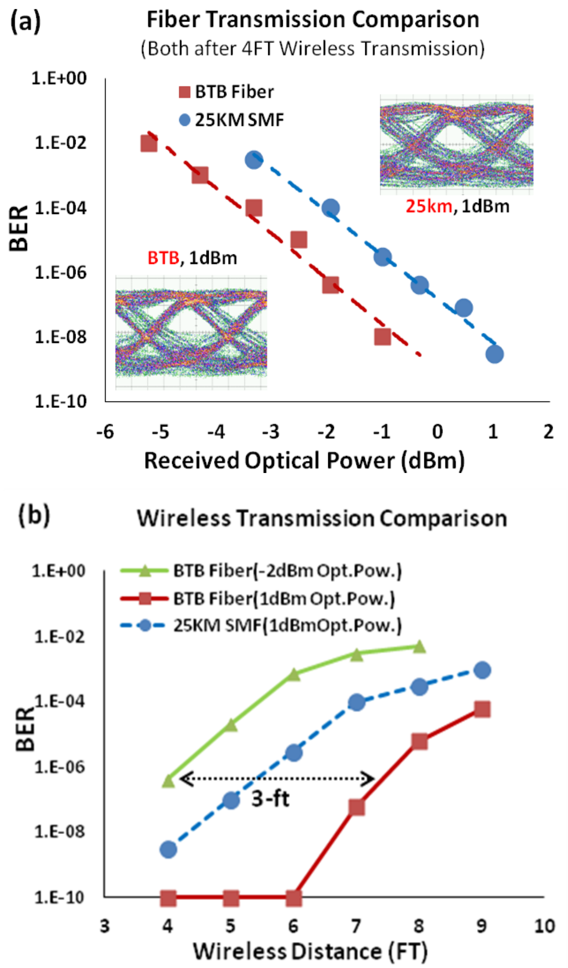

Figure 3.20. BER performance of the demodulated DB signals at different received optical power (a) and wireless propagation distance (b) for both BTB and 25-km fiber transmission cases.

In conclusion, we have proposed and demonstrated a simplifed DB RF receiver design for mm-wave cloud-RoF systems. By utilizing the self-mixing effect, the RF downconversion and DB decoding are achieved simultaneously that greatly simplifies the conventional DB receiver. We believe this proposed DB receiver scheme can provide simplified and robust DB signal demodulation for high-speed and high spectral efficient mm-wave radio-over-fiber systems.

CHAPTER 4: JOINT DETECTION AND DIGITAL SIGNAL PROCESSING FOR COHERENT OPTICAL COMMUNICATION SYSTEMS

4.1 Introduction to Superchannel Coherent Optical Communications Systems

To meet the bandwidth requirements in future optical core networks, the design of transport systems capable of supporting 1Tb/s and greater channel rates based on “superchannel” architectures has been proposed and attracted lots of research interests. The basic concept of the superchannel architecture is to group a number of tightly spaced subcarriers to form a high spectral efficient multi-carrier signal. Therefore, channel capacity can be increased while minimizing the need for high-level modulation formats and high baud rates, which may allow existing format, baud rate and components to be exploited.

As mentioned in Section 1.2.2, Nyquist-WDM [52][53] and coherent optical-OFDM (CO-OFDM) [54][59] are the two approaches to obtain the ultra-high spectral efficiency in superchannel systems. Theoretically, both approaches can achieve baud-rate channel spacing without inducing inter-channel interference (ICI) or inter-symbol interference (ISI). However, in practical systems, neither of the two schemes is perfectly ICI or ISI free.

In ideal Nyquist-WDM superchannel systems, optical subcarriers with rectangular spectra are tightly packed at a channel spacing equals to the baud rate, which achieves Nyquist bandwidth limit. However, in practical Nyquist-WDM systems, precise control on channel spectra is required to avoid strong ICI.

Conventional methods to mitigate ICI effects in Nyquist-WDM systems include pre-shaping the signal spectrum using optical [62] or digital [57] filters to approach a near-rectangular spectrum. Alternatively, strong optical filters can be applied on each subchannel (thus eliminate ICI), followed by DSP to cancel the induced inter-symbol interference (ISI) [53]. The digital pre-filtering (digital pulse shaping) approach by using high-speed DACs is able to achieve more accurate spectral shaping required of true Nyquist-WDM systems. However, Nyquist-like systems (Δf slightly larger than B) may also provide good solutions allowing more cost-effective and power-efficient optical filtering. Transmitter-side approaches are less flexible and adaptable to the overall channel variation, and slight spectral imperfections result in strong ICI at tight channel spacing. A Rx-side solution reduces the filter requirement imposed on the Tx and more readily enables adaptation to changing channel conditions. Therefore, a “super receiver” architecture is proposed to jointly detect and demodulate multiple subchannels at the Rx side and mitigate the penalties associated with the limitations of creating ideal Nyquist-WDM spectra.

4.2 Principle and Design of Joint Detection and Joint DSP

A superchannel system with proposed “super-receiver” architecture (joint detection plus joint DSP) is shown in Figure 4.1 [82].

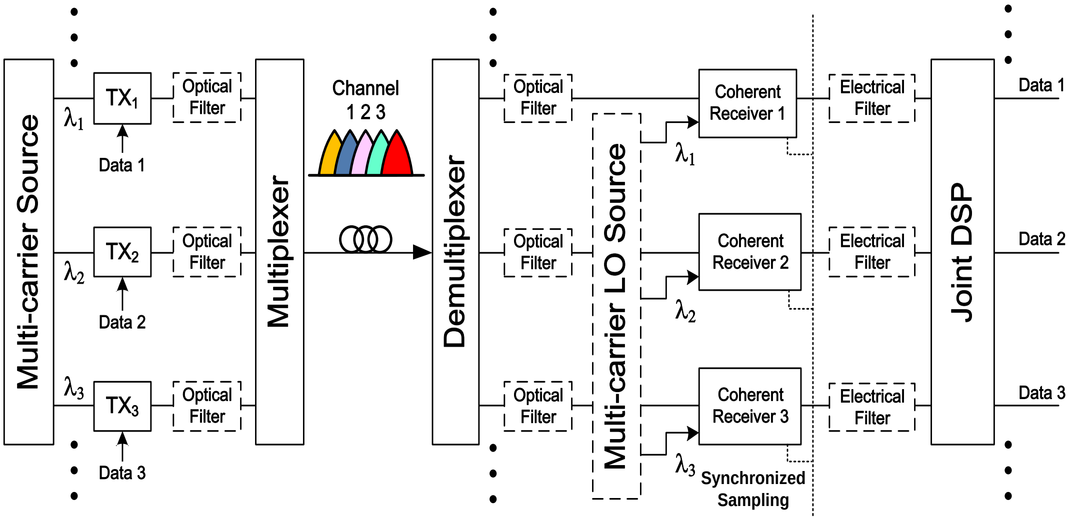

Figure 4.1. **"Super-receiver" architecture for superchannel coherent systems. Optical filters depicted before multiplexer and after demultiplexer represent all optical filters of Tx and Rx respectively.**

Our "super receiver" retains the optical functions of a conventional superchannel receiver, but performs the DSP jointly on multiple subchannels. At the transmitter side, multiple sub-carriers may be generated by independent laser sources [52] or by phase-locked methods [78]. These tightly spaced optical carriers are then independently modulated and optically multiplexed. Strong optical filtering is usually applied to each subchannel before multiplexing to shape the spectrum and minimize ICI. We examine the efficacy of our super-receiver architecture by considering two cases: 1) without Tx optical filtering for individual subchannel and 2) with conventional Tx optical shaping filters. After the optical fiber transmission and optical demultiplexing, each subchannel is sent into its corresponding coherent receiver for O/E conversion, digital sampling and detection. As with the Tx, optical filtering associated with optical demultiplexer is optional. With no individual Rx optical filtering, the function of optical demultiplexer is a simple optical splitter or a wideband optical filter. The carrier separation is done by mixing with an appropriate local oscillator (LO), and passing through subsequent electrical filters. The LOs for coherent receivers are generated in the same way as at the transmitters.

To capture the synchronized information across the subchannels for the subsequent joint signal processing, the optical and electrical path for each subchannel after demultiplexing needs to be the same length, and digital sampling must be synchronized across all subchannels. However, this requirement can be relaxed since it is relatively straight forward to include appropriate time domain memory in the joint DSP functions, which will be discussed later.

Information is available from multiple subchannels in the joint DSP block, thus enabling advanced joint signal processing to cancel crosstalk between the subchannels. Notice that, not only linear ICI (induced by linear spectral overlapping) can be cancelled based on this “super receiver” architecture, in principle, nonlinear ICI (e.g. cross-phase modulation, four-wave mixing, etc.) can also be potentially cancelled by having the information from all the subchannels. In addition, for a carrier-phase-locked superchannel system, since multiple carrier phase information is available, it is possible to compensate carrier phase jointly to achieve better carrier-phase estimation.

Therefore, joint DSP is the key block that realizes all the benefits of the “super receiver” architecture. The detailed discussion on joint DSP will be given in the following sections.

4.2.1 Conventional DSP Procedure and Joint DSP

First of all, a block diagram of conventional DSP procedure for single-channel dual-polarization (DP) – QPSK coherent detection and demodulation is shown in Figure 4.2 as a reference.

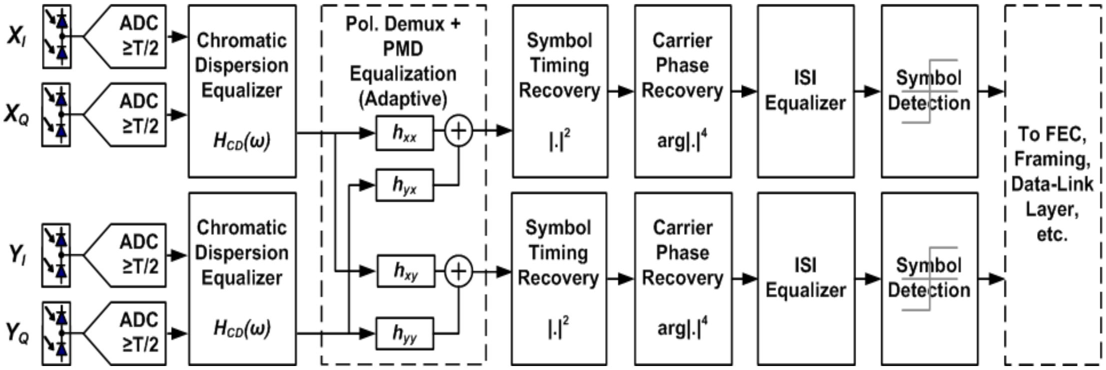

Figure 4.2. Block diagram of conventional single-channel DP-QPSK coherent demodulator.

At the output of a coherent receiver, X_I, X_Q, Y_I, Y_Q represent the detected X and Y polarization with in-phase (I) and quadrature phase (Q) information. After high-speed ADCs, the sampled information follows the conventional DSP processing in the following order: chromatic-dispersion compensation, polarization demultiplexing, timing recovery and carrier-phase estimation. The detailed principle and discussion on each step of the DSP can be found in [79].

Based on the conventional single-channel-based DSP, an example of three-subchannel joint DSP is shown in Figure 4.3. ICI equalization processing for the center subchannel (Ch.2) is illustrated, and the joint carrier phase recovery is optional for carrier-phase-locked superchannel systems.

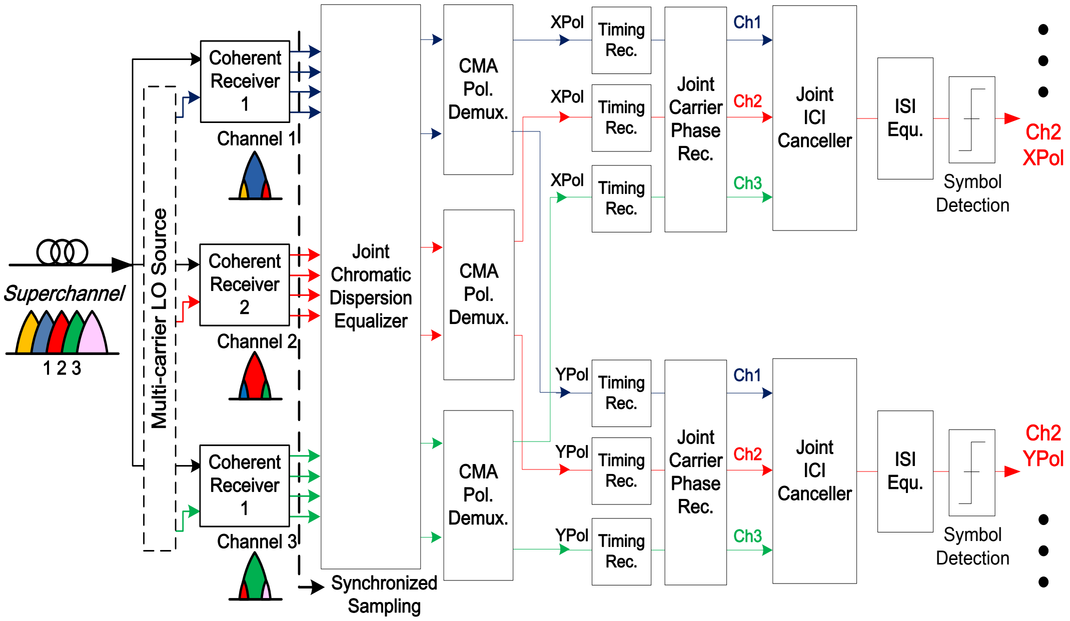

Figure 4.3. Joint-DSP procedure for 3-subchannel Nyquist-WDM superchannel systems.

After the superchannel signal is sampled (with synchronized ADCs), each subchannel follows conventional DSP processing in the following order: joint chromatic-dispersion (CD) compensation, polarization demultiplexing, timing recovery and carrier phase recovery. Notice that except the CD compensation is done jointly, the polarization demultiplexing, timing and carrier phase recovery follows conventional processing for each subchannel independently. Joint carrier-phase recovery is only optional for carrier-phase-locked systems. After timing and carrier-phase recovery, an adaptive ICI equalizer is applied across the three subchannels for both X and Y polarizations separately based on an adaptive least-mean-squares (LMS) algorithm. The joint ICI cancellation can be done for the two polarizations separately after polarization demux, as long as the relative polarization states of the three subchannels remain fixed after demultiplexing. Specifically, the ICI can be considered to occur at the Rx when the subchannels are separated either optically or electrically. Thus as long as the “X” polarization of one subchannel has the same polarization as “X” in its neighbor channels then each polarization can be processed for ICI cancellation separately. We emphasize that the relative polarization state among subchannels must be maintained only over a very limited distance; from the optical demux (or passive split) to the photodiodes of the coherent receivers. In practice, this can be readily accomplished by integrating multiple coherent receivers to detect a superchannel group. In addition, notice that the requirement of polarization tracking can be eliminated by joint processing both X and Y polarizations of all the neighboring subchannels, however, this doubles the complexity of the joint processing.

After joint-ICI cancellation, an ISI equalizer is applied to compensate any residual ISI in the time domain, and the output signal can be used for final decision or sent to forward error correction (FEC).

In the following sections, we will first discuss the joint ICI cancellation algorithm, and then explain why joint CD compensation is needed instead of the conventional independent CD compensation. After that, the joint carrier phase recovery algorithm is introduced.

4.2.2 Joint Linear ICI Cancellation

A block diagram of joint-ICI cancellation is shown in Figure 4.4(a). For each polarization, side subchannels (Ch.1 and Ch.3) are first shifted in the frequency domain by the amount of subchannel spacing to retrieve the spectral overlapping condition experienced during the coherent detection (as illustrated in Figure 4.4(b)). In simulation, we determined that the precision of the frequency shift needs to be better than ~1MHz. This is more stringent than the required precision of the carrier-LO offset estimation, but it is reasonable since carrier-LO offsets result in a simple constellation rotation whereas inter-channel frequency offset errors result in an improper coherent addition to the impaired channel. This frequency shift requirement is most readily accomplished using phase-locked sources and LO's, however it may be feasible to find and track the relative frequency shift between the neighboring channels through joint DSP.

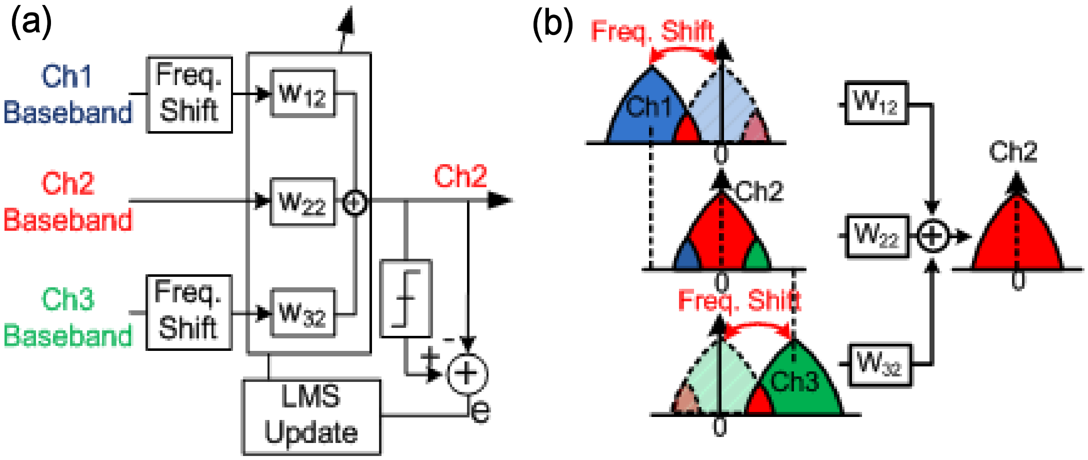

Figure 4.4. (a) Block diagram of joint linear ICI cancellation; (b) Illustration of subchannel frequency shift for subsequent ICI cancellation.

Then the signals from three subchannels are fed into an ICI filter (equalizer), where the filter coefficients (W_{12}, W_{22}, W_{32}) are jointly and adaptively updated based on the LMS algorithm. Each filter coefficient Wij represents the weighted crosstalk from subchannel i to subchannel j. As mentioned previously, each Wij is comprised of a number of time-domain taps to allow for the compensation of any timing skew between the subchannels. Intra-channel ISI can also be partially compensated by these taps. The number of taps depends on the timing offset between the subchannels, it is found that 10 ~ 20 taps are usually sufficient, which corresponds to ~5cm of path mismatch. Note that the same procedure is applied to all subchannels of a superchannel signal with the edge subchannels experience only one-side crosstalk since we presume a small guard band between superchannels.

Since the LMS algorithm is used, the joint ICI algorithm can be applied to any type of modulation format (e.g. DP-16QAM) assuming other parts of the DSP algorithm are compliant. Our initial tests with 16QAM yield similar improvements as experienced with QPSK. This joint ICI cancellation algorithm is capable to cancel the linear crosstalk, and its effectiveness in the nonlinear transmission regime has been tested with simulation results to be shown later. However, to cancel nonlinear crosstalk, nonlinear ICI cancellation model is required, and this is left as future work.

4.2.3 **Joint Chromatic-Dispersion Compensation**

The principle of joint CD compensation which is central to successful ICI cancellation is illustrated in Figure 4.5 [80].

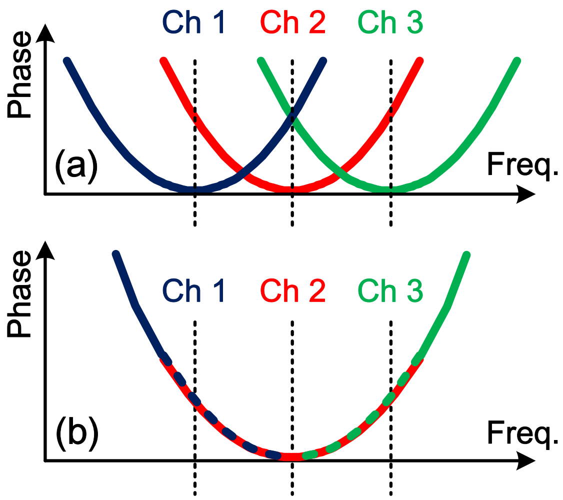

Figure 4.5. Quadratic phase of chromatic dispersion effects for independent CD compensation (a) and joint CD compensation (b).

Since the baseband frequency-domain CD transfer function:

$$G(z,\omega) = \exp(j\frac{Dz\lambda^2}{4\pi c}\omega^2) \tag{4.1}$$

is parabolic in the frequency domain centered at the corresponding reference frequency. Therefore, the goal of CD compensation is to invert the phase response by using digital filtering, performed in either the frequency or time domain. For conventional independent CD compensation (Figure 4.5 (a)), each sub-channel inverts its own phase response with respect to its own LO reference frequency. However, from the center channel point of view, the crosstalk from adjacent sub-channels experiences extended CD parabolic phase response as shown in Figure 4.5(b). Therefore, in order to cancel the crosstalk in the subsequent ICI canceller using the adjacent sub-channels signal, the CD compensation of the sub-channels needs to be re-aligned to the channels of interest. Specifically, for the channel of interest, conventional CD compensation is used directly with no change. For the side-channels, the reference frequencies of CD phase response are shifted corresponding to the sub-channel spacing to match reference frequency of the center channel.

4.2.4 Joint Carrier Phase Recovery

The joint carrier-phase estimation exploits the multiple versions of carrier-phase information available in carrier phase-locked superchannel systems. The initial DSP follows the previous joint ICI cancellation procedure up to carrier-phase recovery. After timing recovery, a joint carrier-phase recovery block is implemented based on a Viterbi-Viterbi (V-V) carrier-phase estimation algorithm. Again, we demonstrate the performance using a three-subchannel example, as shown in Figure 4.6 [83].

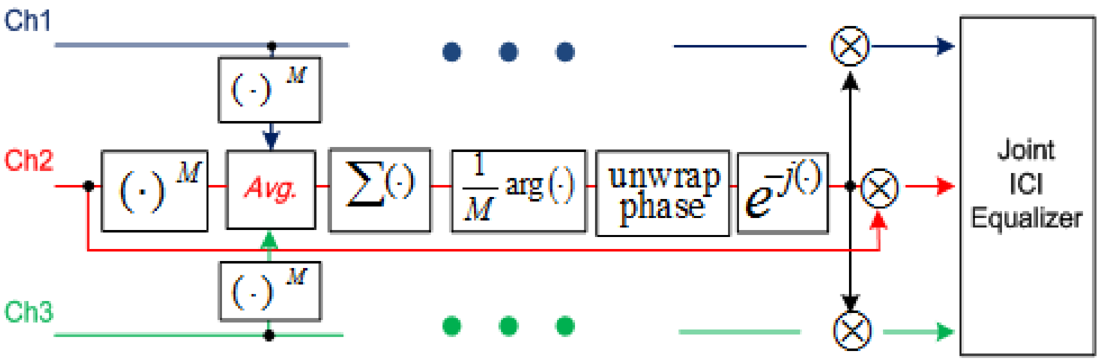

Figure 4.6. Joint carrier phase recovery based on Viterbi-Viterbi algorithm.

The incoming complex baseband signals from each subchannel (both X-pol and Y-pol) are first raised to the 4th power to extract the phase information by removing the data dependencies [81]. Then, the three subchannel streams are averaged. For lasers with relatively narrow linewidth, the carrier-phase noise can be considered as a slow variation with time, and remains constant over several symbol periods. Since all the subchannels experience the same carrier-phase noise variation in a carrier phase-locked system, we average the estimated phase noise both in the time domain and across the subchannels to reduce the impact of ASE and other random noise sources. Also, inter-channel phase-noise impairments can be reduced by the cross-channel averaging process. After that, the argument of the output is divided by 4 and the phase is unwrapped. Finally, the jointly estimated phase error is applied to correct the carrier phase for all the subchannels. Thus the primary difference with the traditional Viterbi-Viterbi carrier-phase recovery algorithm is that one more average stage is added across the subchannels to have a better estimation of the carrier phase.

We found that the two outside subchannels always suffer less crosstalk than the inner subchannels, thus their carrier-phase estimates are more accurate. Therefore, by using the estimated phase information only from the two outside sub-channels, a more precise phase estimation can be obtained and applied to all the subchannels. We emphasize that the relative phase-locked condition must be maintained among the subchannels for joint carrier phase recovery. In practical systems, an integrated superchannel Tx design (with coherent comb generation, optical demux/mux, and data modulation) is preferred to minimize the phase mismatch generated at the Tx. After fiber transmission, we found in simulation that the phase-locked condition is well maintained once the deterministic chromatic dispersion is compensated.

After the joint carrier-phase recovery stage, the three-subchannel signals for both X and Y polarizations can be sent to the joint ICI equalizer. The joint carrier-phase recovery algorithm is compatible with any subsequent DSP including the joint ICI cancellation algorithm.

4.3 Experimental and Simulation Tests

To demonstrate the "super receiver" architecture and the proposed joint DSP algorithms, we performed a proof-of-concept experiment and a separate more complete simulation analysis. We considered two possible superchannel scenarios with different system configurations, as shown in Figure 4.7(a).

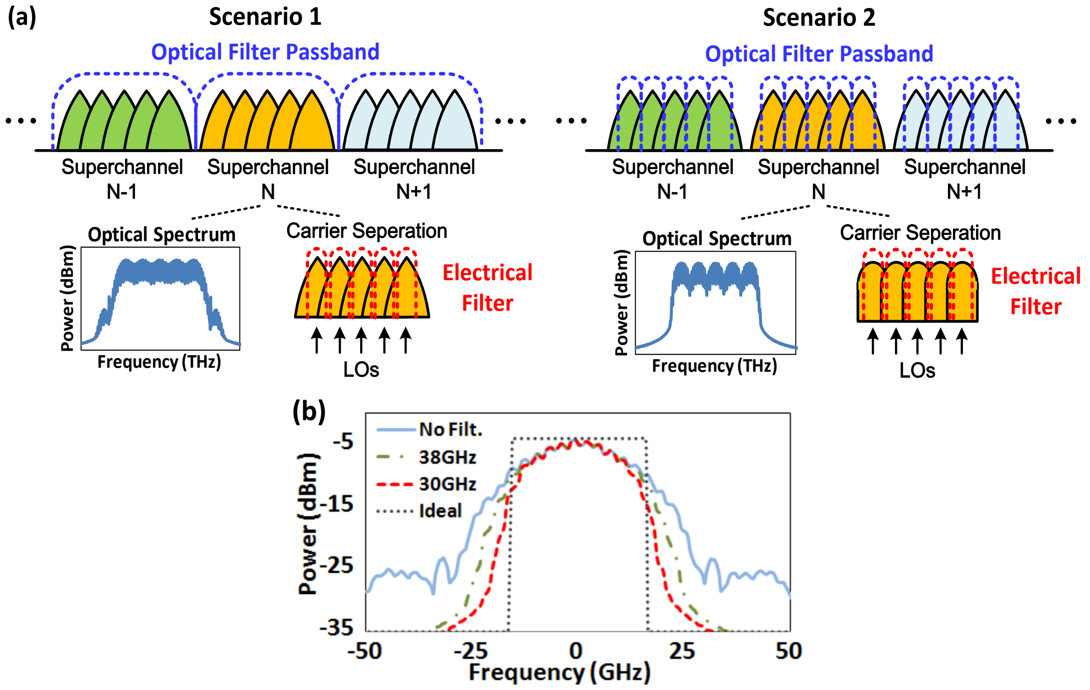

Figure 4.7. (a) Superchannel optical filter scenarios examined. Scenario 1 is the case where no optical filtering is used either at the Tx or Rx for each individual subchannel. Scenario 2 depicts a more typical case where each subchannel is optically pre-filtered at Tx. Subcarrier separation is done in the electrical domain at the receiver for both scenarios. (b) Examples of Tx optical

spectral shapes of 32GBaud QPSK signal under different optical Tx filter bandwidths (ideal 32GBaud Nyquist spectrum, no Tx filter, 38GHz, and 30GHz filter cases).

For scenario 1, optical filtering of each subchannel is omitted throughout the link, and the Tx spectra are limited only by the bandwidth of the generating drivers and modulators. The sub-carrier separation is done strictly by the electrical filters at the receivers. Therefore, the ISI penalty from narrow optical filtering is avoided. However, due to the highly overlapped subchannel spectra, severe ICI exists. We examine this extreme case as a test of the robustness of the joint ICI cancellation algorithm.

Scenario 2 represents a more practical Nyquist-WDM superchannel setup, where each subchannel is optically filtered before multiplexing to minimize ICI. Electrical filters are used to separate the subchannels at the receiver side. The trade-offs between ICI and ISI effects require an optimal design of the optical filter shape and bandwidth, which is analyzed in our simulations. As mentioned, electrical pre-filtering may achieve more accurate spectral shaping, however, we consider the optical pre-filtering method as an example of the general Tx-side approaches, and study the ICI impairments induced by imperfect spectral shaping under different Tx filter configurations and investigate the performance benefits of the "super receiver" approach. Examples of Tx optical spectral shapes of 32GBaud QPSK signal under different optical filter bandwidths are shown in Figure 4.7(b).

The joint ICI cancellation algorithm is validated under both system scenarios. Under scenario 1, we performed a proof-of-concept experiment with a two-subchannel setup. For scenario 2, a more complete simulation analysis under a three-subchannel configuration was conducted, and the optimal optical filter bandwidth was examined under different channel-spacing conditions. We also demonstrated the performance of the joint carrier-phase recovery algorithm, using simulations for both three-subchannel and five-subchannel configurations in a carrier phase-locked system of scenario 2.

4.3.1 2-Subchannel Proof-of-Concept Experimental Tests

We experimentally investigated scenario 1 using a two-subchannel system without Tx optical filtering, as depicted in Figure 4.8.

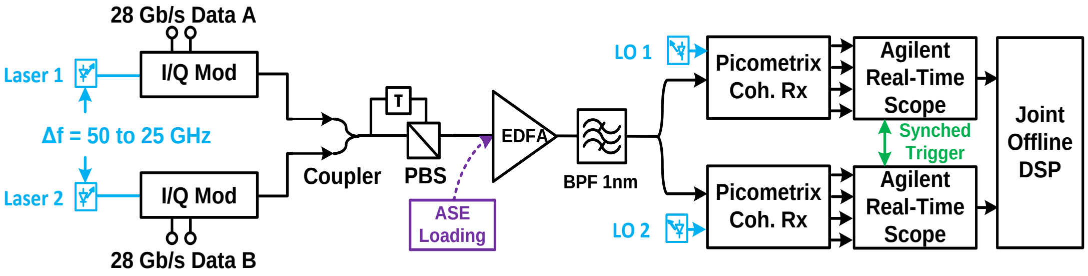

Figure 4.8. Two-subchannel, DP-QPSK, proof-of-concept BTB experimental setup based on the "super receiver" architecture. Neither channel is optically filtered (scenario 1). Both channels use separate but synchronously sampled coherent receivers.

Two independent lasers each carrying 28Gbaud (112Gb/s) DP-QPSK data were muxed together without optical filters. After back-to-back (BTB) transmission, the two-subchannel signals were split into two paths, and were received by two coherent receivers with two synchronized 40GSamples/s Agilent sampling oscilloscopes with a 3dB analog bandwidth (BW) of 16GHz and a 6dB BW of 18GHz. Channel spacing was varied from 50GHz to 25GHz.

The BER (bit-error ratio) vs. OSNR (optical signal-to-noise ratio) was measured for each channel spacing and the required OSNR to achieve a BER of 10-3 was determined, Fig. 8. The performance of both the conventional independent demodulation method and the LMS ICI cancellation algorithm is compared. The corresponding simulation results are shown for comparison. The conventional algorithm includes a long-memory ISI equalizer (15 taps) to mitigate the filtering induced ISI effects and is a typical algorithm used for Nyquist-WDM superchannel signal demodulation without joint DSP [78].

The required OSNR at large channel spacing, >2 ×BWelec (twice the electrical BW of the sampling scope), is ~15.5dB for both experiment and simulation indicating good performance for 28Gbaud DP-QPSK as well as good simulation accuracy in the low ICI regime. Decreasing the channel spacing to less than the electrical bandwidth results in increased ICI and increased required OSNR, as shown in Figure 4.9. However, with the joint ICI equalizer applied, much of the ICI penalty is recovered. For this two-subchannel case, the 30GHz channel spacing has a 2dB penalty using the conventional independent process yet the joint ICI approach reduces this penalty to 1dB, demonstrating the capabilities of the joint ICI cancellation approach. We note that the experimental penalties are larger than the simulation penalties likely resulting from slightly different spectral shape and the high sensitivity to ICI. Note in this particular system setup, since no optical filter is applied at multiplexing, there is significant ICI and the conventional algorithm experiences large ICI penalties.

From the results obtained from the proof-of-concept experimental test, we demonstrate the efficacy of the proposed joint ICI cancellation algorithm for the back-to-back transmission case. More complete simulation studies with more general system configurations are conducted and shown in the following sections.

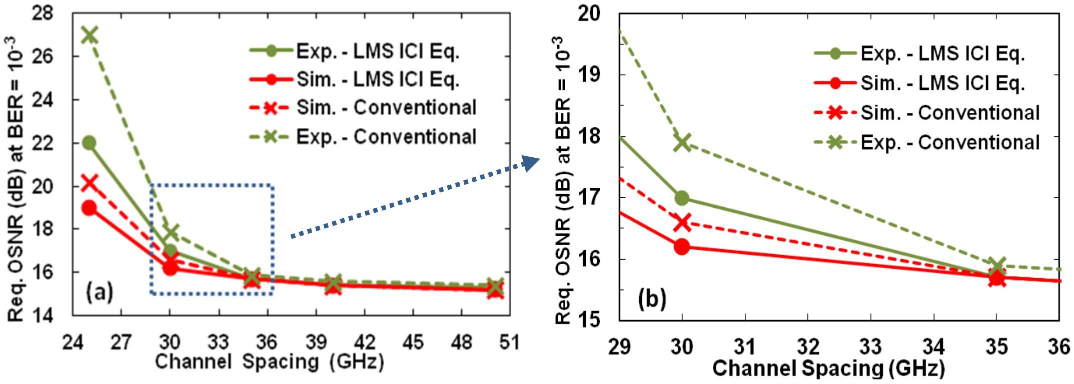

Figure 4.9. Comparison between the joint LMS ICI equalizer and conventional independent channel methods for both experimental and simulation results of the two-subchannel 28GBaud system.

4.3.2 3-Subchannel Simulation Tests

As mentioned, Scenario 1 is an extreme case without Tx spectral shaping and the two-subchannel setup does not capture all the crosstalk on both side of the subchannel. Therefore, a three-subchannel configuration of Scenario 2 was studied via simulation to test the joint DSP methods under more practical subchannel filtering conditions.

We performed simulation analysis of 3×32Gbaud (3x128Gb/s) DP-QPSK superchannel system with different optical filters applied and optimized to reduce ICI while minimizing the induced ISI penalty. The simulation setup is shown in Figure 4.10.

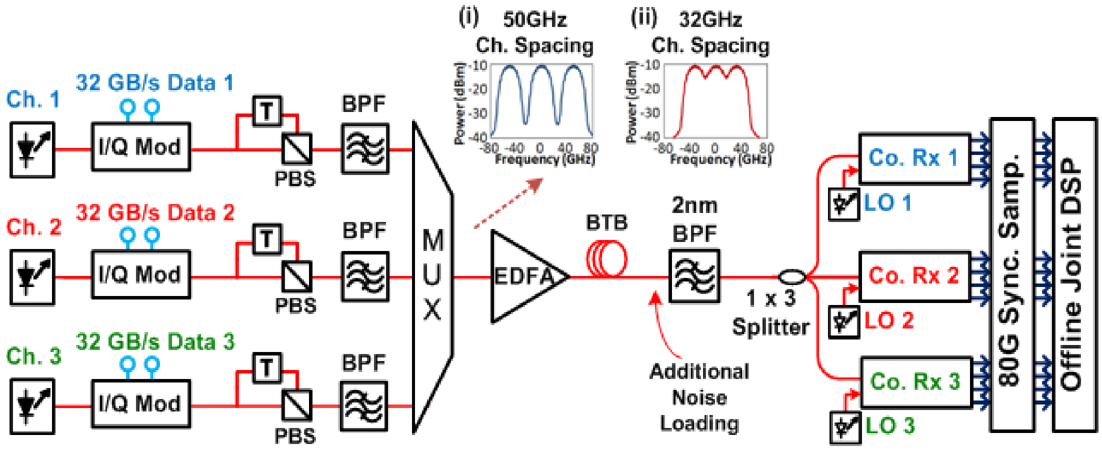

Figure 4.10. Simulation setup of 3 channel x 32Gbaud/s DP-QPSK superchannel signal transmission with joint detection and joint DSP.

The optical filter shape was chosen as super-Gaussian with order 3.5, which is a reasonable model for most AWGs (Arrayed Waveguide Gratings) and WSSs (Wavelength Selective Switches) used in conventional DWDM systems. Therefore, no special design of either Tx optical shaping filters or electrical pulse shaping is required in the system examined. The optical filter bandwidth (BW) was varied from 24GHz to 50GHz. At the receiver side, three sampling receivers were synchronously triggered, with the digital sampling rate of 80GSample/s per subchannel. The electrical filters at the digitizer were 10th order Bessel filters with a 30GHz 3dB bandwidth. The relatively wide electrical bandwidth minimizes the fixed electrical filtering effects, emphasizing the optimization of the optical filter bandwidth. It is noted that for a given channel spacing and channel filtering condition, the equalizers in the DSP will adjust their filter shapes adaptively to yield an optimized performance. The overall optimal performance still needs to be examined under different combinations of optical filter BW and channel spacing conditions.

Firstly we tested the required OSNR to obtain both 10^{-2} and 10^{-3} BER vs. channel spacing. We compared the conventional method with our ICI cancellation algorithm under different optical filter bandwidth configurations, as shown in Figure 4.11.

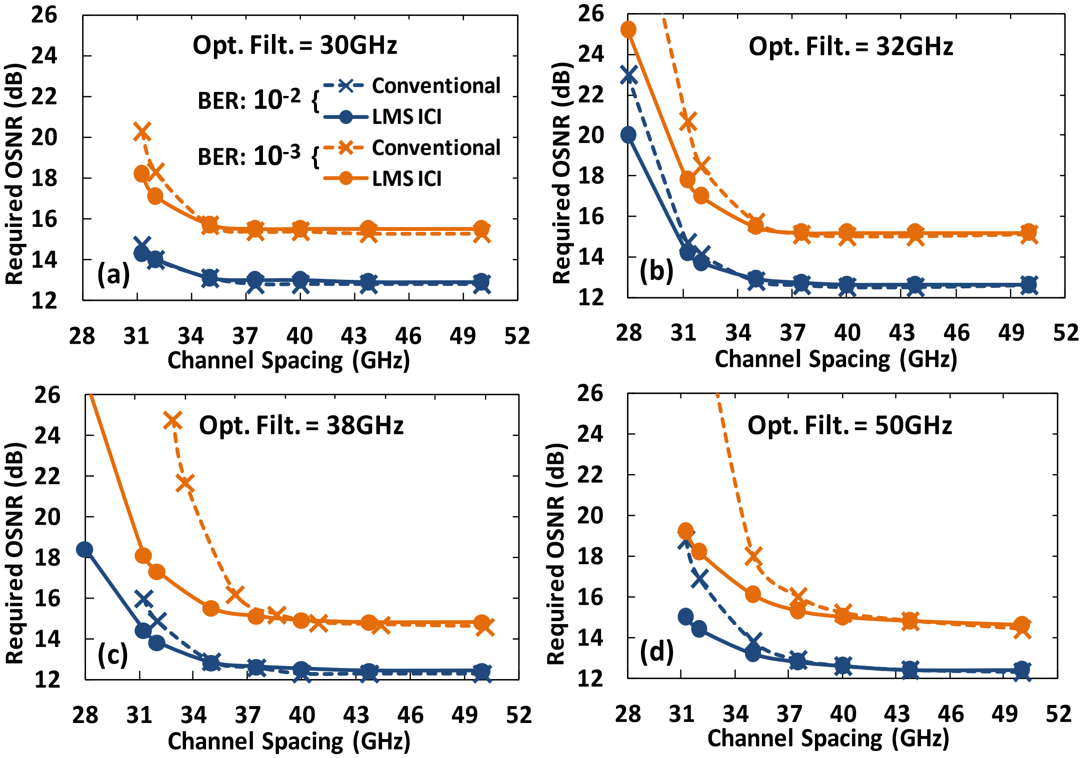

Figure 4.11. Required OSNR to obtain BER = 10^{-2} and 10^{-3} vs. channel spacing under different optical filter bandwidth configurations (three-subchannel 32GBaud BTB setup, scenario 2).

For all the optical filter bandwidth cases (Figure 4.11 (a) to (d)), the absolute performance deteriorates as the channel spacing decreases. The joint LMS ICI cancellation algorithm always shows performance gain over conventional methods at narrow channel spacing in all the filter bandwidth cases. For the very narrow optical filter case (30GHz, Figure 4.11(a)), the joint DSP method provides less benefits due to the reduced ICI from narrow filtering. However, very narrow filtering induces ISI penalties, which can be seen by comparing the performance floors in Figure 4.11 (a) and (d) at wide channel spacing cases (near 50GHz). In particular, the required OSNR to achieve BER = 10^{-3} for the 30GHz optical filter case (15.8dB) is about 1dB higher than for the 50GHz optical filter case (14.8dB) while both are in the ICI-free regimes (near 50GHz channel spacing). Narrower filtering results in dramatically larger ISI penalties. Therefore, a trade-off between ISI and ICI exists, which requires optimal design of the optical filter bandwidth for a given channel spacing.

To investigate the optimal filter bandwidth for a given channel spacing, we determined the required OSNR to obtain a specific BER (10^{-2} and 10^{-3}) vs. optical filter bandwidth under different channel-spacing conditions, as shown in Figure 4.12.

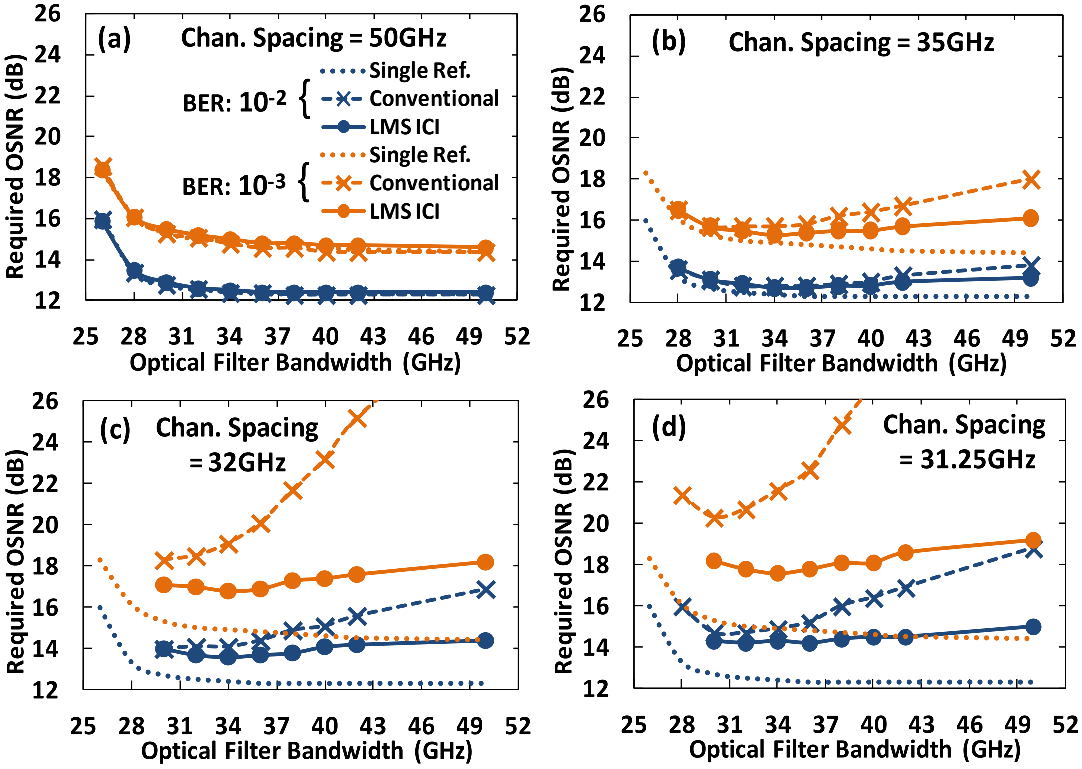

Figure 4.12. Required OSNR to obtain BER = 10-2 and 10-3 vs. optical filter BW under different channel spacing conditions (three-subchannel 32GBaud BTB setup, scenario 2).

At wide channel spacing case (50GHz; Figure 4.12(a)), both methods approach the single-channel reference limit, since there is negligible ICI. At narrow optical filter bandwidth strong ISI penalties occur and the intra-channel equalizer in each method is equally effective. Thus, when there is negligible ICI, it is preferable to maintain as large an optical filter bandwidth as possible. As the channel spacing is reduced (35GHz; Figure 4.12(b)), ICI penalties appear at wide optical filter bandwidths. ICI cancellation now yields a distinct advantage, reducing the penalty and producing the insensitivity to optical filter bandwidth. For Nyquist channel spacing (32GHz; Figure 4.12(c)) and narrower (31.25GHz; Figure 4.12(d)), stronger ICI penalties are observed for the conventional method. However, with the LMS ICI cancellation algorithm applied, the ICI penalties are significantly reduced. Again the performance is insensitive to filter bandwidth, in contrast to the conventional demodulation which exhibits a very strong dependence on optical filter bandwidth. For example, for the sub-Nyquist spacing of 31.25GHz, the optimal filter bandwidth for the conventional method is ~30GHz with the required OSNR of 20dB to achieve BER = 10^{-3}. The LMS ICI equalizer yields ~18dB OSNR requirement for any filter bandwidth. Thus, joint LMS ICI cancellation methods produce better absolute performance, and relax the optical filter bandwidth requirement.

Based on the results shown in Figure 4.12, we chose an optical filter BW of 34GHz for the Nyquist spacing case (32GHz) and examined the performance over a 12-span transmission link. Three-subchannel signals were transmitted through 12 spans of 80km SSMF with launch power of 0dBm per subchannel. We compared the results with single channel reference and the back-to-back (BTB) case, Figure 4.13(a). In order to successfully cancel the crosstalk through the LMS ICI equalizer, a joint chromatic-dispersion compensation is required in front of the joint DSP. This shifts the reference frequency of frequency-domain CD compensation of the side-subchannels to align with the center channel of interest.

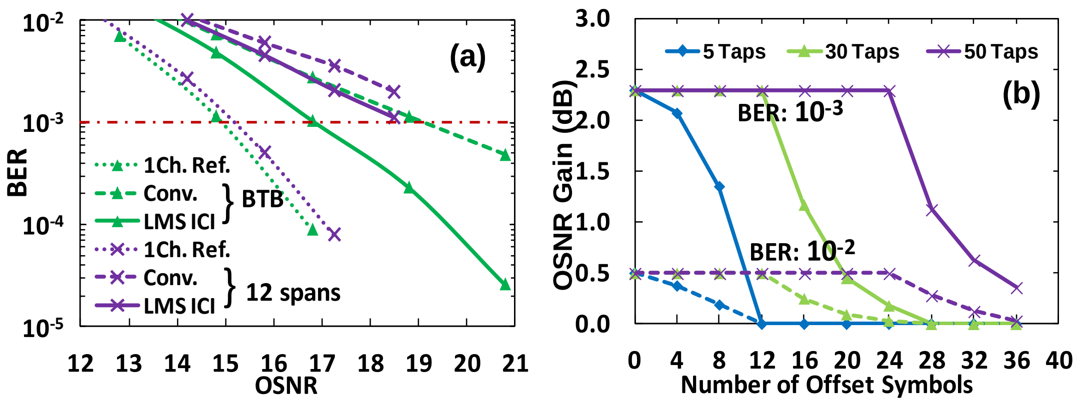

Figure 4.13. (a) BER vs. OSNR of LMS ICI equalization and conventional methods for both BTB and through 12 spans (960km). Three 32GBaud subchannels at Nyquist channel spacing with 34GHz optical filters. Single channel performance is shown for reference; (b) OSNR gain at BER = 10-2 (dashed) and 10-3 (solid) vs. the number of time-domain offset symbols under different ICI-filter tap lengths.

Firstly, the BTB performance is shown, demonstrating again a 2.3dB OSNR gain of the joint method compared to the conventional method at BER = 10^{-3}. After 12 spans (960km) of SSMF transmission, the single channel performance shows only a small penalty compared to the BTB case. On the other hand, the 12-span multi-channel conventional DSP case reveals a penalty >5dB with respect to the single-channel BTB case, and ~1dB penalty compared to the multi-channel BTB case. With the ICI equalizer applied, the penalty is reduced by ~1.5dB, which demonstrates the effectiveness of the joint DSP for both back-to-back and after fiber transmission cases.

To study the effect of timing offset between subchannels due to the imperfect synchronization or path mismatch across the coherent receivers, we determined the OSNR gain with respect to the number of time-domain offset symbols. The OSNR gain is measured under the optimized system setup at 32GHz channel spacing with 34GHz optical filter bandwidth. Different ICI-filter tap lengths in the LMS ICI equalizer were tested as shown in Figure 4.13(b). Note that the ICI equalizer operates with 2 samples per symbol, so filter length of 5 taps spans 2.5 symbols. As the results indicate, as long as the number of offset symbols is within the filter memory range, the ICI equalizer is effective. Thus by increasing the filter tap length, it is more tolerant to the timing offset. These results demonstrate that the requirement of perfect synchronized sampling and exact path matching among the subchannels can be relaxed if appropriate time-domain memory is applied in the ICI equalizer.

Joint carrier-phase recovery requires phase-locked sources and LO's. Therefore we examined simulations with phase-locked carriers under system scenario 2. In the simulation, the phase-locked carriers were generated by a phase modulator, which was driven by a sinusoidal RF wave that determines the channel spacing between the carriers. Each subchannel carried 28Gbaud DP-QPSK data and was spectrally shaped by a 3.5th order super-Gaussian optical filter of 38GHz. At the receiver, the superchannel signal was passive split and fed into three coherent receivers, and the corresponding phase-locked LOs were generated in the same way as at the transmitter side. The digital sampling rate was 40GSample/s per subchannel, and the bandwidth of electrical filters was set to 19GHz. The linewidth of the lasers was fixed at 0.1MHz and the Tx laser and LO are assumed to be perfectly aligned in frequency domain. In practice, methods to track the relative wavelength drift between the sources and LO's are feasible and are similar to the frequency-offset estimation for conventional single channel demodulation. Both three-subchannel and five-subchannel configurations were tested. The BER vs. OSNR results with and without joint carrier-phase recovery reveals a consistent ~0.5dB improvement at all channel spacing conditions, Figure 4.14(a). Further investigations of a five-subchannel (channel spacing at 31.25GHz) simulation allowed a comparison of three different carrier-phase recovery algorithms: conventional V-V, joint V-V, and joint V-V using only outer-subchannels phase information, Figure 4.14(b). For the last method, the estimated carrier phase of the two outer subchannels was averaged and the estimated phase information was used to update all the inner channels. It is found that this method works as well as the joint V-V case, demonstrating the effectiveness of using only the outer-subchannel carrier-phase information to recover all the inner-channel carrier phase. The improvement of joint V-V over conventional V-V is ~1/3dB for all OSNR cases. Since this joint V-V algorithm is compatible with the joint ICI equalizer based on the same “super receiver” architecture, it is beneficial to implement this joint V-V algorithm in phase-locked superchannel systems to provide additional performance gain.

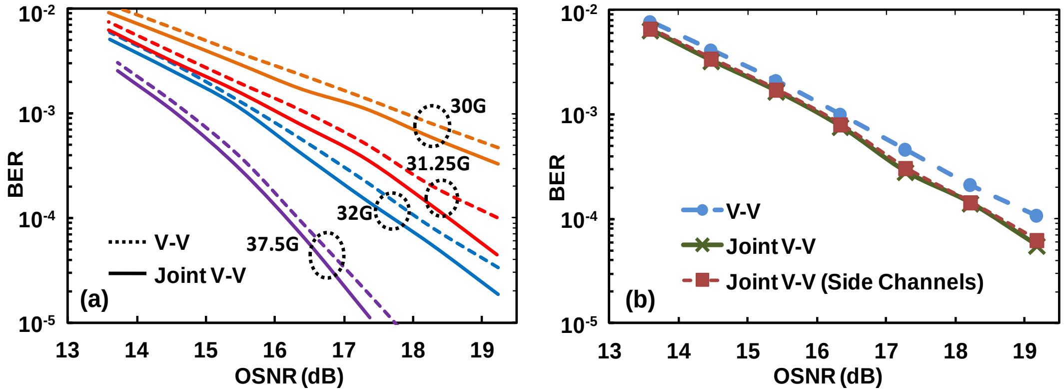

Figure 4.14. (a) Joint carrier phase recovery performance for three-subchannel BTB configurations at different channel-spacings. Conventional Viterbi-Viterbi (V-V) methods shown as reference; (b) Five-subchannel case, 31.25GHz channel spacing, for joint V-V on all 5 subchannels and joint V-V only using outer channels.

4.3.3 **Performance Test in the Nonlinear Transmission Regimes**

Previous results have demonstrated the efficacy of the joint DSP algorithms in both back-to-back and fiber transmission in the linear regimes. However, for long-haul core networks, it is important to investigate the performance of the joint DSP algorithms in the nonlinear transmission regimes.

The simulation setup is shown in Figure 4.15 [84]. Three independent lasers each carrying independent 32Gbaud/s DP-QPSK signals are multiplexed together by an optical coupler. Separate optical filters are applied to each sub-channel to control spectral shape and ICI before multiplexing. The optical filter shape is 3.5th order super- Gaussian with 3dB bandwidth of 32GHz. This optical filter shape is chosen as a reasonable model for commonly used AWGs (Arrayed Waveguide Gratings) and WSSs (Wavelength Selective Switches) in conventional WDM systems. Thus neither specific optical filter design nor electrical pulse shaping (through high-speed DAC) is used. After optical filters, the multiplexed optical spectra at channel spacing of 50GHz and 32GHz (Nyquist limit) are shown in the Figure 4.15 inset (i) and (ii), respectively. This produces negligible ICI for the conventional grid 50GHz case and severe crosstalk for the Nyquist spacing 32GHz case.

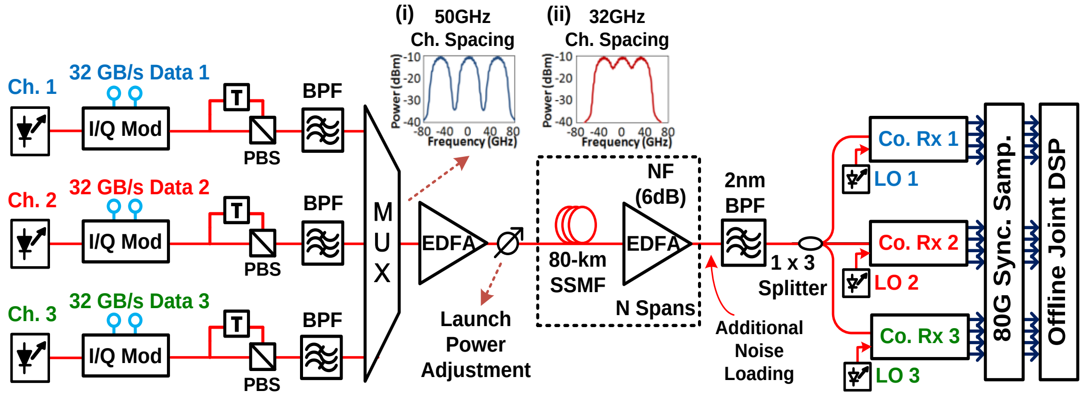

Figure 4.15. Simulation setup of 3 channel x 32Gbaud DP-QPSK superchannel signal transmission in the nonlinear regimes.

The superchannel signals are transmitted through multiple spans of 80km standard single-mode fiber (SSMF) with in-line EDFAs (Noise Figure = 6dB). The launch power per subchannel is adjustable by an optical attenuator at the beginning of the first span. At the receiver, after 1 x 3 optical splitter and coherent detection, three subchannel signals are synchronously sampled at 80GSample/s per sub-channel. The electrical filters at the digitizer are 10th order Bessel filters with 30GHz bandwidth minimizing electrical filtering effects. Sampled signals are offline processed by comparing independent DSP (independent CD compensation and without joint ICI cancellation) with joint DSP. Here joint DSP refers to joint CD compensation plus joint ICI cancellation (joint carrier phase estimation is not applicable due to phase-unlocked Tx lasers).

We first tested the BER vs. optical launch power per subchannel for 12 spans (960km; Figure 4.16(a)) and 16 spans (1280km; Figure 4.16(b)) fiber transmission cases. At lower launch power regimes, the performance is limited by the ASE noise induced by EDFAs (no additional noise loading is used). In the linear regime increased launch power results in an increased optical signal to noise ratio (OSNR) and better BER performance. However, eventually higher launch powers induce strong nonlinear effects, and the BER performance starts to degrade. Thus there exists an optimal operating regime. By comparing 32GHz with 50GHz channel spacing cases, severe performance degradation is observed at 32GHz, which is due to the combination of strong ICI and enhanced nonlinear effects especially at high launch powers. However, by applying the joint DSP for ICI cancellation at 32GHz channel spacing case, the performance gap between 50GHz and 32GHz channel spacing cases is reduced by as much as two orders of magnitude, especially at the optimal operation regime. The same trend is found for both 12 span and 16 span transmission cases. At 50GHz channel spacing case, no performance gain is observed for the proposed joint DSP algorithm due to the minimal ICI at 50GHz channel spacing.

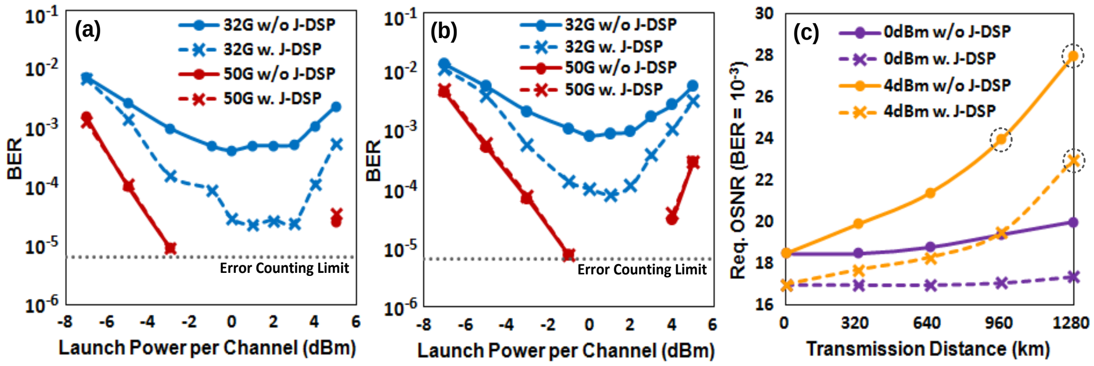

Figure 4.16. BER vs. optical launch power per channel for with and without joint DSP cases at different subchannel spacings (32GHz and 50GHz): (a) After 12 spans (960km) SSMF transmission; (b) After 16 spans (1280km) SSMF transmission. (c) Required OSNR to achieve BER = 10-3 vs. transmission distances at different optical launch powers (0dBm and 4dBm) for the 32GHz channel spacing case. All results are at 32Gbaud.

By looking at the nonlinear transmission regimes (+1 ~ +5dBm launch power) in Figure 4.16 (a) and (b), it shows that the performance of both independent and joint DSP algorithms decrease as more nonlinear noise occurs, and the BER improvement of the joint DSP seems to diminish in the nonlinear regime. To examine this, a test of the required OSNR to achieve a certain BER (10^{-3}) at different transmission distances and launch powers is conducted as shown in Figure 4.16(c). The required OSNR values are obtained by measuring the BER vs. OSNR curves for each data point, which are enabled by the additional tunable noise loading to adjust the received OSNR. Notice that the three circled data points on the plot are estimated from linear extrapolations of the BER vs. OSNR curves due to the very-high required OSNR value that cannot be achieved even without additional noise loading. At 4dBm launch power, the nonlinear effects degenerate the performance for both independent and joint DSP compared to 0dBm launch power case. However, for the linear ICI cancellation, the OSNR gain of the joint DSP maintains and even slightly increases in the nonlinear regimes. It is observed that 5dB OSNR gain can be achieved in the high nonlinear regime after 1280km fiber transmission at launch power of 4dBm. The “discrepancies” in the results interpretations (between Figure 4.16(a, b) and Figure 4.16(c)) at nonlinear regimes are due to the different shapes of BER vs. OSNR curves at different launch powers (Higher launch powers result in worse BER vs. OSNR curves and more gentle slopes). Therefore, from Figure 4.16(c), we conclude that the proposed joint DSP algorithm is effective to cancel the linear ICI even in the nonlinear regimes. However, to cancel the nonlinear ICI, it requires additional nonlinear models implemented in the joint ICI equalization block, and this is left as future work.

4.4 Summary

A novel coherent receiver architecture for superchannel coherent optical systems is proposed and demonstrated. Based on this “super receiver” structure, joint DSP algorithms for linear-ICI cancellation and joint carrier-phase recovery are developed and demonstrated through experimental and simulation results.

The ICI cancellation algorithm was shown to systematically improve performance whenever spectral overlap occurs between adjacent subchannels. Timing offset between subchannels was shown to be readily managed by increasing the time-domain memory size of the ICI equalizer. We also demonstrated that the proposed Rx-side approach can be optimized together with either electrical or optical spectral shaping at the Tx to create a more flexible solution for a dynamic network. Furthermore we showed that the joint ICI cancellation methods enable sub-Nyquist channel spacing with modest penalty. The joint ICI cancellation algorithm has been shown to be effective in both linear and nonlinear fiber transmission regimes.

For the joint carrier-phase recovery algorithm, consistent performance improvement over the conventional Viterbi-Viterbi carrier-phase recovery algorithm was observed in carrier phase-locked systems, and the feasibility of using only outer-subchannel phase information for all the inner-subchannel carrier-phase recovery was successfully demonstrated.

As a result, the proposed “super receiver” architecture enables joint digital signal processing to compensate cross-channel impairments as well as more accurate estimation of transmission channel characteristics, and therefore greatly enhance coherent receiver performance for highly spectral-efficient superchannel systems.

CHAPTER 5: CONCLUSIONS

The final chapter concludes my research works in next-generation converged optical-wireless access systems and high-speed coherent optical communication systems. Technical contributions of this research work are presented in Section 5.1. Potential research directions for future development related to this work are discussed in Section 5.2.

5.1 Technical Contributions

This dissertation investigates the system design and signal processing techniques of next-generation converged optical-wireless access systems and high-speed coherent optical communication systems. Several technical contributions are summarized as follows.

5.1.1 Next-Generation Converged Optical-Wireless Access Systems

- Cloud-radio-over-fiber (cloud-RoF) access system is proposed and investigated for next-generation small-cell wireless access systems. The proposed cloud-RoF architecture provides a cost-effective and power-efficient solution for the deployment of large-scale small-cell wireless access systems.
- A multi-service reconfigurable small-cell cloud-RoF system is designed and demonstrated. By taking advantage of centralized processing power of the cloud-RoF architecture, a reconfigurable backhaul network is proposed and demonstrated to serve different traffic-load areas and different mobile user patterns. In addition, the combination of radio-over-fiber (RoF) technologies and wavelength division multiplexing (WDM) techniques enables optical

infrastructure sharing among multiple services/operators while maintaining independent reconfigurability.

- The convergence of cloud-RoF architecture and 60GHz millimeter-wave radio is investigated. Several novel system designs are proposed that enable advanced modulation format transmission in millimeter-wave cloud-RoF systems in a simplified way.

5.1.2 High-Speed Coherent Optical Communication Systems

- Superchannel coherent systems to achieve ultra-high-speed long-haul optical communication are investigated. A “super receiver” architecture is proposed that jointly detects and demodulates multiple channels simultaneously and mitigates the penalties associated with the limitations of generating ideal superchannel spectra. Several joint DSP algorithms are developed for linear ICI cancellation and joint carrier-phase recovery.
- Several joint digital signal processing algorithms, including joint inter-channel interference cancellation, joint chromatic-dispersion compensation, and joint carrier phase recovery algorithm, are developed and demonstrated. Performance analysis under different system configurations is conducted, and improved system performance is observed with both experimental and simulation data.

5.2 Future Work

For next-generation converged optical-wireless access systems, the utilization of 60GHz mm-wave band for small-cell cellular communication still has several challenges need to be solved. These challenges include: mm-wave beam forming and beam steering for non-line-of-sight wireless channel; low-cost low-power mm-wave integrated circuit design for handheld devices; intelligent hand-off and coordination between in-building mm-wave small-cell and outdoor macrocell (form a heterogeneous network).

For high-speed superchannel coherent optical communication systems, base on the proposed “super receiver” architecture, the nonlinear ICI modeling and cancellation is a promising area to look into, which would take the full advantage of the joint detection and joint DSP architecture to further extend the optical reach. In addition, investigations on how to implement the joint DSP algorithms into practical coherent systems based on current ASIC technologies is very important, which may lead to further algorithm simplification and architectural modifications.

REFERENCES

[1] Cisco Visual Networking Index: Forecast and Methodology, 2009–2014.

[2] Cisco Visual Networking Index: Forecast and Methodology, 2011–2016.

[3] Cisco Visual Networking Index: Global Mobile Data Traffic Forecast Update, 2009–2014.

[4] Cisco Visual Networking Index: Global Mobile Data Traffic Forecast Update, 2011–2016.

[5] S. M. Alamouti, “Network of the future: some challenges ahead,” Wireless Communication and Networking Conference (WCNC) 2012, Keynote Speech.

[6] M. Medin, “Bandwidth, optics and the age of abundance,” Optical Fiber Communication Conference (OFC) 2012, Keynote Speech.

[7] Ericsson, “Heterogeneous network: Meeting mobile broadband expectations with maximum efficiency,” in White Paper, 2012.

[8] China Mobile, “C-RAN: The road towards green ran,” in White Paper, 2011.

[9] Alcatel-Lucent, “LightRadio network: A new wireless experience,” in White Paper, 2012.

[10] Nokia Siemens Networks, “Liquid radio: Let traffic waves flow most efficiently,” in White Paper, 2011.

[11] D. Gesbert, S. Hanly, H. Huang, S. S. Shitz, O. Simeone, and W. Yu, “Multi-cell MIMO cooperative networks: A new look at interference,” IEEE J. Select. Areas Commun., vol. 28, no. 9, pp. 1380–1408, Dec. 2010.

[12] Common Public Radio Interface (CPRI), The CPRI Specification version 5.0, 2011. Available at: http://www.cpri.info/.

[13] Open Base Station Architecture Initiative (OBSAI). Available at: http://www.obsai.com.

[14] G.-K. Chang, C. Liu, "Architecture and applications of a versatile small-cell, multi-service cloud radio access network using radio-over-fiber technologies," IEEE International Conference on Communications (ICC) 2013, Invited Paper.

[15] IEEE 802.15.3c Working Group Homepage, available at http://www.ieee802.org/15/pub/TG3c.html.

[16] Standard ECMA-387, "High rate 60 GHz PHY, MAC and HDMI PAL", Dec. 2008.

[17] WirelessHD™ 1.0 Specification, http://www.wirelesshd.org/.

[18] IEEE 802.11ad PAR (2009), https://development.standards.ieee.org/get-file/P802.11ad.pdf?t=29195900024.

[19] Wireless Gigabit Alliance (WiGig) (2009) http://wirelessgigabitalliance.org/news/wigigalliance-publishes-multi-gigabit-wireless-specification-and-launches-adopter-program/.

[20] H.T. Friis, "A note on a simple transmission formula," Proc. IRE, vol. 34, p. 254, 1946.

[21] Optical Zonu Corp. Module OZ1606, "7GHz ultra premium RF over fiber transceiver," http://www.opticalzonu.com/rfofproducts/standalone/oz1606/

[22] Pharad. Module PXR-030-400-N, “3 - 40GHz RF photonic transceivers,” http://www.pharad.com/rf-photonic-transceivers.html

[23] G.-K. Chang, A. Chowdhury, Z. Jia, H.-C. Chien, M.-F. Huang, J. Yu, and G. Ellinas, “Key technologies of WDM-PON for future converged optical broadband access networks,” Journal of Optical Communication and Network, vol. 1, no. 4, pp. C35-C50, 2009.

[24] A. Koonen and L. Garcia, "Radio-over-mmf techniques-part II: microwave to millimeter-wave systems," J. Lightw. Technol., vol. 26, no. 15, pp. 2396-2408, 2008.

[25] A. Chowdhury, H.-C. Chien, Y.-T. Hsueh, and G.-K. Chang, “Advanced system technologies and field demonstration for in-building optical-wireless network with integrated broadband services,” J. Lightw. Technol., vol. 27, no. 22, pp. 1920-1927, 2009.

[26] Z. Jia, J. Yu, G. Ellinas, and G.-K. Chang, "Key enabling technologies for optical-wireless networks: optical millimeter-wave generation, wavelength reuse, and architecture," J. Lightw. Technol., vol. 25, no. 11, pp. 3452-3471, 2007.

[27] J. Olmos, T. Kuri, and K. Kitayama, "Dynamic reconfigurable WDM 60-GHz millimeter-waveband radio-over-fiber access network: architectural considerations and experiment," J. Lightw. Technol., vol. 25, no. 11, pp. 3374-3380, 2007.

[28] A. J. Seeds and K. J. Williams, “Microwave photonics,” J. Lightw. Technol., vol. 24, no. 12, pp. 4628-4641, 2006.

[29] C. Lim, A. Nirmalathas, D. Novak, R. Waterhouse, and G. Yoffe, "Millimeter-wave broadband fiber-wireless system incorporating baseband data transmission over fiber and remote LO delivery", J. Lightw. Technol., vol.18, no. 10, pp. 1355-1363, 2000.

[30] A. Nirmalathas, C. Lim, D. Novak, and R.B. Waterhouse, "Progress in millimeter-wave fiber-radio access networks", Annals of Telecommunications, vol. 56, no.1, pp. 1-12, 2001.

[31] K. Kitayama, A. Stohr, T. Kuri, R. Heinzelmann, D. Jager, and Y. Takahashi, “An approach to single optical component antenna base stations for broad-band millimeter-wave fiber-radio access systems,” IEEE Trans. Microw. Theory Tech., vol. 48, no. 12, pp. 2588-2595, 2000.

[32] Z. Jia, J. Yu, and G.-K. Chang, “All-optical 16 × 2.5 Gb/s WDM signals simultaneous up-conversion based on XPM in an NOLM in RoF systems,” IEEE Photon. Technol. Lett, vol. 17, no. 12, pp. 2724-2726, 2005.

[33] J. Liu, H.-C. Chien, S.-H. Fan, B. Chen, J. Yu, S. He, G.-K. Chang, “Efficient optical millimeter-wave generation using a frequency-tripling Fabry–Pérot laser with sideband injection and synchronization,” IEEE Photon. Technol. Lett., vol. 23, no. 18, pp. 1325-1327, 2011

[34] J. Yu, Z. Jia, L. Yi, Y. Su, G.-K. Chang, and T.Wang, “Optical millimeter-wave generation or up-conversion using external modulators,” IEEE Photon. Technol. Lett., vol. 18, no. 1, pp. 265-267, 2006.

[35] J. Yu, Z. Jia, L. Xu, L. Chen, T. Wang, and G.-K. Chang, “DWDM optical millimeter-wave generation for radio-over-fiber using an optical phase

modulator and an optical interleaver," IEEE Photon. Technol. Lett., vol. 18, no. 13, pp. 1418-1420, 2006.

[36] J. Ma, J. Yu, C. Yu, X. Xin, J. Zeng, and L. Chen, "Fiber dispersion influence on transmission of optical millimeter-waves generated using LN-MZM intensity modulation," J. Lightw. Technol., vol. 25, no. 11, pp. 3244-3256, 2007.

[37] TR 22.951 3GPP, "Service aspects and requirements for network sharing," in Technical Reprt, Dec. 2009. http://ftp.3gpp.org/specs/html-info/22951.htm.

[38] TR 23.251 3GPP, "Network sharing; architecture and functional description," in Technical Reprt, Mar. 2010. http://ftp.3gpp.org/specs/html-info/23251.htm.

[39] K. Roberts, M. O'Sullivan, K.-T. Wu, H. Sun, A. Awadalla, D. J. Krause, and C. Laperle, "Performance of dual-polarization QPSK for optical transport systems," J. Lightwave Technol. vol. 27, no. 16, pp. 3546-3559, 2009.

[40] J. Renaudier, O. Bertran-Pardo, H. Mardoyan, P. Tran, G. Charlet, S. Bigo, M. Lefrancois, B. Lavigne, J-L. Auge, L. Piriou, O. Courtois, "Performance comparison of 40G and 100G coherent PDM-QPSK for upgrading dispersion managed legacy systems," Optical Fiber Communication Conference (OFC) 2009, NWD5.

[41] R. Ryf, S. Randel, A.H. Gnauck, C. Bolle, A. Sierra, S. Mumtaz, M. Esmaeelpour, E. C. Burrows, R.-J. Essiambre, P. J. Winzer, D.W. Peckham, A.H.McCurdy, and R. Lingle, Jr., "Mode-division multiplexing Over 96 km of few-mode fiber using coherent 6x6 MIMO processing," J. Lightwave Technol. vol. 30, no. 4, pp. 521-531, 2012.

[42] P. J. Winzer and G. J. Foschini, “MIMO capacities and outage probabilities in spatially multiplexed optical transport systems,” Opt. Exp., vol. 19, no. 17, pp. 16680-16696, 2011.

[43] J. Sakaguchi, B. J. Puttnam, W. Klaus, Y. Awaji, N. Wada, A. Kanno, T. Kawanishi, K. Imamura, H. Inaba, K. Mukasa, R. Sugizaki, T. Kobayashi, M. Watanabe, “19-core fiber transmission of 19x100x172-Gb/s SDM-WDM-PDM-QPSK signals at 305Tb/s,” Optical Fiber Communication Conference (OFC) 2012, PDP5C.1.

[44] T. Wuth, M.W. Chbat, V.F. Kamalov, “Multi-rate (100G/40G/10G) transport over deployed optical networks,” Optical Fiber Communication Conference (OFC) 2008, NTuB3.

[45] G. Raybon, P. J. Winzer, and C. R. Doerr, "1-Tb/s (10×107 Gb/s) electronically multiplexed optical signal generation and WDM transmission," J. Lightwave Technol., vol.25, no.1, pp. 233-238, 2007.

[46] F. Buchali, K. Schuh, D. Rosener, E. Lach, R. Dischler, W. Idler, L. Schmalen, A. Leven, R.-P. Braun, A. Ehrhardt, C. Gerlach, L. Schurer, “512-Gb/s DP-16-QAM field trial over 734 km installed SSMF with copropagating 10 Gb/s NRZ neighbors incorporating soft-FEC decoding,” Optical Fiber Communication Conference (OFC) 2012, OW4C.4.

[47] P. J. Winzer, A. H. Gnauck, S. Chandrasekhar, S. Draving, J. Evangelista, and B. Zhu, “Generation and 1,200-km transmission of 448-Gb/s ETDM 56-Gbaud PDM 16-QAM using a single I/Q modulator,” Eur. Conf. Opt. Commun. (ECOC) 2010, PD2.2.

[48] S. Chandrasekhar, X. Liu, "Experimental investigation on the performance of closely spaced multi-carrier PDM-QPSK with digital coherent detection," Opt. Exp., vol. 17, no. 24, pp. 21350-21361, 2009.

[49] J.-X. Cai, C. R.Davidson, A. Lucero, H. Zhang, D. G. Foursa, O. V. Sinkin, W. W. Patterson, A. N. Pilipetskii, G. Mohs, N. S. Bergano, "20Tbit/s transmission over 6860 km with sub-Nyquist channel spacing," J. Lightwave Technol., vol. 30, no. 4, pp. 651-657, 2012.

[50] T. J. Xia, G. A. Wellbrock, Y,-K. Huang, E. Ip, M.-F. Huang, Y. Shao, T. Wang, Y. Aono, T. Tajima, S. Murakami, M. Cvijetic, "Field experiment with mixed-line-rate transmission (112-Gb/s, 450-Gb/s, and 1.15-Tb/s) over 3,560 km of installed fiber using filterless coherent receiver and EDFAs only," Optical Fiber Communication Conference (OFC) 2011, PDPA3.

[51] Z. Jia, J. Yu, H.-C. Chien, Z. Dong, "Field transmission of 100G and beyond: multiple baud rates and mixed line rates using Nyquist-WDM technology," J. Lightwave Technol., Vol. 30, Issue 24, 2012.

[52] E. Torrengo, R. Cigliutti, G. Bosco, G. Gavioli. A. Alaimo, A. Carena, V. Curri, F. Forghieri, S. Piciaccia, M. Belmonte, A. Brinciotti, A. La Porta, S. Abrate, and P. Poggiolini, "Transoceanic PM-QPSK terabit superchannel transmission experiments at baud-rate subcarrier spacing," ECOC 2010, We.7.C.2.

[53] Y. Cai, J. X. Cai, C. R. Davidson, D. Foursa, A. Lucero, O. Sinkin, A. Pilipetskii, G. Mohs, and N. S. Bergano, "High spectral efficiency long-haul

transmission with pre-filtering and maximum a posteriori probability detection," ECOC 2010, We.7.C.4.

[54] X. Liu, S. Chandrasekhar, B. Zhu, P. J. Winzer, A. H. Gnauck, and D. W. Peckham, "Transmission of a 448-Gb/s Reduced-Guard-Interval CO-OFDM Signal with a 60-GHz Optical Bandwidth over 2000 km of ULAF and Five 80-GHz-Grid ROADMs," Optical Fiber Communication Conference (OFC) 2010, PDPC2.

[55] Y. Ma, Q. Yang, Y. Tang, S. Chen, and W. Shieh, "1-Tb/s per channel coherent optical OFDM transmission with subwavelength bandwidth access," Optical Fiber Communication Conference (OFC) 2009, PDPC1.

[56] R. Dischler and F. Buchali, "Transmission of 1.2 Tb/s continuous waveband PDM-OFDM-FDM signal with spectral efficiency of 3.3 bit/s/Hz over 400 km of SSMF," Optical Fiber Communication Conference (OFC) 2009, PDPC2.

[57] R. Schmogrow, M. Winter, M. Meyer, D. Hillerkuss, S. Wolf, B. Baeuerle, A. Ludwig, B. Nebendahl, S. Ben-Ezra, J. Meyer, M. Dreschmann, M. Huebner, J. Becker, C. Koos, W. Freude, and J. Leuthold, "Real-time Nyquist pulse generation beyond 100 Gbit/s and its relation to OFDM," Optics Express, vol. 20, no. 1, pp. 317-337, 2012.

[58] G. Bosco, A. Carena, V. Curri, P. Poggiolini, and F. Forghieri, "Performance limits of Nyquist-WDM and CO-OFDM in high-speed PM-QPSK systems," Photonics Technology Letters, vol. 22, no. 15, pp. 1129-1131, 2010.

[59] S. Chandrasekhar and X. Liu, "Terabit superchannels for high spectral efficiency transmission," ECOC 2010, Tu.3.C.5.

[60] D. Hillerkuss, M. Winter, M. Teschke, A. Marculescu, J. Li, G. Sigurdsson, K. Worms, W. Freude, J. Leuthold, “Low-complexity optical FFT scheme enabling Tbit/s all-optical OFDM communication,” ITG Symposium on Photonic Networks 2010, P5.

[61] K. Takiguchi, M. Oguma, T. Shibata, and H. Takahashi, “Optical OFDM demultiplexer using silica PLC based optical FFT circuit,” Optical Fiber Communication Conference (OFC) 2009, OWO3.

[62] G. Gavioli, E. Torrengo, G. Bosco, A. Carena, V. Curri, V. Miot, P. Poggiolini, M. Belmonte, F.Forghieri, C. Muzio, S. Piciaccia, A. Brinciotti, A. La Porta , C. Lezzi, S. Savory, and S. Abrate, “Investigation of the impact of ultra-narrow carrier spacing on the transmission of a 10-Carrier 1Tb/s superchannel,” Optical Fiber Communication Conference (OFC) 2010, OThD3.

[63] Y. Cai, J. X. Cai, C. R. Davidson, D. Foursa, A. Lucero, O. Sinkin, A. Pilipetskii, G. Mohs, and N. S. Bergano, “Achieving high spectral efficiency in long-haul transmission with pre-filtering and multi-symbol detection,” Asia Communications and Photonics Conference (ACP) 2010, p349.

[64] M. Arslan, J. Yoon, K. Sundaresan, S. Rangarajan, and S. Krishnamurthy, “Fermi: A femtocell resource management system for interference mitigation in ofdma networks,” in ACM MobiCom, Sept 2011.

[65] D. Jiang, J. Jin, Liu G, Z. Yan, and D. Yang, “Application of bbu+rru based comp system to lte-advanced,” in IEEE ICC Workshops, Jun 2009.

[66] The DAS Forum, www.thedasforum.org/news/.

[67] C. Liu, K. Sundaresan, M. Jiang, S. Rangarajan, G.-K. Chang, "The Case for Re-configurable Backhaul in Cloud-RAN based Small Cell Networks," IEEE INFOCOM 2013, paper accepted

[68] C. Liu, N. Cvijetic, K. Sundaresan, M. Jiang, S. Rangarajan, T. Wang, and G.-K. Chang, "A novel in-building small-cell backhaul architecture for cost-efficient multi-operator multi-service coexistence," Optical Fiber Communication Conf. (OFC) 2013, Paper OTh4A.4.

[69] C. Liu, H.-C. Chien, S.-H. Fan, J. Yu, G.-K. Chang, "Enhanced Vector Signal Transmission over Double-Sideband Carrier-Suppressed Optical Millimeter-Waves through a Small LO Feedthrough," IEEE Photonics Technology Letters (PTL), Vol. 23, Issue 3, Feb. 2012.

[70] C. Liu, H.-C. Chien, Z. Gao, W. Jian, A. Chowdhury, G.-K. Chang, "Multi-band 16QAM-OFDM Vector Signal Delivery over 60-GHz DSB-SC Optical Millimeter-Wave through LO Enhancement," Optical Fiber Communications Conference (OFC), March 2011, OThJ2.

[71] C. Liu, H.-C. Chien, Z. Gao, W. Jian, C. Estevez, J. Yu, G.-K. Chang, "Optimization of Vector Signal Delivery over Double-Sideband Suppressed-Carrier Optical Millimeter-Waves through DC Coupling," IEEE Photonics Technology Letters (PTL), Vol. 23, Issue 12, June 2011.

[72] P. J. Winzer, R.-J. Essiembri, "Advanced modulation formats for high-capacity optical transport networks," J. Lightwave Technol., vol. 24, no. 12, pp. 4711-4728, 2006.

[73] H.-C. Chien, A. Chowdhury, S.-H. Fan, D. Guidotti, Y.-T. Hsueh, Z. Jia, and G.-K. Chang, "Spectrum-compressed mm-wave wireless over fiber access system using duobinary line-coding at 10-Gbps and beyond," Optical Fiber Communication Conference (OFC) 2010, OThO1.

[74] J. Builting, "Introduction to duobinary encoding and decoding," Elektor Electronics, pp. 50-52, Jan. 1990.

[75] C. Liu, H.-C. Chien, S.-H. Fan, Y.-T. Hsueh, J. Liu, L. Zhang, J. Yu, G.-K. Chang, "A Novel Self-Mixing Duobinary RF Receiver for Millimeter-Wave Radio-over-Fiber Systems," Optical Fiber Communications Conference (OFC) Mar. 2012, OM2B.5.

[76] C. Liu, S.-H. Fan, L. Zhang, Y.-T. Hsueh, M. Zhu, A. Yi, C. Ye, H.-C. Chien, J. Yu, G.-K. Chang, "Duobinary RF Envelope Detector in Coherent Optical Millimeter-Wave Systems" IEEE Photonics Society 2012 Summer Topical Meetings, July 2012, WB3.3.

[77] I. P. Kamino, T. Li, and A.E. Willner, Optical Fiber Telecommunications V. A, Academic Press, 2008.

[78] Z. Dong, J. Yu, H.-C. Chien, N. Chi, L. Chen, G.-K. Chang, "Ultra-dense WDM-PON delivering carrier-centralized Nyquist-WDM uplink with digital coherent detection," Optics Express, vol. 19, no. 12, pp. 11100-11105, 2011.

[79] T. Detwiler, "Continuous phase modulation for high-speed fiber-optic links," Ph.D. dissertation, School of Electrical and Computer Engineering, Georgia Institute of Technology, Atlanta, GA, 2011.

[80] C. Liu, J. Pan, T. Detwiler, A. Stark, Y.-T. Hsueh, G.-K. Chang, S. E. Ralph, “Joint DSP for Superchannel Coherent Optical Systems: Joint CD Compensation for Joint ICI Cancellation,” European Conference on Optical Communications (ECOC), Oct. 2012, Th.1.A.4.

[81] A. J. Viterbi and A. M. Viterbi, “Nonlinear estimation of PSK-modulated carrier phase with application to burst digital transmission,” IEEE Trans. Inf. Theory, 29(4), Jul. 1983.

[82] C. Liu, J. Pan, T. Detwiler, A.Stark, Y.-T. Hsueh, G.-K. Chang, and S. E. Ralph, “Joint digital signal processing for superchannel coherent optical communication Systems,” Optics Express, Vol. 21, Iss. 7, pp. 8342–8356, Mar. 2013.

[83] J. Pan, C. Liu, T. Detwiler, A. Stark, Y.-T. Hsueh, S. E. Ralph, “Inter-channel Crosstalk Cancellation for Nyquist-WDM Superchannel Applications,” IEEE Journal of Lightwave Technology (JLT), Vol. 30, No. 24, Dec. 2012.

[84] C. Liu, J. Pan, T. Detwiler, A. Stark, Y.-T. Hsueh, G.-K. Chang, S. E. Ralph, “Joint ICI Cancellation for Superchannel Coherent Optical Systems in the Nonlinear Transmission Regimes,” Optical Fiber Communications Conference (OFC) 2013, OTu2I.4.

PUBLICATIONS

Journal Publications (12 journal papers):

[1] **C. Liu**, H.-C. Chien, S.-H. Fan, J. Yu, G.-K. Chang, "Enhanced Vector Signal Transmission over Double-Sideband Carrier-Suppressed Optical Millimeter-Waves through a Small LO Feedthrough," IEEE Photonics Technology Letters (PTL), Vol. 23, Issue 3, Feb. 2012.

[2] **C. Liu**, H.-C. Chien, Z. Gao, W. Jian, C. Estevez, J. Yu, G.-K. Chang, "Optimization of Vector Signal Delivery over Double-Sideband Suppressed-Carrier Optical Millimeter-Waves through DC Coupling," IEEE Photonics Technology Letters (PTL), Vol. 23, Issue 12, June 2011.

[3] **C. Liu**, J. Pan, T. Detwiler, A. Stark, Y.-T. Hsueh, G.-K. Chang, S. E. Ralph, "Joint Digital Signal Processing for Superchannel Coherent Optical Communication Systems," Optics Express, Vol. 21, Iss. 7, pp. 8342–8356, Mar. 2013.

[4] **C. Liu**, J. Pan, T. Detwiler, A. Stark, Y.-T. Hsueh, G.-K. Chang, S. E. Ralph, "Super-Receiver Design for Superchannel Coherent Optical Systems," ZTE Communications. Vol. 10, No. 1, March 2012, Invited Paper.

[5] **C. Liu**, L. Zhang, M. Zhu, J. Wang, L. Cheng, G.-K. Chang, "A Novel Multi-Service Small-Cell Cloud Radio Access Network for Mobile Backhaul and Computing Based on Radio-over-Fiber Technologies," IEEE Journal of Lightwave Technology (JLT), paper submitted, Feb. 2013.

[6] **C. Liu**, H.-C. Chien, S.-H. Fan, Y.-T. Hsueh, J. Yu, G.-K. Chang, “Duobinary RF Receivers for Bandwidth-Efficient Millimeter-Wave Radio-over-Fiber Systems,” Optics Letters, paper accepted with minor revisions, March. 2013.

[7] J. Pan, **C. Liu**, T. Detwiler, A. Stark, Y.-T. Hsueh, S. E. Ralph, “Inter-channel Crosstalk Cancellation for Nyquist-WDM Superchannel Applications,” IEEE Journal of Lightwave Technology (JLT), Vol. 30, No. 24, Dec. 2012.

[8] Y.-T. Hsueh, A. Stark, **C. Liu**, T. Detwiler, S. Tibuleac, M. Filer, G-K. Chang, S. E. Ralph, “Passband Narrowing and Crosstalk Impairments in ROADM-Enabled 100G DWDM Networks,” IEEE Journal of Lightwave Technology (JLT), Vol. 30, Issue 24, Dec. 2012.

[9] J. Liu, M. Zhu, S.-H. Fan, **C. Liu**, H.-C. Chien, J. Yu, G.-K. Chang, “Multi-band QPSK Signal Transmission Implemented with Remote Up-Conversion and Schottky RF Detectors in a 60-GHz Millimeter Wave Radio-over-Fiber System,” Optical Fiber Technology, Available online, Mar. 2013.

[10] A. Stark, Y.-T. Hsueh, S. Searcy, T. Detwiler, **C. Liu**, M. Filer, S. Tibuleac, G.-K. Chang, S. E. Ralph, “Scaling 112Gb/s Optical Networks with the Nonlinear Threshold Metric,” IEEE Journal of Lightwave Technology (JLT), Vol. 30, Issue 9, May 2012.

[11] L. Zhang, M. Zhu, C. Ye, S.-H. Fan, **C. Liu**, X. Hu, P. Cao, Q. Chang, Y. Su, G.-K. Chang, “Generation and Transmission of Multiband and Multi-Gigabit 60-GHz MMW Signals in a RoF System with Frequency Quintupling Technique,” Optical Express, Vol. 21, Issue 8, pp. 9899-9905, 2013.

[12] J. Yu, G.-K. Chang, Z. Jia, A. Chowdhury, M. Huang, H.-C. Chien, Y.-T. Hsueh, W. Jian, **C. Liu**, Z. Dong, “Cost-Effective Optical Millimeterwave Technologies and Field Demonstrations for Very High Throughput Wireless Over Fiber Access Systems,” IEEE Journal of Lightwave Technology (JLT), Vol. 28, Issue 16. August 2010, Invited Paper.

Conference Publications (40 conference proceedings):

[1] **C. Liu**, K. Sundaresan, M. Jiang, S. Rangarajan, G.-K. Chang, “The Case for Re-configurable Backhaul in Cloud-RAN based Small Cell Networks,” IEEE INFOCOM 2013, paper accepted.

[2] **C. Liu**, N. Cvijetic, K. Sundaresan, M. Jiang, S. Rangarajan, T. Wang, G.-K. Chang, “A Novel In-Building Small-Cell Backhaul Architecture for Cost-Efficient Multi-Operator Multi-Service Coexistence,” Optical Fiber Communications Conference (OFC) 2013, OTh4A.4.

[3] **C. Liu**, A. Yi, M. Zhu, J. Wang, L. Zhang, S.-C. Shin, Z. Dong, H.-C. Chien, J. Yu, C. Su, G. Gu, A. Ng'Oma, G.-K. Chang, “A Novel Direct-Modulation Envelope-Detection Pol-Mux MIMO RoF System based on Blind Equalization Techniques,” Optical Fiber Communications Conference (OFC) 2013, OM3D.6.

[4] **C. Liu**, J. Pan, T. Detwiler, A. Stark, Y.-T. Hsueh, G.-K. Chang, S. E. Ralph, “Joint ICI Cancellation for Superchannel Coherent Optical Systems in the Nonlinear Transmission Regimes,” Optical Fiber Communications Conference (OFC) 2013, OTu2I.4.

[5] **C. Liu**, J. Pan, T. Detwiler, A. Stark, Y.-T. Hsueh, G.-K. Chang, S. E. Ralph, "Joint DSP for Superchannel Coherent Optical Systems: Joint CD Compensation for Joint ICI Cancellation," European Conference on Optical Communications (ECOC), Oct. 2012, Th.1.A.4.

[6] **C. Liu**, S.-H. Fan, L. Zhang, Y.-T. Hsueh, M. Zhu, A. Yi, C. Ye, H.-C. Chien, J. Yu, G.-K. Chang, "Duobinary RF Envelope Detector in Coherent Optical Millimeter-Wave Systems" IEEE Photonics Society 2012 Summer Topical Meetings, July 2012, WB3.3.

[7] **C. Liu**, J. Pan, T. Detwiler, A. Stark, Y.-T. Hsueh, G.-K. Chang, S. E. Ralph, "Joint ICI Cancellation based on Adaptive Cross-Channel Linear Equalizer for Coherent Optical Superchannel Systems," OSA Signal Processing in Photonic Communications (SPPCom), May 2012, SpTu3A.2.

[8] **C. Liu**, H.-C. Chien, S.-H. Fan, Y.-T. Hsueh, J. Liu, L. Zhang, J. Yu, G.-K. Chang, "A Novel Self-Mixing Duobinary RF Receiver for Millimeter-Wave Radio-over-Fiber Systems," Optical Fiber Communications Conference (OFC) Mar. 2012, OM2B.5.

[9] **C. Liu**, J. Pan, T. Detwiler, A. Stark, Y.-T. Hsueh, G.-K. Chang, S. E. Ralph, "Super Receiver Design for Superchannel Coherent Optical Systems," Proceedings of the SPIE, 8284-4, Jan 2012.

[10] **C. Liu**, H.-C. Chien, Z. Gao, W. Jian, A. Chowdhury, G.-K. Chang, "Multi-band 16QAM-OFDM Vector Signal Delivery over 60-GHz DSB-SC Optical Millimeter-Wave through LO Enhancement," Optical Fiber Communications Conference (OFC), March 2011, OThJ2.

[11] **C. Liu**, W. Jian, H.-C. Chien, A. Chowdhury, G.-K. Chang, "Experimental Analysis and Optimization of Equalization Techniques for 60-GHz OFDM Radio-over-Fiber System," Optical Fiber Communications Conference (OFC), March 2010, JWA54.

[12] G.-K. Chang, **C. Liu**, "Small-cell, Multi-service Cloud Radio Access Network using Radio-over-Fiber Technologies," IEEE International Conference on Communications (ICC), 2013, Invited Paper.

[13] J. Wang, **C. Liu**, M. Zhu, G.-K. Chang, "Investigation of Intra/Inter-Band Cross-Modulation in Multiband Radio-over-Fiber Systems," IEEE International Conference on Communications (ICC), 2013, paper accepted.

[14] L. Cheng, **C. Liu**, Z. Dong, J. Yu, G.-K. Chang, "60-GHz and 100-GHz Wireless Transmission of High-Definition Video Services in Converged Radio-over-Fiber Systems," Conference on Lasers and Electro-Optics (CLEO), 2013, CM3G.2.

[15] L. Rao, **C. Liu**, M. Zhu, J. Wang, G.-K. Chang, "A Novel Full-duplex 60-GHz Radio-over-Fiber Transmission System for Next-Generation Wireless Access Networks," Conference on Lasers and Electro-Optics (CLEO), 2013, CM3G.1.

[16] J. Wang, **C. Liu**, M. Zhu, A. Yi, G.-K. Chang, "Investigation of Intra/Inter-Band Cross-Modulation in Multi-Band Radio-over-Fiber Systems," Conference on Lasers and Electro-Optics (CLEO), 2013, CM3G.5.

[17] Y.-T. Hsueh, **C. Liu**, S.-H. Fan, J. Yu, G.-K. Chang, "A Novel Full-Duplex Testbed Demonstration of Converged All-Band 60-GHz Radio-Over-Fiber

Access Architecture," Optical Fiber Communications Conference (OFC) 2012, OTu2H.5.

[18] S.-H. Fan, **C. Liu**, Y.-T. Hsueh, M. Zhu, T. Wang, G.-K. Chang, "Full-Duplex 60 GHz Vector-Signal Radio-over-Fiber System Using Heterodyne Optical-Carrier Suppression," Optical Fiber Communications Conference (OFC) 2012, JW2A.84.

[19] G.-K. Chang, **C. Liu**, "Millimeter-Wave, Multi-Access Wireless over Fiber Technologies and Applications" IEEE Avionics, Fiber- Optics and Photonics Technology Conference (AVFOP), Sept. 2012, TuB4, Invited Paper

[20] H.-C. Chien, **C. Liu**, J. Liu, S.-H. Fan, Y.-T. Hsueh, Z. Jia, S. He, J. Yu, G.-K. Chang, "Emerging Technologies for Mm-wave RoF Communication," IEEE Photonics Society 2012 Summer Topical Meetings, July 2012, MB4.4 Invited Paper.

[21] J. Pan, **C. Liu**, T. Detwiler, A. Stark, Y.-T. Hsueh, S. E. Ralph, "Inter-Channel Crosstalk Cancellation by MAP Detection for Nyquist-WDM Superchannel," Signal Processing in Photonic Communications (SPPCom), May 2012, SpTu3A.3.

[22] J. Pan, **C. Liu**, T. Detwiler, S. E. Ralph, "Digital Pre-Compensation of Inter-Channel Crosstalk for Nyquist-WDM System," IEEE Photonics Conference (IPC), Sept. 2012, TuU3.

[23] S.-C. Shin, **C. Liu**, S.-H. Fan, Y.-T. Hsueh, S. Hsiao, G.-K. Chang, "A Versatile 60 GHz CMOS Phased Array Transmitter Chipset for Broadband

Radio-over-Fiber Systems," Asia-Pacific Microwave Conference (APMC) Dec. 2011, (1190).

[24] W. Jian, **C. Liu**, H.-C. Chien, S.-H. Fan, J. Yu, J. Wang, C. Yu, Z. Dong, J. Yu, G.-K. Chang, "Link Performance Improved 16QAM-OFDM 60-GHz Radio-over-Fiber System Employing Convolutional Codes," Optical Fiber Communications Conference (OFC), Mar. 2010, OThO4.

[25] W. Jian, **C. Liu**, H.-C. Chien, S.-H. Fan, J. Yu, J. Wang, C. Yu, Z. Dong, J. Yu, G.-K. Chang, "QPSK-OFDM Radio over Polymer Optical Fiber for Broadband In-building 60GHz Wireless Access," Optical Fiber Communications Conference (OFC), Mar. 2010, OTuF3.

[26] J. Pan, A. Stark, **C. Liu**, S. E. Ralph, "Fractionally-Spaced Frequency Domain Linear Crosstalk Cancellation with Spectral Alignment Techniques for Coherent Superchannel Optical Systems," Optical Fiber Communications Conference (OFC) 2013, OW4B.6.

[27] Y.-T. Hsueh, A. Stark, **C. Liu**, T. Detwiler, M. Filer, S. Tibuleac, G-K. Chang, S. E. Ralph, "Nonlinearity Impact on Crosstalk Effects for a 112Gb/s PDM-QPSK System," Optical Fiber Communications Conference (OFC) 2012, NTu1F.4.

[28] L. Zhang, S.-H. Fan, **C. Liu**, M. Zhu, X. Hu, Z. Li, Y. Su, G.-K. Chang, "A Cost-effective Multi-gigabit 60-GHz Wireless over Optical Fiber Access System Based on a Novel Frequency Quintupling Technique," IEEE Photonics Society 2012 Summer Topical Meetings, July 2012, WB1.2.

[29] M. Zhu, L. Zhang, **C. Liu**, S.-H. Fan, G.-K. Chang, “Delivery of Wireless and Wired Services Using a Single-drive Mach-Zehnder Modulator for Bidirectional Radio-over-Fiber Systems” IEEE Photonics Society 2012 Summer Topical Meetings, July 2012, WB4.5.

[30] L. Zhang, P. Cao, X. Hu, **C. Liu**, M. Zhu, A. Yi, C. Ye, Y. Su, G.-K. Chang, “Enhanced Multicast Performance for a 60-GHz Gigabit Wireless Service over Optical Access Network Based on 16-QAM-OFDM Hierarchical Modulation,” Optical Fiber Communications Conference (OFC) 2013, OTu3D.1.

[31] M. Zhu, S.-H. Fan, L. Zhang, **C. Liu**, G.-K. Chang, “Transport of MIMO-OFDM Wireless Services in 60-GHz Radio-over-Fiber System Multiplexed by Optical TDM,” Optical Fiber Communications Conference (OFC) 2013, OTu3D.4.

[32] M. Zhu, A. Yi, Y.-T. Hsueh, **C. Liu**, J. Wang, S.-C. Shin, J. Yu, G.-K. Chang, “Demonstration of 4-Band Millimeter-wave Radio-Over-Fiber System for Multi-service Wireless Access Networks,” Optical Fiber Communications Conference (OFC) 2013, OM3D.4.

[33] L. Zhang, M. Zhu, C. Ye, **C. Liu**, X. Hu, Y. Su, and G.-K. Chang, “Multi-service, Multi-band, and MIMO Data Distribution over 60-GHz RoF System for Gigabit Wireless Local Area Networks,” Asia Communications and Photonics Conference (ACP), Nov. 2012, ATh2C.2.

[34] J. Liu, M. Zhu, S.-H. Fan, **C. Liu**, H.-C. Chien, J. Yu, G.-K. Chang, “Multi-band QPSK Signal Transmission Implemented with Remote Up-Conversion

and Schottky Diode RF Detectors in 60-GHz Millimeter Wave RoF Systems," 2012 International Workshop on OPS and OCDMA, Nov. 2012, Pt7.

[35] A. Stark, Y.-T. Hsueh, T. Detwiler, **C. Liu**, K. Mehat, M. Filer, S. Tibuleac, G.-K. Chang, S. E. Ralph, "Performance of 32 Gbaud PDM-QPSK in Nonlinear Transport Regimes," Proceedings of the SPIE, (Jan 2012), 8284-10.

[36] C. Estevez, S. Angulo, A. Abujatum, G. Ellinas, **C. Liu**, G.-K. Chang, "A Carrier-Ethernet Oriented Transport Protocol with a Novel Congestion Control and QoS Integration: Analytical, Simulated and Experimental Validation," Proc. of IEEE International Conference on Communications (ICC) 2012, page 2673-2678.

[37] A. Chowdhury, H.-C. Chien, S.-H. Fan, **C. Liu**, C. Su, G.-K. Chang, "A Survivable Protection and Restoration Scheme using Wavelength Switching of Integrated Tunable Optical Transmitter for High Throughput WDM-PON System," Optical Fiber Communications Conference (OFC) 2011, OThK6.

[38] G.-K. Chang, J. Long, S.-H. Fan, **C. Liu**, A. Chowdhury, H.-C. Chien, S. Khire, N. Jayant, "Emerging Heterogeneous Optical Wireless Access Networks for Next Generation Telemedicine and Telehealth Applications," Proceedings of the Optoelectronics and Communication Conference (OECC) 2011, Page 381-382

[39] A. Stark, Y.-T. Hsueh, S. Searcy, **C. Liu**, "DQPSK for Metro Networks," Proceedings of the SPIE, Volume 7621, pp. 76210L-8 (2010).

[40] S.-H. Fan, H.-C. Chien, A. Chowdhury, **C. Liu**, W. Jian, Y.-T. Hsueh, G.-K. Chang, "A Novel Radio-over-Fiber System Using the xy-MIMO Wireless

Technique for Enhanced Radio Spectral Efficiency," European Conference on Optical Communications (ECOC), Sept. 2010, Th.9.B.1.

PATENTS AND PATENT APPLICATIONS

[1] **Cheng Liu,** Toshiaki Koike-Akino, Kieran Parsons, "Adaptive Cross-Polarization Modulation Cancellers for Coherent Optical Communication Systems," US Patent (20120263464A1)

[2] **Cheng Liu,** Shu-Hao Fan, Gee-Kung Chang, "RF-Carrier Embedded Optical Radio-Signal Modulation of Heterodyne Optical Carrier Suppression," US Patent Pending (13/784,061)

[3] **Cheng Liu,** Jie Pan, Thomas Detwiler, Stephen Ralph, "Super Receiver for Coherent Optical System," US Provisional Patent Application Filed (61/589,655)

[4] **Cheng Liu,** Hung-Chang Chien, Shu-Hao Fan, Gee-Kung Chang, "Optical Millimeter-Wave Vector Signal Generator," Invention Disclosure (GTRC-5572)

VITA

Cheng Liu was born in Zhengzhou, Henan, China. He received the B.S. degree in electronics engineering from Peking University (PKU) in 2008. He is currently working toward the Ph.D. degree at the School of Electrical and Computer Engineering of Georgia Institute of Technology, Atlanta, since Fall 2008.

During his Ph.D. study at Georgia Tech, he works with Prof. Gee-Kung Chang on several projects for the NSF Center on Optical Wireless Applications. At the mean time, he was a student member of the Georgia Tech Terabit Networking Consortium lead by Prof. Stephen Ralph and Prof. Gee-Kung Chang working on high-speed coherent optical communication systems. In 2010 and 2012, he was a research intern in Mitsubishi Electric Research Laboratories, Cambridge, MA and NEC Labs America, Princeton, NJ, respectively. His research interests are mainly focused on system design and signal processing techniques for next-generation converged optical-wireless access systems and high-speed coherent optical transmission systems. He has authored and co-authored more than 50 peer-reviewed journal and international conference papers, and holds 4 US patents and patent applications.

When he is not working on his research, he enjoys watching and playing basketball and learning digital photography.